MSc Thesis

Finding similarities between the deep mantle structures of Earth & Mercury

Liselotte Mulder

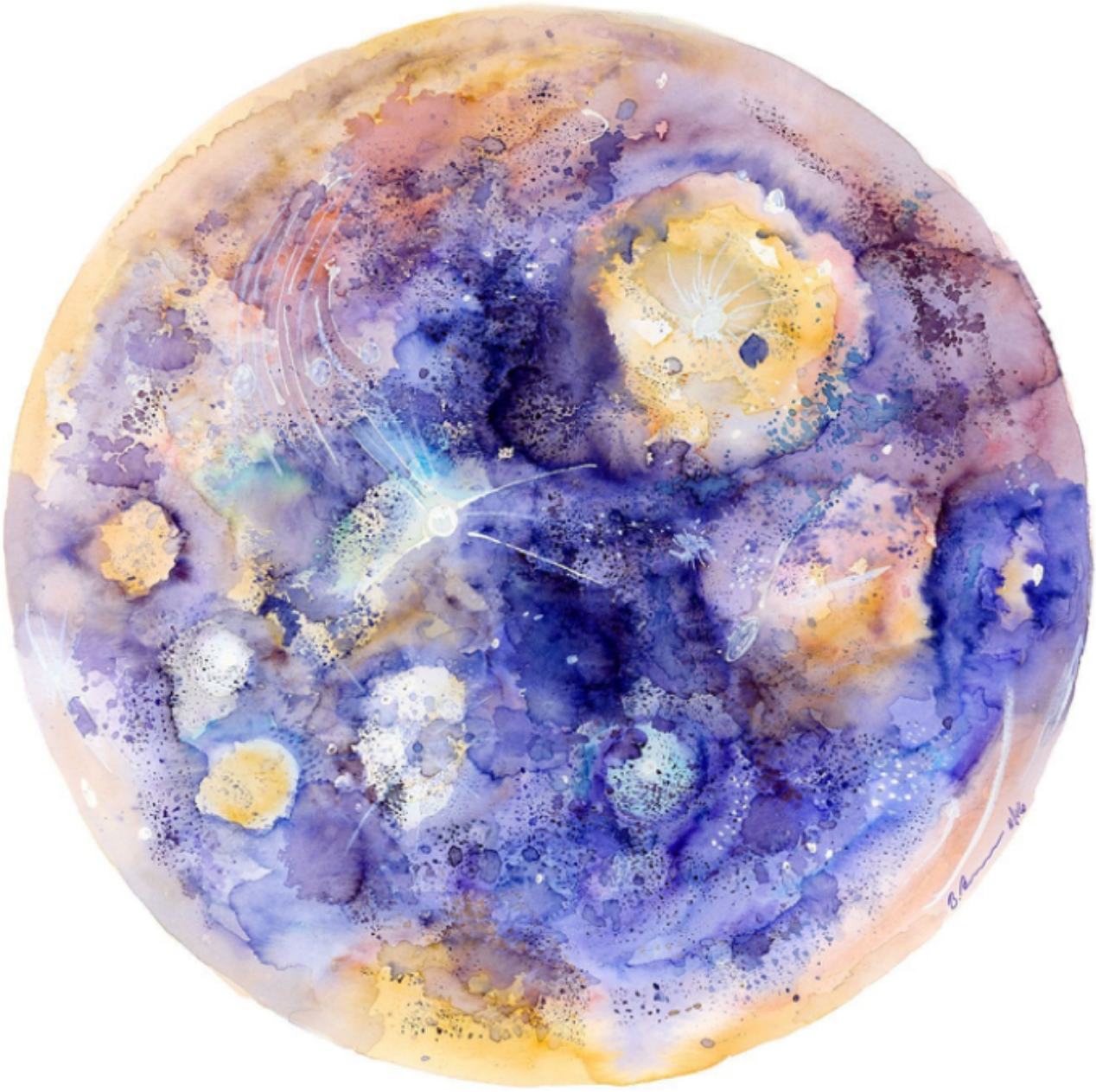

Delft University of Technology

TU Delft

MSc Thesis

Finding similarities between the deep mantle structures of Earth & Mercury

by

Liselotte Mulder

to obtain the degree of Master of Science
at the Delft University of Technology,
to be defended publicly on Thursday December 5, 2019 at 13.00.

Student number:	4305264	
Project duration:	February 4, 2019 – December 5, 2019	
Assessment Committee:	Dr. ir. W. van der Wal	Delft University of Technology, Chair
	Dr. ir. B.C. Root	Delft University of Technology, Supervisor
	Dr. S. Sperreta	Delft University of Technology

An electronic version of this literature study is available at `https://repository.tudelft.nl/`.

Front image: artist impression of Mercury made by *TinyToesDesign*, retrieved from
`https://www.etsy.com/listing/496936916/mercury-watercolor-planet-mercury-art`.

TU Delft

Abstract

In this research project a preliminary investigation is conducted to identify deep mantle structures in Mercury equivalent to the Large Low Shear-Velocity Provinces (LLSVPs) in Earth. The existence of LLSVPs has been acknowledged for several decades (Trønnes, 2010). The two main regions are located beneath the Pacific Ocean (Thomas et al., 2004b) and the African continent (Thomas et al., 2004a). The LLSVPs are predicted to be important for plate tectonics: one of the vital aspects for life on Earth. The observed relation between volcanic features and the LLSVPs suggest a long life span of the LLSVPs (Torsvik et al., 2006). This longevity makes the LLSVPs highly interesting in our attempt to understand Earth's formation and evolution better. The inconvenient location, in the deep mantle of Earth (2900 km depth), inhibits progress in understanding the LLSVPs, as few data is available about this region. Some studies also relate the LLSVPs to geoid highs observed over Earth (Liu and Zhong, 2015) and this allows for investigation of the deep mantle anomalies in Mercury using gravity data. The advantage of Mercury is its thin mantle, causing anomalies in the deep mantle to be located at a relatively shallow location. The origin of this thin mantle is still subject of debate. Suggested explanations are in relation to Mercury's close location to the Sun (Cameron, 1985; Weidenschilling, 1978) or a hit-and-run scenario that ripped off Mercury's mantle (Asphaug and Reufer, 2014). The question to be answered in this thesis is: Could density anomalies in the deep mantle structure of Mercury, similar to the Large Low Shear-Velocity Provinces in Earth, account for the observed long-wavelength gravity field of Mercury?

Before one can start to investigate the deep mantle, the crust and its gravitational features need to be assessed. Various elementary principles for crustal thicknesses and densities are investigated, and a model retrieved from literature is used as well (James et al., 2014). This analysis showed that the crust likely accounts for some of the gravity signature, mainly the short-wavelength anomalies, but that a major anomaly remains. The residual of three models, namely Airy-Heiskanen isostatic compensation, inversion of the Bouguer anomaly and the model from James et al. (2014), need to be counteracted by deep mantle mass anomalies.

To answer the research question, the residual gravity fields of the crustal models are used as input to constrain the density and thickness of deep mantle structures. This analysis yielded that the Airy and Bouguer crustal model allow for deep-mantle structures that have similar density and thickness characteristics as the LLSVPs have in Earth. The James model has a relatively large residual that can be counteracted by mass anomalies, however, given their required size and density, it is arguable whether these can be compared to LLSVPs. An alternative explanation for the gravity field signature is a temperature anomaly in the mantle of Mercury (Tosi et al., 2015). This temperate anomaly would result from the propagation of the peculiar insolation pattern of the surface of Mercury into the mantle. It is assessed for its effect on the density and hence the gravity field. Various mantle compositions were tested for phase transitions, and the resulting density differences were computed. Different combinations of the three crustal models and several mantle models were used as input to compute the required CMB topography in order to match the gravity observations. It is observed that the James crustal model matches the density anomaly that is induced by the temperature anomaly well. The Airy and Bouguer models require large CMB variations which are rendered unfeasible.

The relation between the crustal models and volcanic features is also investigated. LLSVPs in Earth are shown to have a relation with Large Igneous Provinces (LIPs) and hotspots. Equivalent volcanic features on Mercury, smooth plains and pyroclastic vents, are assessed for their correspondence with the hypothetical deep mass anomalies. The three crustal models show no correspondence with the volcanic features. Because of the uncertainty in the crustal models and the incomplete map of pyroclastic vents due to limited coverage of Mercury, this conclusion could not be drawn with high confidence.

Recommendations for future research include the improvement of the fitting algorithm and concurrent consideration of size and density variations in the basal layer. Furthermore, this study can partially be repeated when higher fidelity data is available following the BepiColombo mission, currently en route to Mercury. Alternatively, the possibility of LLSVPs in Mars could be further investigated (Burke et al., 2012), given the high accuracy of the available gravity field data and the deployment of a seismometer by the Insight mission.

Preface

This document is the culmination of my studies in Aerospace Engineering at Delft University of Technology. It contains my MSc thesis report, that concludes my MSc degree in the field of Spaceflight, Space Exploration. The conducted research is about similarities between the deep mantle structures of Earth & Mercury, which special attention for deep mass anomalies in Mercury that are similar to the Large Low Shear-Velocity Provinces in Earth. This thesis is conducted in light of ESA's BepiColombo mission, that is currently en route to Mercury. I selected this subject because of my profound interest in understanding the universe and exploration of extraterrestrial life.

I would like to thank my supervisor Bart Root for his guidance in conducting this thesis. Our weekly meetings always resulted in useful insights and new inspiration to continue in good spirit. I appreciate Peter B. James, Sebastian Padovan, Marc A. Wieczorek, Timothy A. Goudge and Isamu Matsuyama for our email conversations to answer my questions about their research and enhance my understanding in their fields of expertise. Also, I would like to express my gratitude to Peter B. James for sharing his crustal model of Mercury, that I used as one of the models to investigate deep mass anomalies. I would like to thank Timothy Goudge for sharing his complete data set of the locations of pyroclastic vents.

Liselotte Mulder
Delft, November 2019

Contents

List of Figures

List of Tables

Nomenclature

Roman Symbols

D	average radial location of crust-mantle boundary layer
D	flexural rigidity
E	E-modulus
G	standard gravitational parameter
g	gravity
g_B	Bouguer anomaly
h	altitude
h_{lm}	shape coefficients
M	mass
n	spherical harmonic degree
k	wavelength
p	pressure
R	average planetary radius
r	radial location
t	thickness
w	filter

Greek symbols

α	thermal expansion coefficient
$\Delta\rho$	density difference
λ	Lagrange parameter
λ	latitude
ν	Poisson ratio
ρ	density
θ	latitude
Φ	flexural response
ξ	weight fraction

Subscripts

avg	average
c	crustal
$comp$	compensation
e	elastic
$infill$	infill (material that substitutes other material)
l	spherical harmonic degree l
k	wavelength
lm	spherical harmonic degree l, order m
m	mantle
n	spherical harmonic order n
max	maximum
$mean$	mean
min	minimum
$root$	crustal root (from Airy-Heiskanen theory)
0	value at t = 0

Superscripts

BA	Bouguer Anomaly

Abbreviations

Al	Aluminium (element)
CMB	Core-Mantle Boundary
Ca	Calcium (element)
Cr	Chromium (element)
ESA	European Space Agency
ETH	Eidgenössische Technische Hochschule
FC	Mercury mantle model from Fegley and Cameron (1987)
Fe	Iron (element)
GRS	Gamma Ray Spectrometer
GSHA	Global Spherical Harmonic Analysis
GT	Mercury mantle model from Goettel (1988)
Ga	Giga-annum, 1 billion years
HRC	Hit-and-Run Collision
JAXA	Japan Aerospace Exploration Agency
K	Potassium (element)
LIP	Large Igneous Province
LLSVP	Large Low Shear-Velocity Provinces
MESSENGER	MErcury Surface, Space ENvironment, GEochemistry and Ranging
MORB	Mid-Ocean Ridge Basalt
MA	Mercury mantle model from Morgan and Anders (1980)
MC	Mercury mantle model from Krot et al. (2001)
Ma	Mega-annum, 1 million years
Mg	Magnesium (element)
Mn	Manganese (element)
mGal	MilliGal ($1{\cdot}10^{-5}$ m/s^2)
NASA	National Aeronautics and Space Administration
Na	Sodium (element)
O	Oxygen (element)
S	Sulfur (element)
SH	Spherical harmonic
Si	Silicate (element)
TBL	Thermal Boundary Layer
Ti	Titanium (element)
TS	Mercury mantle model from Taylor and Scott (2005)

1 Introduction

Mercury is the innermost terrestrial planet in our Solar System. This position relates to the fact that Mercury's orbital period around the Sun is the shortest of all planets in our Solar System. This fast rotation motivated the Romans to name the planet after their winged and thus swift-footed messenger of the Gods, namely Mercury (May, 2011). Mercury is also the least explored terrestrial planet. In the 70's the Mariner-10 mission performed two flyby's and gave a first insight into Mercury, and over the past decade NASA's MErcury Surface, Space ENvironment, GEochemistry, and Ranging (MESSENGER) mission orbited the planet and provided data of a more global coverage. In October 2018, ESA's first mission to Mercury in the form of BepiColombo has been launched, that will arrive after seven years and will hopefully provide answers to the many questions that still remain. Interest in missions to Mercury is rapidly increasing, as understanding of the innermost planet of our Solar System located in close proximity to the Sun, can drastically enhance our understanding of the beginning of the Solar system and planet formation. However, missions to Mercury are subject to major technological challenges due to this close proximity to the Sun, because of the subsequent strong gravitational pull by the Sun and harsh radiation environment (Benkhoff et al., 2010).

In this thesis the gravity, composition and topography data retrieved from MESSENGER, Mariner-10 and Earth observations is used to investigate the possibility of deep mantle mass anomalies in Mercury. Similar features in Earth, Large Low Shear-Velocity Provinces (LLSVPs), are detected in seismological and gravity data. The inconvenient location of the LLSVPs in Earth inhibit the progress in our understanding of the deep mantle. Expanding our understanding of the deep mantle structure of Mercury and making the analogy with the mantle of Earth, is a creative solution that could aid in our understanding of present-day Earth, her history and evolution.

LLSVPs

In 1983, Lay and Helmberger (1983) noticed a discontinuity in the shear-wave velocity at 280 km above the core-mantle boundary (CMB) of the Earth. Around that time, it was assumed that the CMB-layer could be modelled as a smooth, thermal boundary layer with only minor velocity gradients. Lateral velocity variations were not discovered any earlier, as previous studies used an averaged velocity structure, in which the discontinuities of about 2.75 ± 0.25% disappeared. This stratification, nowadays known as the LLSVPs, is likely to drastically influence the thermal and dynamic evolution of the Earth (Lay and Helmberger, 1983; Trønnes, 2010).

Initially, Lay and Helmberger (1983) determined the stratification of the CMB-layer to be 280 ± 40 km. In later studies, conducted by different research groups and using various data sources, several tomographic models of the LLSVPs have been constructed. These models all illustrate the location and size of the LLSVPs, and yield similar results, although not exactly. Garnero et al. (2016) summarised the different findings on the location and size of the LLSVPs. Consistent throughout all models is that two LLSVPs are identified, the African and the Pacific LLSVP, that cumulatively cover approximately 30% of the CMB. Furthermore, in all models the Pacific LLSVP has an oval shape, while the African LLSVP is more elongated in the north-south direction.

The vertical extent of the LLSVPs is not included in this global map. Obviously, the vertical extent of the LLSVPs also varies across the models. While (Lay and Helmberger, 1983) observed a discontinuity 280 ± 40 km above the CMB, later models have indicated that in some regions the LLSVPs can extend up to 1200 km above the CMB (Garnero et al., 2016). The LLSVPs in general do not have a smooth form, but contain several bulges and steep edges. The models agree on the observation that the African LLSVP is larger and has more continuous edges, while the Pacific LLSVP shows a more whimsical shape (Cottaar and Lekic, 2016). The Pacific LLSVP can be divided in three parts: the West anomaly, the Superswell anomaly and the East anomaly. The anomalies can be seen as bulges of approximately 1000 km high (from the CMB) that are connected by regions with an average height of 300-400 km (Cottaar and Lekic, 2016; He and Wen, 2009). The African LLSVP has a more continuous shape and an average height of 500-1000 km (Cottaar and Lekic, 2016; Wang and Wen, 2007).

The inconvenient location of the LLSVPs, in the deep mantle at ~3000 km depth, complicates the investigation of the LLSVPs. The constituent of the LLSVPs is not known, however there are several theories about what the LLSVPs are made up of:

- Post-perovskite has been investigated as constituent of the deep-mantle layer many times. Sidorin et al. (1999) calculated that the Clapeyron slope of a potential phase transition in the deep mantle would be ~6 MPa/K. Oganov and Ono (2004) and Murakami (2004) independently matched this value to the Clapeyron slope of the transition from bridgmanite to post-perovskite. The phase transition changes the structure of the materials, hence resulting in different crystallographic and elastic properties.
  This phase transition would be activated by a temperature anomaly that is induced by the subduction of tectonic slab material, or Mid-Ocean Ridge Basalt (MORB). This mechanism introduces cool material into the deep mantle, and at locations where this cooling of the mantle takes place, the conditions exist in which the phase transition occur.
  The discovery of the phase transition to post-perovskite and its suitability to explain the situation in the deep mantle, triggered new investigations about post-perovskite to prove this further. These later studies showed that the bridgmanite phase transition would also clarify other unresolved mysteries observed in seismic waves coming from the deep mantle:
  - Significant seismic anisotropy that is observed in seismic data is explained by the lattice-preferred orientation of post-perovskite (Oganov and Ono, 2004; Murakami, 2004).
  - The anti-correlation between shear and bulk sound velocities observed by Su and Dziewonski (1997), were explained as the consequence of either thermal variations or a large compositional variation. Oganov and Ono (2004) showed that the formation of post-perovskite in the deep mantle would yield these observations indeed.
  - Two oppositely polarised discontinuities are identified at the location of the LLSVPs (Hernlund et al., 2005), beneath Euroasia (Thomas et al., 2004a) and the Pacific Ocean (Thomas et al., 2004b). Numerical models showed that the convective cells produced by the subduction of plate material creates the desired circumstances to facilitate the transition to post-perovskite. The boundaries of this convective cell are visible as a double-crossing, indicating that post-perovskite transitions into bridgmanite again as soon as it heats again towards the CMB. This explanation would also clarify why at certain regions the phase transition is not observed; that is the 'hot' region where the mantle is not cooled by subducted MORB material.
- Other studies question this theory on post-perovskite and argue that it is more likely that a chemical heterogeneity explains the observations. Wen (2001) and To et al. (2005) were the first to claim that the observations can not be explained by a thermal gradient only. They do not render the existence of post-perovskite impossible, but argue that another mechanism, in addition to post-perovskite theory, is required to explain the observations fully. The steep edges of the LLSVPs could for example be well explained by the post-perovskite theory. A side-note to this is that the theory on post-perovskite was not fully established yet by the time of these publications.
  According to Hirose (2006), an anti-correlation between density and shear-wave velocity, presuming the LLSVPs are high in density, can only be explained by a chemical distinction and not by a phase transition. Furthermore do they state that the Clapeyron slope that is now used as strong evidence for post-perovskite, is highly dependent on temperature and pressure at which the transition takes place. As the temperature and pressure in the deep Earth are only roughly known, this introduces a large

uncertainty in the allegation. Also, the sample size of the experiment during which the Clapeyron slope was determined, was small because of the highly challenging environment that had to be created.
Possible chemical heterogeneities that act as alternatives for the post-perovskite transition and that would explain the behaviour in the deep mantle, are:

- The MORB-material that moves into the deep Earth and causes a local cooler region, could in addition to the cooling effect also accumulate and form a distinct chemical layer (Hirose, 2006). Seismic tomographic measurements show that subducted slabs can penetrate into the deep mantle (Trønnes, 2010; Garnero et al., 2016) and numerical models also supports that the basaltic crust can reach as far as the deep mantle (Hirose, 2006).
- By experimental research it has been found that a chemical reaction between liquid iron in the core and mantle minerals could result in an FeSi-alloy (Dubrovinsky et al., 2003). The reaction product directly adjoining the core is presumed to be dispersed by the flow of the core (Knittle and Jeanloz, 1989). This alloy could form a chemically distinct layer at the CMB (Garnero et al., 2016; Manga and Jeanloz, 1996). This proposition has been further investigated by Otsuka and Karato (2012); Hirose et al. (2006), however has not lead to any further conclusions.
- Partial melting has been opted as a third explanation. In a material that constitutes several different minerals it is possible that at a certain temperature some minerals are in liquid form, while others remain solid (Hirose, 2006). This melt could possess very different characteristics than the solid material does, which results in a complex pattern in the seismic wave propagation. The chemical consequences of partial melting are poorly investigated and thus not known yet, and also it is unclear if partial melting could account for the enormous thickness of the LLSVPs.

The above enumeration illustrates the uncertainties that are still encountered in the characterisation of the LLSVPs. This analysis does not explicitly rule out the existence of a phase transition from bridgmanite to post-perovskite in the deeper layer of the Earth. Rather it suggests the presence of a more complex physical environment than is characterised by a sole phase transition (Hirose, 2006). It therefore seems appropriate to refer to the LLSVPs as thermochemical piles (Trønnes, 2010).

Geoid highs

In addition to the seismic observations of the LLSVPs, the LLSVPs are also recognised in the gravity data (Trønnes, 2010; Liu and Zhong, 2015). These positive geoid undulations over the Earth do not correspond with the continents, nor do they show any relation with mid-ocean ridges (Anderson, 1982; Liu and Zhong, 2015). The undulations can however be associated with hotspots and subduction zones. After removal of these undulations, the residual geoid shows large peaks near the central Pacific and the Atlantic-African region, although slightly shifted. This could indicate a relation between the geoid highs and the LLSVPs.

Large Igneous Provinces & Hotspot volcanism

An important discovery about the LLSVPs is their (seemingly) relation with Large Igneous Provinces (LIPs) (Trønnes, 2010). LIPs are large regions of solidified magma, or igneous rocks, at the surface of the Earth. LIPs are mainly identified by their composition and can be dated back to 1 Ga (Wingate et al., 2004). LIPs are not necessarily located near plate margins, as 'ordinary' volcanoes are, and their origin is still under investigation. LIPs are often related to hotspots: the type of volcanism that does not have its origin near plate boundaries (Torsvik et al., 2006; Zhao, 2001).

Burke and Torsvik (2004) and Torsvik et al. (2006) investigated the relation between the locations of the LIPs and the LLSVPs. Several models, all based on different assumptions, were used to map the currently observed location of the LIPs on the Earth's surface to the location where the initial eruption took place - the latter can be compared to the location of the LLSVPs. All models revealed that ~90% of the eruption sites of the LIPs are located at the boundaries of the LLSVPs, going back 200, 251 and 300 Ma (Burke and Torsvik, 2004; Torsvik et al., 2006, 2008). Other LIPs that can not be related directly to the margins of the LLSVPs, might be associated with minor LLSVPs that have not been detected in seismological data yet (Castle et al., 2000; Kuo et al., 2000).

The physical explanation for this observation is further analysed in a geodynamical model. Steinberger and Torsvik (2012) show that the combination of 1) a thermal boundary layer (TBL) along which heat is transferred

from the core to the mantle, 2) subduction of lithospheric slabs towards the deep mantle and 3) discontinuous chemically distinct and dense layer at the base of the mantle indeed induces rising mantle plumes. These plumes only arise when all three conditions are present, and the lack of either one results in an entirely different spread of the locations of the LIPs and hotspots.

Hirose (2006) and Tan et al. (2002) explain how the combination of these three aspects could initiate the plumes. The phase change from bridgmanite to post-perovskite that is induced by the cold slab material that wells down, is highly exothermic. The depressing force and the exothermic reaction cause instabilities and/or thickness variations in the TBL. The generation of these irregularities in the TBL already occur when the penetrating slab is still distant from the TBL. As soon as the slab actually reaches the CMB, the slab is forced aside. The earlier induced thickness variations are pushed forward. At the location where a plume reaches the LLSVP, the plume is forced up into the mantle, eventually resulting in LIPs and hotspots. The small plumes are not (yet) seismically detected, only large upwellings beneath the central Pacific and Africa are observed in the deep mantle (Zhao, 2001). It is therefore generally assumed that the smaller plumes bundle into superplumes (Schubert et al., 2004).

An important conclusion from these studies is that the LLSVPs are temporally and spatially stable for at least 250 Ma. This apparent long-term temporal and spatial stability of the LLSVPs puts constraints on the density of the LLSVPs. Strong heating coming from the CMB would induce thermal expansion and buoyancy of the LLSVPs, yielding that the LLSVPs vanish over time. The observed stability therefore implies that the density contrast between the LLSVP material and the surroundings is large (McNamara and Zhong, 2005). However, the steep margins of the LLSVPs imply that the density contrast is moderate (Trønnes, 2010). A balance between these two conditions should thus be present.

The inconvenient location of the LLSVPs, deep in the mantle, inhibits the progress in the understanding of the LLSVPs. On Mercury, the similar geoid undulations associated with the LLSVPs are observed, which might indicate that a similar deep mantle structure can be seen on Mercury. The mantle of Mercury is much thinner than that of Earth, and therefore the location of potential LLSVPs in Mercury is much shallower. Investigation of the interior of Mercury therefore might reveal more information about LLSVPs, presuming that actual deep density anomalies exist in Mercury. In the following section our knowledge of the interior of Mercury is further explained, with a focus on the analogies between Earth and Mercury.

LLSVPS in relation to Mercury

Mercury is the least explored planet in our Solar System. Despite the few missions that have travelled to Mercury and the limited availability observational data that is available, the planet is still relatively well understood. This is because of the progress that is made in the understanding of the planet using mathematical models (Peale, 1969, 1988), in addition to the available observational data (Margot et al., 2018).

Mercury is build up of several layers: a high-density core with possible differentiation into a solid inner core and a liquid outer core, a thin mantle with a possible basal layer at the CMB and a crust. The bulk density of Mercury is 5429.30 ± 0.28 kg/m^3, which is high in comparison with other terrestrial planets and is close to the bulk density of Earth. Several explanations have been suggested for the thin mantle of Mercury. Weidenschilling (1978) explains the planet's composition as a consequence of a slightly more effective aerodynamic removal process of silicate than of iron (Fe), resulting in a iron-rich body. Cameron (1985) proposed that Mercury used to be of much larger size, more like the other terrestrial planets, but that the immense heat coming from the solar nebula led to vaporisation of the mantle and that this material was carried away with surrounding gasses of the solar nebula cloud. A third explanation is the hit-and-run scenario, suggested by Asphaug and Reufer (2014). In such an event two bodies collide, during which the first body is only slightly eroded, while the second body is ripped off the mantle. Shocks cause the mantle material to vaporise and disperse. The core-component and a small part of the mantle of the second body remain gravitationally bound. Observations on the surface composition have revealed that the surface has a relatively low abundance of iron, which is hard to explain in combination with the high bulk density of the planet. A distinct layer at the base of the mantle is opted in literature to explain the depletion of Fe in the surface of Mercury. The distinct layer could inhibit Fe to migrate from the core to the mantle, leaving few Fe particles in the mantle and crust.

Hermeoid highs

The gravity field of Mercury has been mapped by the MESSENGER mission up until spherical harmonic degree 50 (Mazarico et al., 2014). MESSENGER followed an eccentric orbit around Mercury, with a distant apogee above the south pole, hence causing a discrepancy in the accuracy of the data on the northern and southern hemisphere. This is the case for all data retrieved from MESSENGER, and is clearly observable in the gravity field. The Hermeoid (analogous to the geoid of the Earth) shows two bulges along the equator at 0^{o}E and 180^{o}E, similar gravitational bulges as we observe on Earth. Some of these bulges can be partially related to the Caloris, Subkou and Budh basins. The locations of these impact craters is at the location of gravity anomalies, suggesting a relation. The rest of these two bulges can not be related to topographic anomalies, and therefore must be explained by other mass anomalies. A possibility are deep mantle mass anomalies: similar features as we observe in Earth in the form of LLSVPs.

Matsuyama and Nimmo (2009) analysed Mercury's gravity field resulting from additional effects: tidal deformation, despinning, variable eccentricity, and reorientation of a residual bulge. It was concluded that neither the mass excess associated with the Caloris basin nor a large remnant bulge acquired when the planet was rotating faster can account alone for the observed gravity at degree 2. They proposed instead a more complex scenario in which a (sufficiently) large gravity anomaly associated with Caloris drove the reorientation of an also large remnant bulge through an event of true polar wander.

Volcanism

On Mercury, smooth plains and pyroclastic vents are considered signatures of volcanism. There is no indication on Mercury for plate tectonics, and therefore volcanic features require a different explanation. The smooth plains are regions of distinct morphology and composition and are expected to be solidified lava flows (Wieczorek, 2015). The plains cover a large part of Mercury's surface, and are concentrated in the northern hemisphere (Denevi et al., 2013). As the LIPs on Earth are mentioned in relation to the LLSVPs, the smooth plains on Mercury might provide valuable information about the location of LLSVPs in Mercury.

Pyroclastic deposits are explosive volcanic eruption signatures, that are the result of the fragmentation and eruption of magma particles, propelled through the expansion of volatiles released from rising bodies of magma (Kerber et al., 2011). On Mercury, 51 pyroclastic deposits are identified and they are considered to be of a global scale (Kerber et al., 2011; Goudge et al., 2014). A study by Goudge et al. (2014) found that the pyroclastic deposits were likely amassed on Mercury's surface throughout a long period of time. The deposits do not show any relation with smooth plains, but their locations do correspond to the locations of impact craters (Goudge et al., 2014). Thinner crust at these locations as a consequence of an impact could allow for easier penetration of the mantle materials through the crust, resulting in pyroclastic vents. However, not all pyroclastic vents are located near impact basins and therefore this hypothesis is not fully confirmed. An analogy between hotspot volcanism on Earth and pyroclastic vents on Mercury is not ruled out.

Deep mantle structure

The gravity field of Mercury, and especially its C2-anomalies, have been subject of investigations earlier. James et al. (2014) described how irregularities in the possible basal layer could emerge and sustain over time, causing anomalies in the gravity field. Tosi et al. (2015) investigated how the insolation pattern of Mercury could induce temperature differences throughout the mantle. The 3/2 spin-orbit resonance of Mercury (3 sidereal days for every 2 sidereal years) generate hot and cold poles across Mercury. The density differences that result from this could reflect the gravity field anomalies, either as the result of density reductions following from thermal expansion or because of an induced phase transition.

Research question

Should there be LLSVPs in Mercury, then this would be highly interesting because of the shallow location they would have in Mercury. Despite the complexity of reaching Mercury, the big advantage of researching the LLSVPs in our Solar System's inner planet is the thin mantle of Mercury. The deep location of the LLSVPs inhibit the progress in our understanding of the deep mantle structure. The longevity of the LLSVPs in Earth and their effect on mantle convection and Earth's volcanism, render it possible that the LLSVPs play a major role in the Earth's formation and evolution. Understanding the deep mantle features is essential in our quest to understand how life has developed, and what might be prerequisites for life as we know it on Earth.

The size of Mercury is much smaller than that of Earth, and especially the mantle thicknesses differ. Despite the similar bulk densities of the planets, it is likely that the compositions of the planets also highly differ, as they formed under highly different circumstances. This causes the LLSVPs to be located not only in a shallower position, also in a totally different physical environments. Furthermore, there is no tectonic activity on Mercury detected (yet) - this contradicts with the likely relation between tectonic activity and LLSVPs in Earth. These differences are important to keep in the back of the mind during the research, but are considered not to render the comparison unlikely and/or impossible. The research question therefore is:

Could density anomalies in the deep mantle structure of Mercury, similar to the Large Low Shear-Velocity Provinces in Earth, account for the observed long-wavelength gravity field of Mercury?

1. What knowledge about Mercury is available to constrain the crustal interference with the gravity field?
   (a) Assuming isostatic compensation, what would be the crustal thickness and density?
   (b) Assuming Bouguer compensation, what would be the crustal thickness and density?
   (c) Are there other crustal models of Mercury available?
2. What could be possible causes for deep-mantle mass anomalies in Mercury?
   (a) What would be the effect of LLSVP-like structures with an anomalous thickness or density on the gravity field of Mercury?
   (b) What would be the effect of temperature anomalies in the mantle on the gravity field of Mercury?
   (c) What would be the effect of CMB topography on the gravity field of Mercury?
3. What other information is available to constrain the size and density of deep mantle mass anomalies?
   (a) What is the relation between volcanic features on Mercury and the Hermeoid?
   (b) Are the normal modes of Mercury related to deep mantle mass anomalies?

With the long-wavelength gravity field the gravity anomalies captured in the lower spherical harmonic degrees (<10) are meant. Analysis of the gravity field of the Earth has confirmed the hypothesis that short-wavelength features are visible in the crust, and that the long-wavelength features are dominated by the mass anomalies in the deep mantle. The LLSVPs are located in the deep mantle of the Earth, hence their gravity signature is expected to be visible in the lower spherical harmonic degrees.

This study is performed in consideration of the BepiColombo mission. This ESA mission is designated to collect more information on the composition, geophysics, atmosphere, magnetosphere and history of the planet. The mission aims to provide a better understanding of formation and history of Mercury, and the inner planets of our Solar System in general.[1] In light of this mission objective, this thesis is an excellent preparatory assessment of the information about the deep mantle structure enclosed in the currently available data.

This thesis will start in Chapter 2 with the construction of a crustal model for Mercury. Several researchers have investigated the crustal thickness and density of Mercury before, and to rule out the possibility that shallow crustal features explain the C2- gravity anomalies, the crust is investigated. In Chapter 3 the relation between volcanic features observed on the surface of Mercury and the Hermeoid resulting from the potential deep mass anomalies are compared. The crustal models are then used in Chapter 4 to investigate possible size and density combination of LLSVPs in Mercury. The mantle composition of Mercury will be analysed for its suitability to facilitate such a density transition and also CMB variations are investigated as a possibility to explain the observations. For all these gravity analyses the Global Spherical Harmonic Analysis software constructed by Root et al. (2017) is used. In Chapter 6 the results are reviewed and put into context. In Chapter 7 conclusion from this research are drawn. The appendices include more information on the available topography and gravity data and some additional plots about the modelled deep mantle structures.

[1] https://www.esa.int/Science_Exploration/Space_Science/BepiColombo_overview2

2

Crustal Model

The first step in numerically simulating the gravity field of Mercury, is making a model of the crust. By identifying what features in the gravity field can be assigned to the crust of Mercury, one can also identify how the gravity field of Mercury is affected by deep mass anomalies. To this end several data sources are available, that can be used to make a preliminary estimate of the crustal thickness and density. Different physical theories are currently available to construct a crustal model and several of these will be subject of further analysis in this chapter. Their advantages and limitations will be discussed, such that a best fit model can be selected in later stages of this research project. This chapter will begin with a brief discussion about the available gravity and topography data, and what can be concluded from that about Mercury. Then, in Section 2.2an analysis of the crustal thickness and density using local isostasy in the form of the Airy-Heiskanen and Pratt-Hayford compensation mechanisms is described. In Section 2.3 the theory of regional isostasy is considered. The topography and gravity field will be used further to construct and investigate the Bouguer anomaly in Section 2.4. In Section 2.5 the crustal model constructed by James et al. (2014) is subject of analysis. In Section 2.6 the process and results of the addition of small crustal density increments is described, which is done to construct a crustal model that matches the gravity observations better. The chapter is concluded in Section 2.7.

2.1. Data Analysis

Mercury is the least explored terrestrial planet of our Solar System. In the 70s, Mariner-10 performed some flyby's of the planet, that provided some idea of the characteristics of the planet. MESSENGER (the MErcury Surface, Space ENvironment, GEochemistry and Ranging) was launched in 2004 and yielded more information on the exterior and interior of the planet. Unfortunately, MESSENGER executed a highly eccentric orbit, resulting in good coverage of the northern hemisphere, however poor coverage of the southern hemisphere. In the data this is also clearly visible, and it is therefore important to keep that in mind during the analysis.

The current best estimate of the mass of Mercury (Mohr et al., 2012) is

$$M = (3.301110 \pm 0.00015) \times 10^{23} \text{ kg}.$$

Using laser altimetry and radar occultation data the average radius of Mercury is determined (Margot et al., 2018). The uncertainty in this value can be attributed to the sparse sampling of the southern hemisphere.

$$R = (2439.35 \pm 0.02) \text{ km}.$$

The above values allow for an estimate of the bulk density (Margot et al., 2018):

$$\rho = (5429.30 \pm 0.28) \text{ kg} \cdot \text{m}^{-3}$$

This bulk density is similar to that of Earth, which is roughly 5500 kg/m^3 (Fowler, 2005, p.336). However, the smaller radius of Mercury implies lower pressures in the interior of Mercury. The material inside Mercury is thus less compressed than the material inside Earth. From the equivalent bulk densities and differing sizes, it can be deduced that Mercury must consist of a large metallic component (Ash et al., 1971; Margot et al., 2018).

The data that is used in this study is retrieved from NASA[1]. The topography of Mercury is mapped until spherical harmonic degree (SH) 150. This topographic model is constructed from laser altimetry, stereophotogrammetry, optical limb measurements and radio occultations (Wieczorek, 2015). The gravity field is constructed by Mazarico et al. (2014). The fluctuation in degree strength n across the planet in field maps is illustrated in Figure 8b of (Mazarico et al., 2014). The maps show that the highest degree strength is n>36 in the most northern region of Mercury and that this decreases to n ~15 in the equatorial region and reduces further to n<10 at the South Pole.

The Mollweide and stereographic projections of the topography and free-air anomaly field are presented in Figure 2.1 and Figure 2.2 respectively. All figures have several features of Mercury indicated, that will be discussed later.

The terrain of Mercury is heavily cratered. The smooth plains observed within and in the surroundings of the Caloris basin, in combination with the level of cratering that is observed, indicate that this is probably the youngest surface on Mercury (Fassett et al., 2011). Comparison of the density and size of the craters observed on Mercury and that of the Moon, yield that Mercury must have experienced resurfacing in its early history. Smooth plains are observed at more locations on Mercury. Approximately 27% of Mercury's surface is covered with smooth plains, of which about two-thirds are estimated to be of volcanic origin. The composition of the plains varies across the planet, indicating that the magma sources are different and might have changed over time (Denevi et al., 2013). The northern smooth plains are associated with regional negative gravitational anomalies.

Amongst the many impact craters and basins, there are several interesting ones. These are discussed separately in the following bullet list.

- The Caloris basin (170^{o}E, 30^{o}N) was already noticed in the images the the Mariner-10 satellite sent back to Earth. It is one of the best-preserved impact craters on Mercury, making it relatively easy to analyse. In the topographic data, the Caloris basin is associated with degree 18-28 (James et al., 2014).
  The Caloris basin shows two concentric rings, one with a radius of 690 km and one with a radius of 850 km (Head et al., 2010). The inner ring has a smooth inner surface, indicating that the interior of the basin has been resurfaced with volcanic plains. Several smaller impact craters are still visible, showing the radial layering of the Caloris crust (Prockter et al., 2008). The structure of the rim of the basin varies largely - ranging from a steep two-kilometre deep cliff to rough, cratered plains showing radial troughs. The varying rim structure is mentioned in relation to the pre-impact terrain structure (Head et al., 2010).
  The plains surrounding the Caloris basin, also called the Odin-type plains, are often thought of as Caloris impact ejecta. Crater-counting, however, has indicated that the Odin-type plains are younger than the Caloris basin, and therefore it is more likely that the surrounding plains have a volcanic origin (Fassett et al., 2009).

- The Sobkou basin (134^{o}W, 36^{o}N) lies to the east of the Caloris basin, outside of the smooth plains that encircle Caloris. The Sobkou basin is associated with a positive gravitational anomaly that not exactly coincides with the location of the basin. The inner part of Sobkou is covered with smooth plains that are expected to be of volcanic origin. The crater density on the plain is such that the age of the crater is older than the age of the plains, meaning that the plains are the remains of volcanic events rather than solidified impact melt (Fassett et al., 2011).

- The Budh basin (152^{o}W, 17^{o}N) is observed in topography data, however, in the gravity field the Budh basin is mainly associated with the gravitational rise that is in between Budh and Sobkou. According to Smith et al. (2012), the strong positive anomaly in the Bouguer anomaly map and the weaker gravity anomaly in the free-air field indicate crustal thinning beneath the basins and a relatively thick crust directly beneath the positive gravity anomaly.

- Rachmaninoff (58^{o}E, 28^{o}N) is an impact basin of 290 km in diameter and is of high scientific interest because of its relatively young age. It is the point of lowest elevation on Mercury, namely around 5.5 km deep. Rachmaninoff shows an inner area that is filled with smooth plains. The craters within the basin appear to be of similar materials as the plains, indicating volcanism (Prockter et al., 2010).

[1] `http://pds-geosciences.wustl.edu/messenger/mess-h-rss_mla-5-sdp-v1/messrs_1001/data/shadr/`

- The Northern rise (33°E, 68°N) is situated in the middle of the northern smooth plains and is most clearly visible in the stereographic projection in Figure 2.1. The formation history of the northern rise remains a mystery because of several reasons. Craters on the flanks of the rise indicate that the formation of the rise took place after the surface had been cratered, indicating that the rise formed at a relatively late stage. Furthermore, the northern rise does not show to be compositionally different from the smooth plains (James, 2018). A similar rise is observed at the Budh-Sobkou rise and in the northern part of the Caloris basin. The northern rise is associated with degrees 30-34 (James et al., 2014).

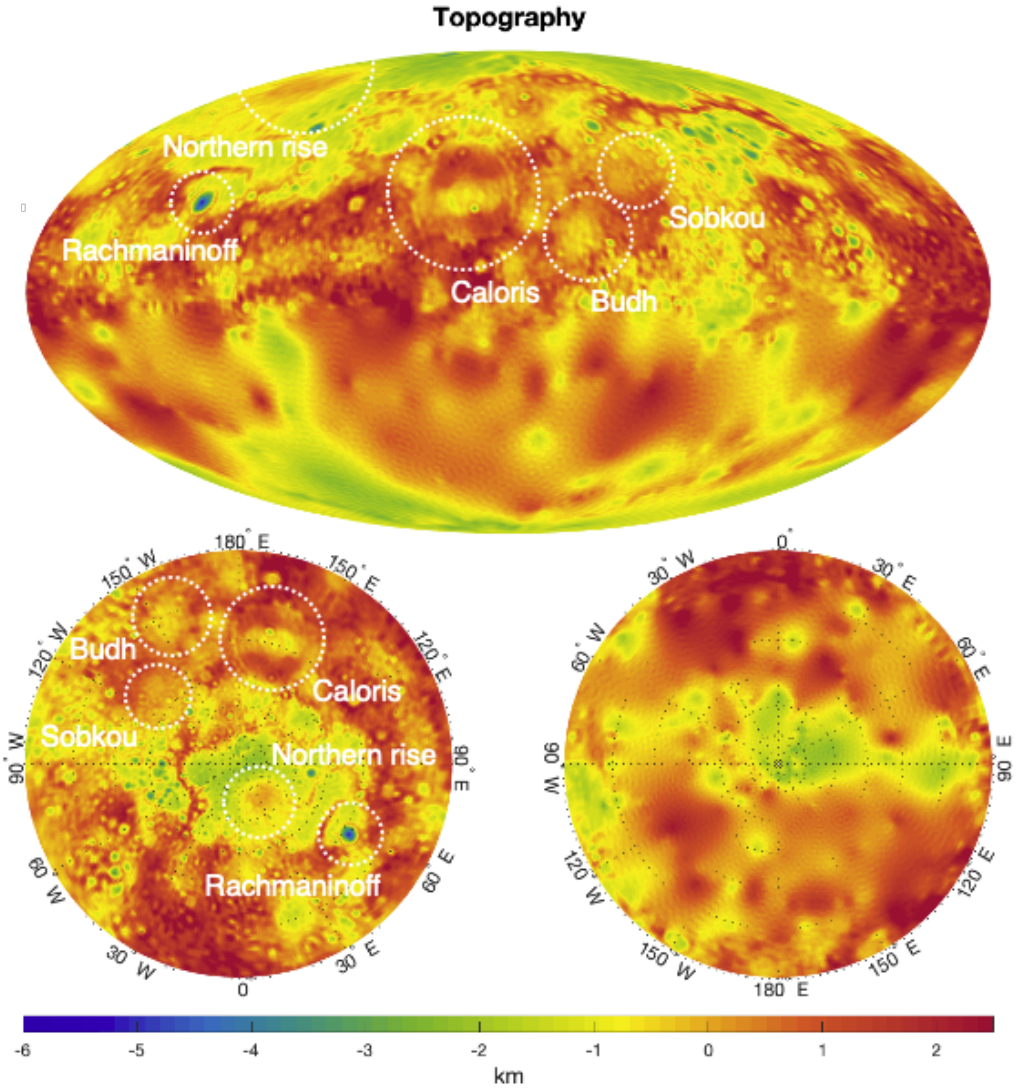

Figure 2.1: Mollweide projection (central meridian of 180°E) and stereographic plots of the topography on Mercury. Left stereographic projection is the northern hemisphere, the right projection is the southern hemisphere. Indicated on the map are five important topographic features on Mercury: 1) Rachmaninoff basin, 2) Northern rise, 3) Caloris basin, 4) Budh basin and 5) Sobkou basin. The projection is constructed using the dataset that contains the data up to spherical harmonic degree 150.

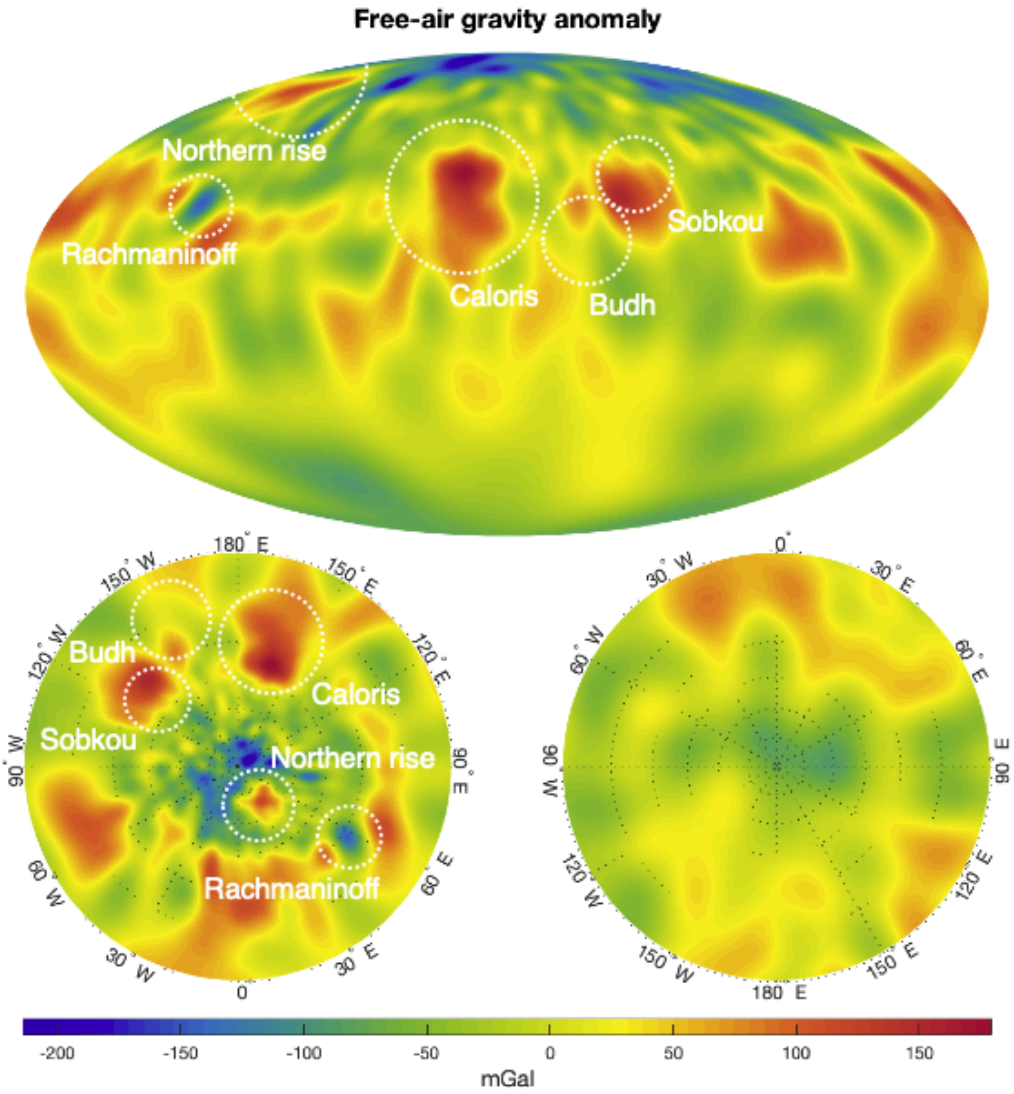

Figure 2.2: Mollweide projection (central meridian of 180°E) and stereographic plots of the gravity anomaly field of Mercury. Left stereographic projection is the northern hemisphere, the right projection is the southern hemisphere. Indicated on the map are five important topographic features on Mercury: 1) Rachmaninoff basin, 2) Northern rise, 3) Caloris basin, 4) Budh basin and 5) Sobkou basin. The projection is constructed using the dataset that contains the data up to spherical harmonic degree 50, which degree 0, 1 and C_{20} removed.

2.1.1. Power spectra

In Figure 2.3 the power spectra of the gravity and topography coefficients (or shape coefficients, as long as C_{00} is not set to zero) are plotted, along with the admittance and correlation spectra. The left plot in Figure 2.3 shows the power spectrum of both the gravity coefficients and the shape coefficients, along with their uncertainties. The topography shows a relatively large uncertainty already at lower degrees; at degree 17 the uncertainty already exceeds the magnitude of the coefficient. The gravity field is known with more certainty, and the uncertainty exceeds the magnitude of the coefficient at degree 40 and further. This uncertainty in the short-wavelength domain will mainly affect the crustal model, because of its often close relation with topographic and crustal density variations. It is predicted that the uncertainty is mainly caused by lack of data for the southern hemisphere, and that the coefficient for the northern hemisphere are still relatively accurate. Because of the difference in spherical harmonic accuracy between the topography and gravity field, the topography model is truncated at SH50. When analysing gravity and shape data simultaneously, it is unreasonable to use a different degree and order of the coefficient sets and therefore the precision of the gravity data is limiting.

The correlation and admittance spectra are given in the right plot of Figure 2.3. Except for degree 9, the admittance shows values in the range of several tens of mGal/km. This is less than the admittance that would be predicted for uncompensated topography (Wieczorek, 2015), indicating that the topography is compensated. With smaller wavelengths the admittance decreases, indicating the small wavelength topographic signatures are almost fully compensated. The correlation ranges between -0.05 and 1, tell that various topographic features are correlated with the gravity, but also that some degrees do not possess this correlation. For example, the deep trough at SH9 in both the correlation and the admittance spectra indicate that on some locations the topography does not correspond to gravity anomalies of equal sign. This could for example be caused by the several basins on Mercury, that are associated with positive gravity anomalies although their topography is negative. Mascons - mass concentrations, also observed on for example the Moon (Muller and Sjogren, 1968) - and deep mantle mass anomalies could be the cause for the non-correlation, as these features cause positive gravity anomalies where there is no increase in elevation. Correlation between the two fields in the short-wavelength domain can be established with less certainty because of the uncertainty in the coefficients, and observed discrepancies between the fields should be assigned less significance.

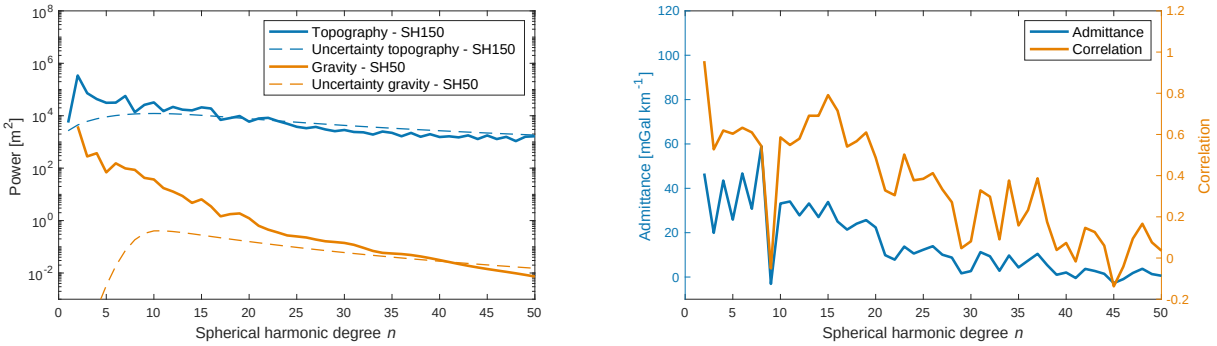

Figure 2.3: Spectral analysis of the gravity (Mazarico et al., 2014) and topography data observed by MESSENGER (Smith 2012, not part of an official publication). The power spectra of the gravity and topography data are plotted along with their given uncertainties. The admittance and correlation spectra are often used to assess the level of topographic compensation.

2.2. Local isostasy

Models on isostatic equilibrium describe how layers of thin and relatively light crust overlay a fluid mantle layer with relatively high density. A key aspect in isostasy is that columns of equal size are assumed to have equal mass. The buoyancy force that follows from the displacement of the fluid by the crustal root, balances with the gravitational attraction. High mountain regions are thus either compensated by a large root, or are made up of lightweight material (Watts, 2001). These two physical explanations, varying crustal thickness versus varying crustal density, are discussed separately.

2.2.1. Airy - Heiskanen

In the Airy-Heiskanen model, the equal column masses are assumed to be effectuated by crustal thickness variations. Therefore, elevated regions are assumed to be underlain by light regions, in which heavy mantle material is replaced by light crust material and thus where the crustal thickness is larger. Vice versa, deep basins show so-called anti-roots, where crustal material has been substituted by heavy mantle components, resulting in a relatively thin crust. This compensation mechanism is based on equal masses in all columns (Watts, 2001).

In his publication Airy already pointed out that he considered it unlikely that all surface features on Earth were in isostatic equilibrium and 'floating' on the mantle (Watts, 2001). Seismic data of the Earth, not available at the time of publication, has however in the meantime indicated that the assumption of isostatic compensation is valid for several regions on Earth (Watts, 2001). For Mercury however, seismic data is still not available, and investigation of isostasy is limited to the analysis of topography and gravity measurements. It is therefore important to carefully consider the inherent assumptions of Airy isostasy, and evaluate their prerequisites and implications.

Method

According to the Airy-Heiskanen theory the crustal thickness can be calculated using Equation 2.1. Following Equation 2.1, the crust is built up of three parts: the average crustal thickness part $t_{c,avg}$, the elevation of the topography h (can also be of negative sign), and the right part of the equation, that can also be named the thickness of the root t_{root}.

$$t_c = t_{c,avg} + h + \frac{h \cdot \rho_c}{\rho_m - \rho_c} \tag{2.1}$$

In Equation 2.1, h can be computed by subtracting the average radius of Mercury (2439.35 km) from the shape of Mercury. The shape of Mercury is mapped by MESSENGER and represented in spherical harmonic coefficients. The other input parameters ($t_{c,avg}$, ρ_c and $\rho_m - \rho_c$) require assumptions. Earlier studies on the crustal thickness of Mercury, analysis of surface composition maps and analogy with other planets give some reasonable ranges for the input parameters. An overview is given in Table 2.1.

Smith et al. (2012)	$t_{c,avg}$	= 50 km
	ρ_c	= 3100 kg $\cdot$ m^{-3}
	ρ_m - ρ_c	= 200 kg $\cdot$ m^{-3}
James et al. (2014)	$t_{c,avg}$	= 40 km
	ρ_c	= 3200 kg $\cdot$ m^{-3}
	ρ_m - ρ_c	= 200 kg $\cdot$ m^{-3}
Wieczorek (2015)	$t_{c,avg}$	= 26 km
	ρ_c	= 2900 kg $\cdot$ m^{-3}
	ρ_m - ρ_c	= 300 kg $\cdot$ m^{-3}
Padovan et al. (2015)	$t_{c,avg}$	= 35 $\pm$ 18 km
	ρ_c	= 2700 - 3100 kg $\cdot$ m^{-3}
	ρ_m - ρ_c	= 400 kg $\cdot$ m^{-3}
Sori (2018)	$t_{c,avg}$	= 26 $\pm$ 11 km
	ρ_c	= 2700 - 3100 kg $\cdot$ m^{-3}
	ρ_m - ρ_c	= - *

Table 2.1: Overview of input parameters for Airy-Heiskanen model used in literature. * Sori (2018) uses the admittance in his calculation on the Mercury's crust and his conclusions thus do not depend on the crust-mantle density contrast.

A schematic representation of the Airy-Heiskanen mechanism is given in Figure 2.4. The lower limit that is indicated in the drawing is the limit up to which the analysis is performed, and can be set to any value that is deeper than the deepest point of the crust. Please note that h can also be a value smaller than 0, resulting in a negative t_{root}.

Results

For the ranges of values for the input parameters as given in Table 2.1 the model as sketched in Figure 2.4 is tested. In Figure 2.4 two layers are drawn, however for the analysis these two layers are split up in several layers to ensure convergence, for more information see Section 5.6. The lower boundary is set to the deepest location of the crust. For each input parameter combination the average crustal thickness is calculated. Also, the corresponding gravity field anomalies (taken to be spherical harmonic degree 2 and higher with C_{20} = 0) of the observed gravity field and the calculated crustal gravity field are compared and the root-mean-square value of the residual is calculated. It is concluded that the variability of the input parameters does not invoke noteworthy variations in the resulting average crustal thickness. The average crustal thickness, $t_{c,avg}$ in Equation 2.1 is highly determinant in the final crustal thickness, and the variation that is induced by variations in the crust and mantle density are considerably less. Also for the residual of the models it is observed that no large variations between the parameter sets can be observed, and that there is no parameter set outperforming others. Therefore, an arbitrary parameter set was chosen to analyse the applicability of the Airy-Heiskanen theory in more detail. The average crustal density was set to 2800 kg/m^3, the density difference between crust and mantle to 300 kg/m^3 and the average crustal thickness to 50 km. These parameters were selected based on literature (see Table 2.1). The results are shown in Figure 2.5.

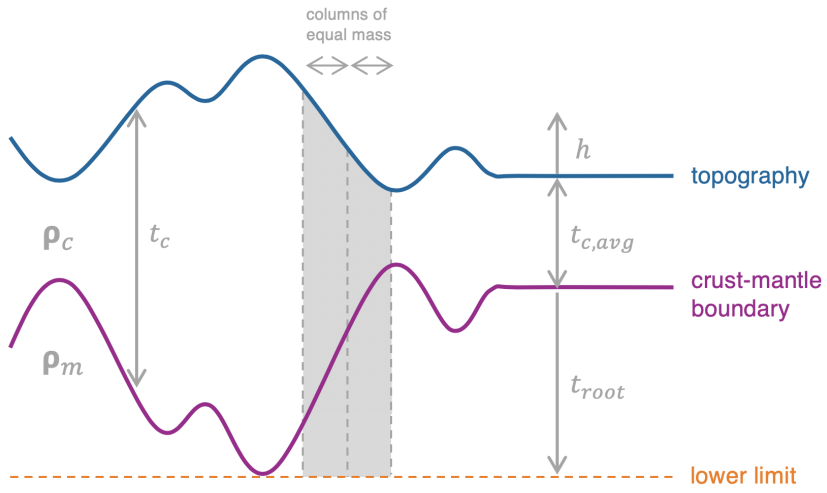

Figure 2.4: Schematic representation of the Airy-Heiskanen model. ρ_c is crustal density, ρ_m = mantle density, t_c is the crustal thickness, h is the elevation, $t_{c,avg}$ is the (assumed) average crustal thickness and t_{root} is the (calculated) thickness of the crustal root. The lower limit of the model is set to deepest location of the total crustal root.

Figure 2.5a shows the free-air gravity anomaly field up to spherical harmonic degree 50, that was deduced from MESSENGER. Plot (b) shows the gravity field for the same spherical harmonic degrees that results from a fully Airy-Heiskanen isostatically compensated crust. Please note that all plots use the same scale, which is decided so to enhance legibility. It is observed that the measured gravity field shows a much stronger signal than the crustal gravity field. In comparison with the observed gravity field, the crustal gravity is rather constant and does not show that much variation across the planet. The residual between the two fields therefore is much alike the observed gravity field; the outlook of the free-air anomaly is also visible in the residual plot. Several characteristic features that are observed on the surface of Mercury:

- Caloris impact basin (170°E, 30°N) and Sobkou impact basin(134°W, 36°N) are both still clearly visible in the residual data. The anomalies are not in isostatic equilibrium and thus require a different physical explanation. As both features are basins resulting from an impact event (Fassett et al., 2009), this could be (part of) the explanation for their associated anomaly. The heat and pressure waves of the impact could well affect the crust and mantle composition (Fassett et al., 2009). Smith et al. (2012) mentioned the basins in relation to mascons, which would well fit these observations as well. Furthermore, resurfacing of the Caloris basin with smooth plains of volcanic origin affects the gravity anomaly, and so are the regions outside of Caloris that are also associated with this phenomenon (James et al., 2014).

- Rachmaninoff (58°E, 28°N) basin was already mentioned as an outstanding feature in the Bouguer analysis, and it is that in the isostasy analysis as well. According to Airy, basins would be associated with thin crust and thick mantle, resulting in positive gravity anomalies. However, in Figure 2.5a the basin is associated with a strong negative anomaly, and this remains after isostatically compensating the basin. Comparison of the observations with the residual shows that the anomaly seems reduced, especially in the inner part of the basin. This indicates that the gravity anomaly extends further than the observed topographic outlines of the basins, and that it does requires a broader topographic variation than the shape data shows for it to be isostatically compensated. The impact might have had a bigger effect on the surroundings than merely the observed basin. The Rachmaninoff basin is covered with smooth plains that are probably of volcanic origin (Denevi et al., 2013), and this might give a biased view of the extent of isostatic compensation that is required.

  Based on these observations it is concluded that the Rachmaninoff basin is not Airy-Heiskanen-compensated.

- The Budh basin (152°W, 17°N) is of little interest. It is slightly visible in gravity data, and also in the crustal gravity it is not a prominent feature. A close-up view of the topography clearly shows a basin, however the depth of this basin is not significant in the Airy-Heiskanen analysis. Therefore, the residual also does not show very strong signs of this topographic feature.

- The Northern rise (33°E, 68°N) is slightly smoothed in the residual data, and thus shows some signs of isostatic compensation. However, the northern rise remains visible in the residual plot, and is thus not fully isostatically compensated following these results. The origin of the Northern rise is still unknown (James, 2018), and it could be that a combination of isostatic compensation and another compensation mechanism are at play.

Padovan et al. (2015) already indicated that it is unlikely that these topographic features are (fully) isostatically compensated and this is thus also confirmed in this isostasy analysis. Padovan et al. (2015) did however prove, by using the admittance of the gravity and topography field, that spherical harmonic degree 9-15 show to be Airy isostatically compensated. With this research they calculated an average crustal thickness of 35 ± 18 km and Sori (2018) refined this estimate to 26 ± 11 km assuming equal pressures Airy-Heiskanen compensation, instead of equal masses Airy-Heiskanen compensation.

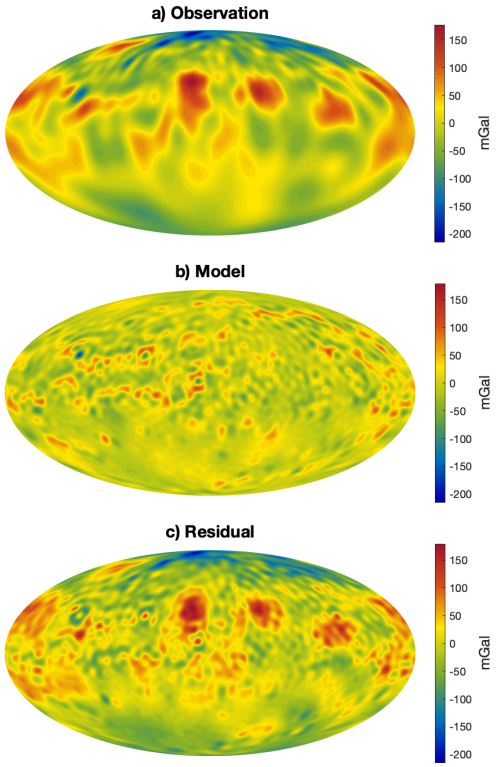

Figure 2.5: Comparison of the free-air gravity anomaly field and an Airy-isostatically compensated crust. (a) The observed free-air anomaly gravity field. (b) Gravity field resulting from an Airy isostatically compensated crust, with ρ_c = 2800 kg/m^3, ρ_m - ρ_c = 300 kg/m^3 and $t_{c,avg}$ = 50 km. (c) Residual of the two fields. All fields are computed for spherical harmonic degree 2-50 (C_{20} is excluded). Images are in Mollweide projection with a central meridian of 180°E.

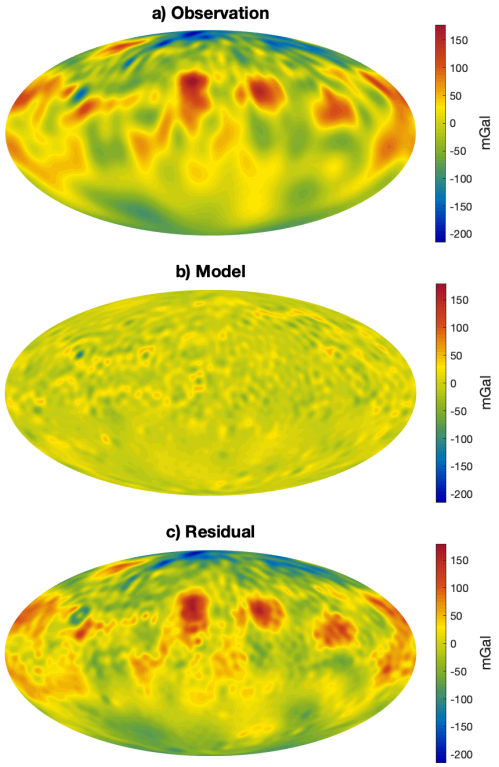

Figure 2.6: Comparison of the free-air gravity anomaly field and a Pratt isostatically compensated crust. (a) The observed free-air anomaly gravity field. (b) Gravity field resulting from a Pratt isostatically compensated crust, with ρ_c = 2800 kg/m^3 and $t_{c,avg}$ = 50 km. (c) Residual of the two fields. All fields are computed for spherical harmonic degree 2-50 (C_{20} is excluded). The average crustal density is 2817 kg/m^3. Images are in Mollweide projection with a central meridian of 180°E.

2.2.2. Pratt - Hayford

The Pratt-Hayford model is much similar to the Airy-Heiskanen model as it is also based on an equal mass assumption. The equal mass is however not achieved by variable crustal thicknesses, but by variations in crustal density. Elevated regions are thus made up of light material, whereas low basins are assumed to be underlain by high density material.

Method

The Pratt-Hayford model dictates that the crustal density can be calculated using Equation 2.2. The average crustal density $\rho_{c,avg}$ and the compensation depth t_{comp} require assumptions. Ranges for these values can be

computed from Table 2.1, assuming that the compensation depth can be deduced from the average crustal thickness. A schematic overview of the Pratt-Hayford model is given in Figure 2.7. For the calculation the crust is split into several layers, again to ensure convergence.

$$\rho_c = \rho_{c,avg} \cdot \frac{t_{comp}}{t_{comp} + h} \tag{2.2}$$

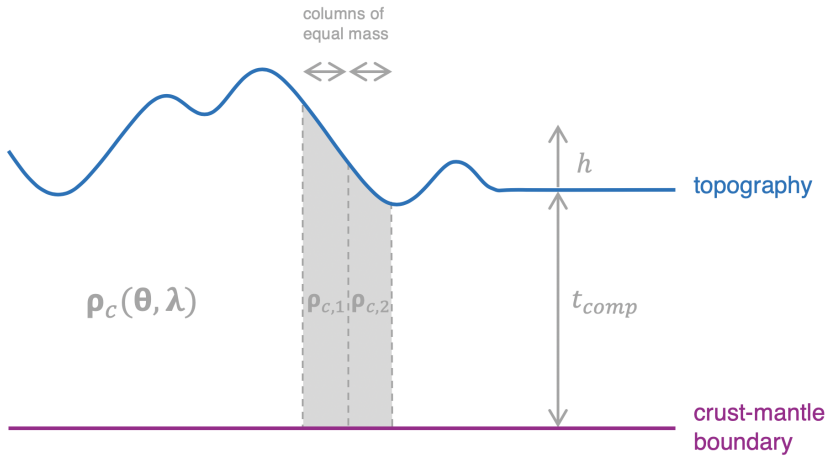

Figure 2.7: Schematic representation of the Pratt-Hayford model. ρ_c is crustal density and varies across the planet, ρ_m is mantle density, t_{comp} is the compensation depth, h is the elevation. The lower limit of the model is in the Pratt-Hayford theory equal to the compensation depth.

Results

One representative combination of the input parameters is analysed in more detail, namely the one where the average crustal density is set to 2800 kg/m^3, and the mean crustal thickness is set to 50 km, both taken from literature (see Table 2.1). The results are shown in Figure 2.6.

Figure 2.6 shows that the Pratt crustal gravity is relatively small in comparison with the observed gravity field. The residual field in Figure 2.6c shows strong resemblance with the observed field and the overall magnitude remains the same, indicating that the Pratt isostatically compensated crust is not minimising the residual. As with Airy-Heiskanen isostasy, distinct topographic features on Mercury are not especially counteracted.

Pressure isostasy

Pressure isostasy is a better approximation of isostasy in reality, however also adds complexity to the calculations. In pressure isostasy, one assumes no longer equal masses, but equal pressures instead. For smaller planets, with a smaller radius of curvature, the assumption of mass isostasy becomes disputable because of the spherical shape of the crust. Therefore, for this study the effect of the mass assumption was assessed. Sori (2018) quantified the effect on the average crustal thickness and found a reduction in this parameter of 25%. Variations in the average crustal thickness will however not be visible in the free-air gravity anomaly field, and only lateral variation in the crustal root is of importance in this specific study. The effect of the mass assumption on the thickness of the crustal root can be quantified using Equation 3 in (Hemingway and Matsuyama, 2017). For the case of Mercury it was found that the effect on the size of the crustal root is ~1%, and it is assumed that this can be neglected.

2.3. Regional isostasy

Regional isostasy is bending of the crust under the loading that is induced by the weight of the topography. In local isostasy, this crust is assumed to be weak and therefore topographic features require to be locally compensated. In the Bouguer approach, the crust is assumed to be rigid, therefore not responding to the induced load. In flexural isostasy, or regional isostasy, the strength of the crust is assumed to be finite. The lithosphere suppresses short-wavelength deformation and passes the long-wavelength deformation. (Watts, 2001)

This process can be further mathematically analysed by approximating the crust as a thin plate. The flexural response function Φ_e of a plate can then be calculated using Equation 2.3, where k is the wave number, ρ_m is the mantle density, ρ_{infill} is the density of the material that infills the flexural depression and g is the nominal gravity. D is the flexural rigidity, which is a measure for the resistance offered by the crust while undergoing bending, and is calculated using Equation 2.4. E is the E-modulus of the material, T_e is the elastic thickness of the crust, ν is the Poisson ratio. The wave number k can be calculated as a function of spherical harmonic degree n, and requires the radius R of the planet to be inserted (Watts and Moore, 2017).

$$\Phi_e(k) = \left[\frac{D \cdot k^4}{(\rho_m - \rho_{infill}) \cdot g} + 1 \right]^{-1} \tag{2.3}$$

$$D = \frac{E \cdot T_e^3}{12(1-\nu^2)} \tag{2.4}$$

$$k(n) = \frac{2n+1}{2R} \tag{2.5}$$

In Figure 2.8 the flexural rigidity of Mercury's crust is given for several cases. The range for the value of the elastic thickness is set rather arbitrarily. Observations of this parameter on other planets, Earth, Mars and Venus, and also previous investigations on Mercury using this parameter, provide some constraints. The large temperature variations on Mercury due to unbalanced solar irradiation of Mercury, might impose a large range in the elastic thickness over the surface of Mercury. It could therefore well be that the surface of Mercury can be represented as several regions with different elastic thicknesses, that, being concatenated, match the observations. The infill density is set to the crustal density that was also used in earlier analysis.

In the flexural response function it is observed that for the precision of the model that is currently available, SH50, the compensation mechanism is a combination of pure Airy isostasy and flexural response. Bouguer compensation is only of importance for high values of T_e. Bouguer compensation commences around degree 100, mainly depending on the elastic thickness, and is well beyond the limit of the available gravity model. Furthermore it is clear that the elastic thickness is an important parameter as it shifts the flexural response function rather rigorously, especially in comparison with the effect of density differences. Therefore elastic thickness is kept as a variable parameter in the remaining part of the analysis.

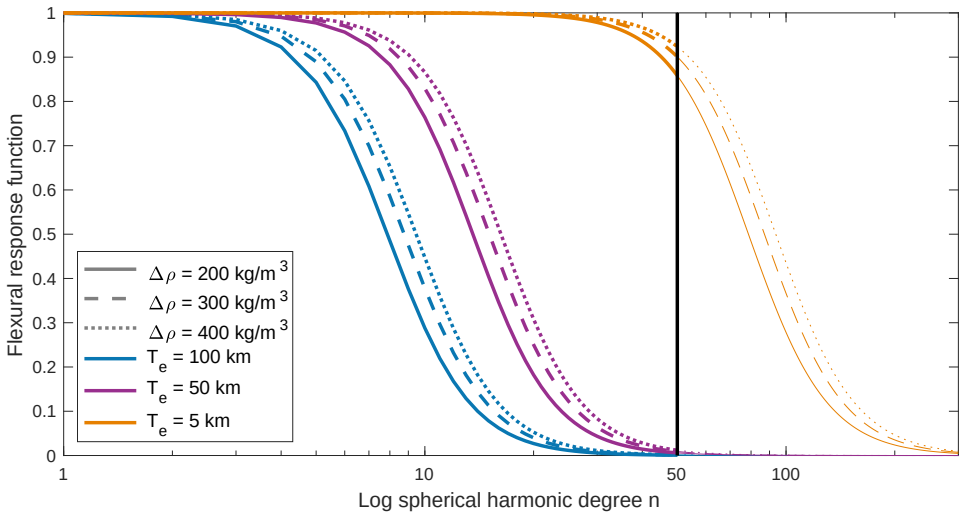

Figure 2.8: Flexural response function of Mercury's crust for different input parameters. The vertical black line indicates spherical harmonic degree 50 - the accuracy of the currently available gravity model.

2.3.1. Airy-Heiskanen model

The flexural response filters are applied to the crustal thickness of the Airy-Heiskanen crustal model. In Figure 2.9 also the power spectrum from observations and the power spectrum from the topographic gravity (= Bouguer correction) is plotted, along with the gravity signatures from the crustal models with various elastic thicknesses. It is observed that the gravity power spectrum from the crustal gravity without a filter is larger than the observations, and that application of the flexural filter only shifts the gravity field of the crustal model further away from the observations, towards the Bouguer correction. Filters corresponding to a higher elastic thickness produce more flattened crust and thus shift the crustal gravity more towards the topographic gravity. Vice versa do filters with a low elastic thickness resemble the Airy model without filter.

At spherical harmonic degrees larger than 20, the gravity signal of an unfiltered Airy crustal model exceeds the actual observations. This indicates that an Airy compensated crust would produce a too large gravity signal to match the observations, and that it is not possible that the Airy compensation model is at play as it is currently modelled. A possible explanation could be that the compensation depth of the crust is shallower than is currently modelled. A thinner crust would reduce the magnitude of the gravity anomalies and hence better comply with the observations.

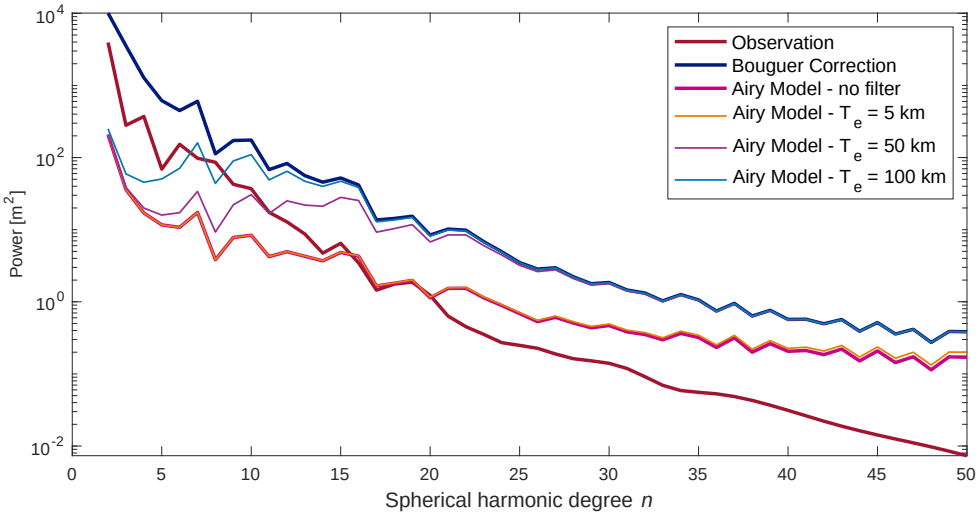

Figure 2.9: Gravity power spectra of the Airy-Heiskanen model with several flexural response filters. ρ_c = 2800 kg/m^3, ρ_m = 3100 kg/m^3, $t_{c,mean}$ = 50 km.

2.3.2. Pratt-Hayford model

A similar analysis is done for the Pratt-Hayford model, where the flexure filter is applied over the density of the crustal layer. The results are shown in Figure 2.10. Apart from the inherent differences between the methods, the effect of the filter is similar for both approaches, as was expected.

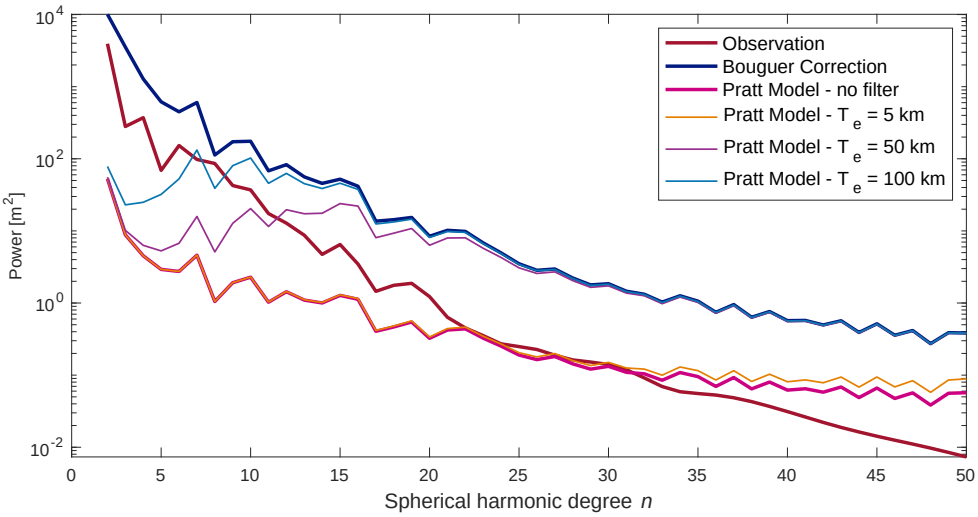

Figure 2.10: Gravity power spectra of the Pratt-Hayford model with several flexural response filters. ρ_c = 2800 kg/m^3, ρ_m = 3100 kg/m^3, t$_{comp}$ = 50 km.

2.4. Bouguer

A useful comparison of topography and gravity data is described by the Bouguer correction. The Bouguer correction accounts for the gravitational attraction of mass between the measurement point and sea level. The Bouguer anomaly, that is calculated by subtracting the Bouguer topographic reduction from the free-air gravity anomaly field, represents the gravity field that is induced by all material below sea level (Fowler, 2005).

The Bouguer anomaly is thus an indication of the gravity anomalies that are not caused by topographic anomalies, but solely by internal variations in density distribution. The Bouguer anomaly for the northern hemisphere is presented in Figure 2.11, computed using the Global Spherical Harmonic Analysis software (GSHA) (Root et al., 2016) (where positive topography is assigned a positive density, and negative topography is assigned a negative density) and assuming a crustal density of 2800 kg/m^3. The southern hemisphere is not analysed, as poor coverage of the southern hemisphere has resulted in low quality data.

Inspection of the Bouguer anomaly indicates that the topographic reduction is stronger than the observed gravity field. Whereas the gravity field anomalies would first lie within ±200 mGal, the Bouguer anomalies now show a variation within ±300 mGal. As a result, Mercury's topographic features are strongly visible in the Bouguer anomaly. Comparison with literature yields that this is more often the result of applying the Bouguer correction, see Section 5.3 for a more in depth explanation.

Topographic features that are not isostatically compensated, are expected to vanish in the Bouguer anomaly. For *uncompensated* features, it is assumed that no crustal thickness or crustal density variations are associated with this specific topographic feature. Contrary to these uncompensated features, topographic features that are isostatically compensated are expected to show either positive Bouguer anomalies for basins, or negative Bouguer anomalies for mountain areas. Isostasy was discussed and investigated in more detail in Section 2.2. Some observations from Figure 2.11:

- Caloris basin (160^{o}E, 31^{o}N) has a clear gravity anomaly associated with it. The topographic correction does not compensate for this region, to the contrary: the gravity anomaly is increased. This might point to isostatic equilibrium, where lower elevated regions are associated with positive gravity anomalies. However, several studies ((James et al., 2014), (Padovan et al., 2015)) have pointed out that isostatic equilibrium is unlikely for Caloris basin. The basin is the result of a relatively recent impact event, and smooth plains in the basin and surrounding the basin indicate that a high level of volcanic activity has been or is still present. It is expected that several compensation mechanisms are superimposed in this region (James et al., 2014). Smith et al. (2012) argue that Caloris basin is a mascon, pointing out the good spatial correlation between the free-air gravity anomaly and the location of the basin.

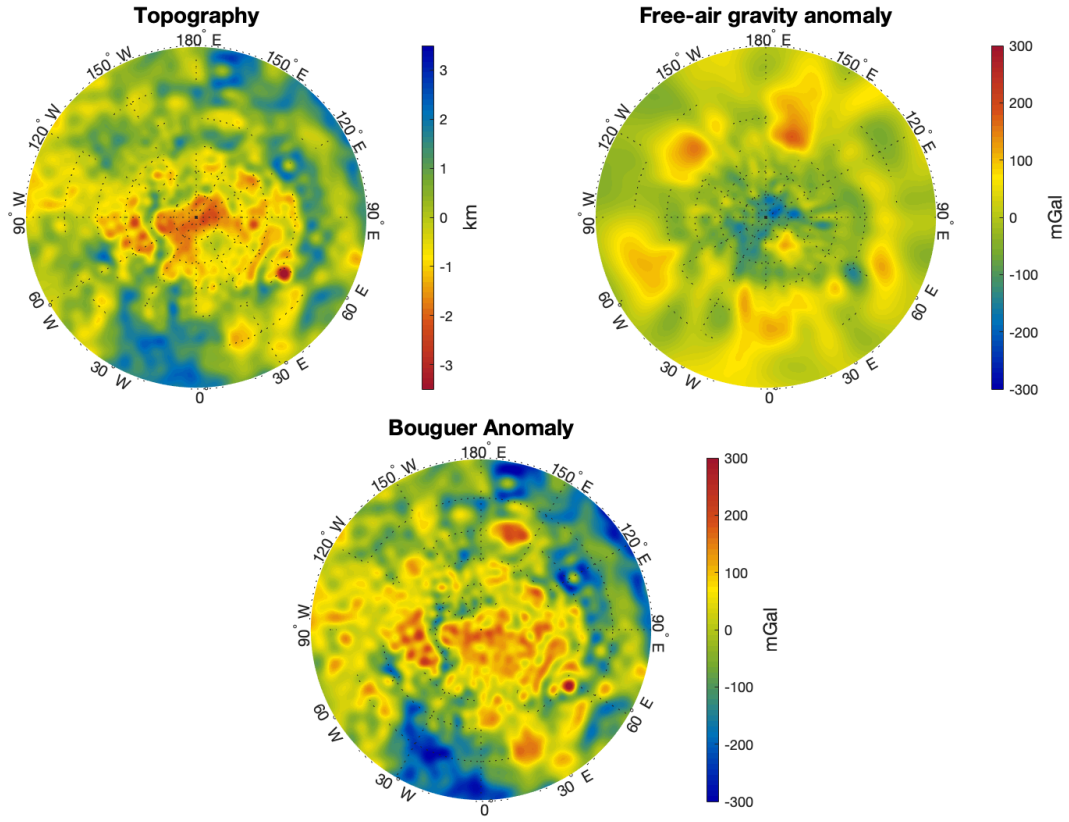

Figure 2.11: (top left) The topographic map of Mercury, computed from spherical harmonic degree 0 - 50, along with the (top right) observed gravity anomalies over Mercury, computed from spherical harmonic degree 0 - 50 with C_{20} = 0 and (bottom) the resulting Bouguer anomaly using a crustal density of 2800 kg/m^3. The figures only cover the northern hemisphere, of the southern hemisphere there is not sufficient data to perform a valuable analysis. (In all plots 0-level is indicated with the same colour. The colourbar for both gravity plots are set to the same range to ease comparison. The topography colourbar is of opposite colours with respect to the colourbars of the gravity plots.)

- The Sobkou basin (134^{o}W, 36^{o}N) has a clear gravity anomaly associated with it - although slightly shifted, making the relation somewhat complicated. In the Bouguer anomaly, the Sobkou basin shows an even stronger gravity anomaly, which might point towards crustal thinning (Smith et al., 2012).

- The Budh basin (152^{o}W, 17^{o}N) is closely related to the Sobkou basin, in that they are located adjacently and 'share' a positive free-air anomaly. The Budh basin is located at the edge of the free-air anomaly and therefore only slightly shows in this map, however in the Bouguer anomaly a small positive anomaly is observed. This might indicate that the Budh basin experienced crustal thinning and is, in contrast to the other basins, is isostatic equilibrium.

- Rachmaninoff (58^{o}E, 28^{o}N) basin is an interesting feature in the Bouguer analysis. In the free-air anomaly the Rachmaninoff basin shows a strong negative anomaly. However, when the Bouguer correction is applied, the gravitational attraction associated with the basin becomes highly positive. Overall, the Bouguer anomaly is considered to be too strong, and the behaviour at the location of this basin is confirming that. The Rachmaninoff is thus not supported merely by crust-mantle relief, and isostasy might play a role here as well.

- The Northern rise (33^{o}E, 68^{o}N), located in the middle of the northern smooth plains, is clearly visible in both topographic and gravity anomaly data. In the Bouguer anomaly this topographic rise 'blends' with its surroundings. The regions surrounding the northern rise are lifted as a whole, leaving the northern rise no longer an outstanding feature.

- The elevated regions near the equator do not show in the free-air anomaly field. In the Bouguer anomaly they are observed very strongly. This indicates that they are probably isostatically compensated.

Aside from the above mentioned specific topographic features, the general view is that the heavily-cratered surface of Mercury induces not so many gravity anomalies. The free-air anomaly field is smoother than the Bouguer anomaly, indicating that the impact craters experience some compensation in either the crust or mantle (Wieczorek, 2015)

2.4.1. Method

In the following crustal thickness calculation methods it is assumed that all gravity anomalies that have remained in the Bouguer anomaly are caused by crust-mantle relief. This is schematically drawn in Figure 2.12. Two (similar) mathematical methods exist that are used to calculate the crustal thickness. To calculate the crustal gravity field, both layers shown in Figure 2.12 are split in several layers to ensure convergence, for more information on why this is done see Section 5.6.

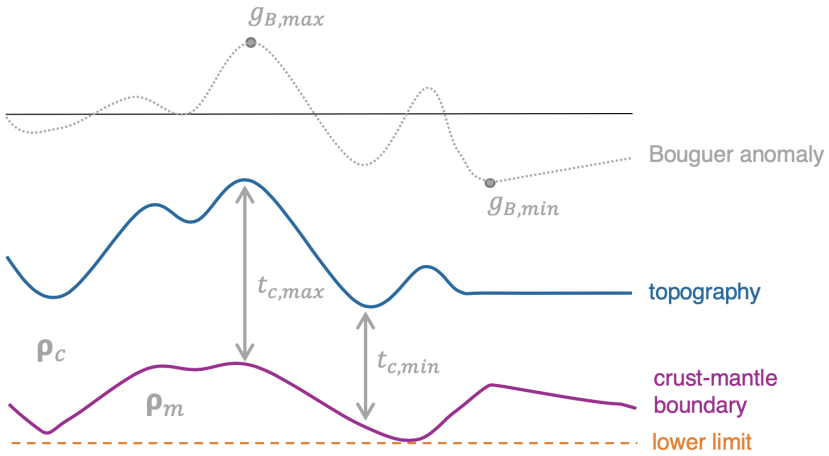

Figure 2.12: Schematic representation of the Bouguer model. The lower limit of the model is set to deepest location of the total crustal root. The parameters $g_{B,min}$ and $g_{B,max}$ are the minimum and maximum value of the Bouguer anomaly.

Downward continuation of the Bouguer anomaly - linear approximation

A simple, but proven to be successful method is a linear approximation of the crustal thickness using a downward continuation of the Bouguer anomaly (Wieczorek, 2015) as given in Equation 2.6. This formula requires an assumption on the minimum and maximum crustal thickness, $t_{c,min}$ and $t_{c,max}$, that can be made based on literature. The maximum, minimum and local Bouguer anomalies, $g_{B,max}$, $g_{B,min}$ and g_B, can be taken from the calculations on the Bouguer anomaly.

$$t_c = t_{c,max} + \frac{(t_{c,min} - t_{c,max}) \cdot (g_B - g_{B,min})}{(g_{B,max} - g_{B,min})} \tag{2.6}$$

Downward continuation of the Bouguer anomaly - advanced

The second method relies upon the same assumption that crustal variations are responsible for any Bouguer gravity anomaly, however the calculation method is more advanced. This enhancement is in the mass-sheet approximation that is no longer necessary, allowing for more accurate calculations on the crustal thickness. Especially in the case of small planets like Mercury, this improvement is important to consider.

Equation 2.7 reflects the advanced approach. The variable h_{lm} describes the crust-mantle relief in spherical harmonic coefficients of degree l and order m, C^{BA}_{lm} is the Bouguer gravity anomaly in spherical harmonic coefficients, M is the mass, ρ_c is the crustal density, D is the average radial location of the crust-mantle boundary, R is the average radius of the planet. Furthermore, w_l is a spherical harmonic filter, that is to be calculated using Equation 2.8 (Wieczorek and Phillips, 1998).

$$h_{lm} = w_l \left[\frac{C^{BA}_{lm} M(2l+1)}{4\pi\Delta\rho_c D^2} \left(\frac{R}{D}\right)^l - D \sum_{n=2}^{l+2} \frac{(h^n)_{lm}}{D^n n!} \frac{\prod_{j=1}^{n}(l+4-j)}{(l+3)} \right] \tag{2.7}$$

$$w_l = \left\{ 1 + \lambda \left[\frac{M(2l+1)}{4\pi\Delta\rho_c D^2} \left(\frac{R}{D} \right)^l \right]^2 \right\}^{-1} \tag{2.8}$$

Equation 2.7 consists of two terms. As a first step, h_{lm} is calculated using only the left term. In the second step, an iterative approach is taken, in which the right term of the equation is also used. In the case of Mercury, the calculations converge after ~10 iterations. The weighting factor requires an assumption on the Lagrange parameter λ. That parameter is chosen such that w_l=0.5 at degree 40 (Wieczorek, 2015).

2.4.2. Results

The results of both methods are presented together, to allow for easy comparison. The scale of the plots in Figures 2.13 and 2.14 is the same, which is decided upon to enhance the visualisation of how the modelled field compares to the actual gravity field. The crustal model of the Bouguer linear approximation, see also Figure B.2, reflects the topography to a large extent. This is the relatively large magnitude of the Bouguer correction, resulting in a Bouguer Anomaly that follows the topography, aside from some specific locations. Despite the whimsical crustal thickness that is supposed to 'counteract' the topography, the residual gravity field from this crustal model also has an erratic outlook. Especially around the equator the gravity field shows a high level of short-wavelength variations, although from small magnitude. Some of the variations constitute in a relative small area - clearly representing a cratered area. At the poles these topographic variations are lesser and the topography is more smooth (smooth plains), and therefore also the residual gravity field displays this smoothness.

The iterative approach is also based on the Bouguer anomaly. The method involves a filter, that includes high-wavelength crustal variations and derogates short-wavelength variations, hence a smoothed crust. The resulting gravity residual counteracts the free-air anomaly of the northern hemisphere in a large fashion, however it does not with southern part of Mercur. In that area the crustal model seems to introduce gravity anomalies (for completeness a full plot of the Bouguer anomaly is included in Figure B.1). This might be the result of the topography model being more detailed than the gravity model, leading to an asymmetry in the comparison of the two. Although the topographic model is truncated at degree 50, the higher precision is also contained in the lower degrees. It could also well be that this is an example of a topographic feature that is in isostatic equilibrium, hence only shows a small free-air anomaly, and therefore wrongfully emerges in the Bouguer anomaly. The southern part is not of main interest in this analysis, because of the scarcity of available data, and therefore this observation is not considered to be detrimental in the analysis and therefore not assigned any more attention.

Although the two models require the same input data, a large difference between the two models is observed in both the outlook and the magnitude. The average crustal thickness of the two models is similar, and it is mainly the variations in the crustal thickness that are determinant. It is furthermore noted that the truncation of the gravity field highly influences the variation in the crustal thickness, but not necessarily effects the average crustal thickness. When considering what spherical harmonic degrees to include, it is thus of importance to make a careful consideration, to inhibit over- or underestimation of the crustal thickness. In doing so, it is determined what spherical harmonic coefficients and thus what characteristic wavelengths of topographic features are assumed to be counteracted by a Bouguer compensation mechanism. It is likely that long wavelength topography is compensated by crust-mantle relief or deep mass anomalies, while smaller wavelength topography could also be compensated by flexural loading.

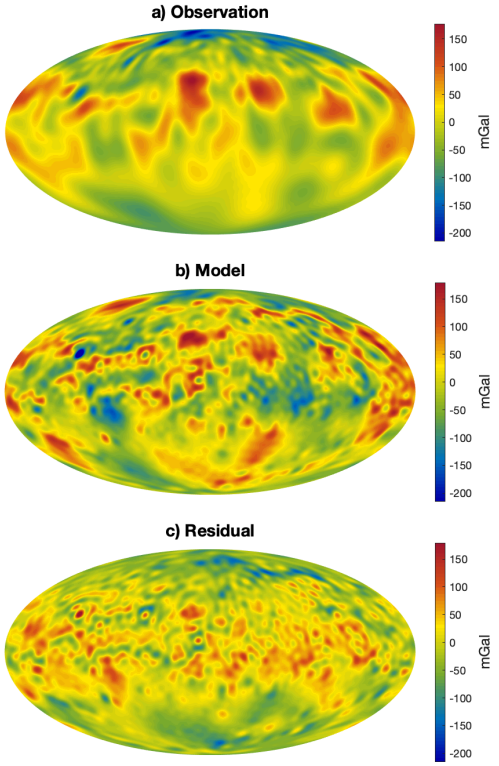

Figure 2.13: Comparison of the free-air gravity anomaly and a crust computed using a linear approximation of the downward continuation of the Bouguer anomaly. (a) The observed free-air anomaly gravity field. (b) Gravity field from Bouguer crust, with ρ_c = 2800 kg/m^3, $t_{c,min}$ = 20 km and $t_{c,max}$ = 80 km. (c) Residual of the two fields. All fields are computed for SH2-50 (C_{20} is excluded). The corresponding crustal model can be found in Figure B.2. Images are in Mollweide projection with a central meridian of 180^{o}E.

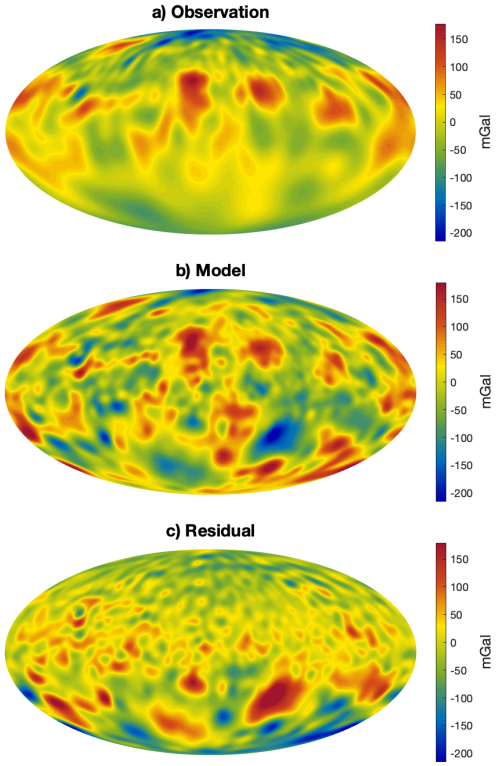

Figure 2.14: Comparison of the free-air gravity anomaly and a crust computed using an iterative analysis of the downward continuation of the Bouguer anomaly. (a) The observed free-air anomaly gravity field. (b) Gravity field from Bouguer crust, with ρ_c = 2800 kg/m^3 and $t_{c,avg}$ = 50 km. (c) Residual of the two fields. All fields are computed for SH2-50 (C_{20} is excluded). The corresponding crustal model can be found in Figure B.2. Images are in Mollweide projection with a central meridian of 180^{o}E.

2.5. Topographic compensation by James et al. (2014)

The poor correlation of gravity and topography and the low or negative admittance values are either an indication of multiple compensation mechanisms for the topography (James et al., 2014) or the consequence of observation uncertainty. James et al. (2014) performed an extended analysis of possible compensation mechanisms in Mercury. In this study, support for the topography is sought in 1) relief on the crust-mantle boundary, 2) deep mass anomalies, 3) lithospheric flexure and 4) lateral variations in density. Filtering of the spherical harmonic domain allowed for investigation of the support mechanisms that are at play in the Northern Smooth Plains, the Caloris Plains, the Heavily Cratered Terrain and the Northern rise. Based on admittance spectra it was concluded that none of the compensations mechanisms fit the data well at all wavelengths. The range of admittance values for the different compensation mechanisms and the imperfect correlation of gravity and topography make it likely that the gravity and topography observations are the results of the superposition of two or more compensation mechanisms. Furthermore, an analysis of the full power spectrum yielded that crustal compensation is likely to play an important role in the topographic compensation at all wavelengths. The admittance values are however too high to be the sole result of crustal thickness variations. Therefore either deep compensation or flexural support is at play, and at lower spherical harmonic degrees it is most likely that deep compensation is important, rather than flexural support. As an important note James et al. (2014) write that deep-seated mass anomalies might be present on the rest of the planet, but that they are largely obscured by yet unobserved crustal thickness variations. The assumptions in the analysis make it impossible to rule out these additional crustal thickness variations. Possibilities for the deep compensation is opted in the perturbation of an interface between layers of different density, compositional layering in the mantle, or effects of temporal variations in temperature and composition and the subsequent lateral density variations. This will be further discussed in Chapter 4.

Any crustal model needs to fit two constraints: 1) the model must reproduce the observed gravity and 2) the weight of the topography must be counteracted by the radial stress on the surface. The two unknowns in this calculation are the relief on the crust-mantle interface and the amplitude of the dynamic load. Whereas previously constructed crustal models, for example that of (Smith et al., 2012) and (Mazarico et al., 2014), were constructed by fitting the Bouguer anomaly and therefore they were a single-layer inversion of the observed gravity and topography, this new approach includes the possibility of deep compensation. The resulting crustal model is given in Figure 2.16 (retrieved via personal communication). ρ_c is set to 3200 kg/m^3 and ρ_m to 3400 kg/m^3, the mean crustal thickness is assumed to be 38 km and the mantle load depth, that is the mean depth of mantle mass anomalies, to be 350 km. The crustal thickness variations contribute more to the topographic relief than to the gravity field, so the crustal thickness map looks similar to Mercury's topography. The analysis is limited by the precision of the gravity field.

Because of the scarce availability of data on the southern hemisphere, the crustal map is only computed for latitudes north of 30^{o}S. As the GSHA software requires the input of a crustal model of the whole planet and thus requires the data points south of 30^{o}S, the incomplete crustal model is enhanced. This completion is performed using the correlation between the topography and the crustal thickness, for the part of Mercury for which the crustal thickness is constructed, see Figure 2.15. The southern part of the planet will not be analysed in much detail because of the scarcity of data points, however the assumption does also have an implication on the gravity field of the rest of Mercury and therefore needs to be kept in mind. This approach implicitly assumes that the topography is dominant in the determination of the crustal thickness, which is not necessarily the case. James et al. (2014) used a dual-inversion method, including both topography and gravity data. It was mentioned that the crustal thickness map looks more like the topographic map than the gravity map for particular reasons, and therefore the correlation between topography and crustal thickness is expected to yield a reasonable estimate in Figure 2.17. Alternatively, the crustal thickness could be set to a constant value or the crust-mantle boundary could be set to a constant depth, however these approaches seem even more arbitrarily. To assess the implication of the assumption with respect to the approach where the crustal thickness would be set to a constant value, also the gravity field of the latter crustal model is assessed in Figure 2.18. Comparison of the two models yield that there are barely any differences, and therefore it is assumed that the taken approach is good. The model in Figure 2.17 will be used in the rest of the research.

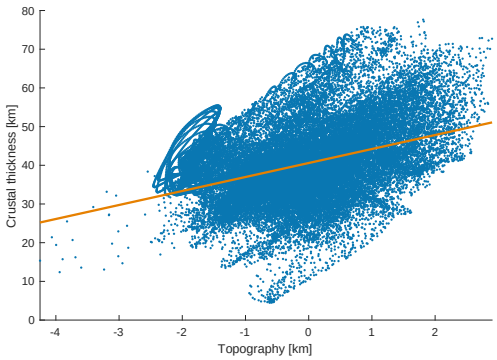

Figure 2.15: Correlation between topography and crustal thickness, as observed in crustal thickness model of (James et al., 2014).

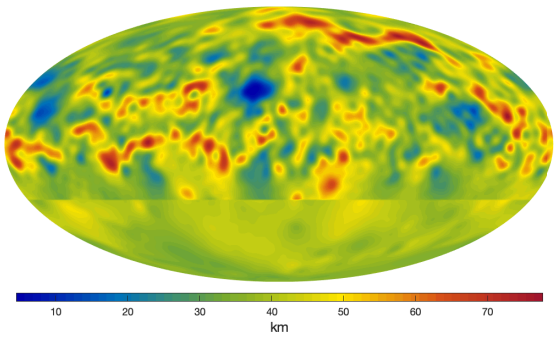

Figure 2.16: Crustal thickness map from (James et al., 2014), retrieved via personal communication. Image is in Mollweide projection with a central meridian of 180^{o}E.

The gravity field that this crustal model produces is presented in Figure 2.17. Although the crustal model does not necessarily show very strong features, the gravity field does. Very interesting is the 'inversion' of the gravity field. Whereas in the observed gravity field the positive anomalies lie around 0^o and 180^o latitude, the crustal model shifts these anomalies by 90 degrees to the west, and leaves negative anomalies where positive anomalies were before. The explanation for this observation is sought in the Bouguer anomaly that is used as input for the calculation of the crustal thickness. The Bouguer anomaly is further investigated in Section 2.4 and it was observed that the Bouguer Anomaly is strong in comparison with the free-air anomaly, and that indeed the Bouguer correction roughly inverts the free-air anomaly in sign. Although the Bouguer anomaly

is not the only input for the crustal thickness calculation, this parameter does strongly reflect in the crustal model. The northern rise is almost fully compensated. James et al. (2014) assign the anomalies of the residual field to deep mantle mass anomalies, and those are further investigated in Chapter 4.

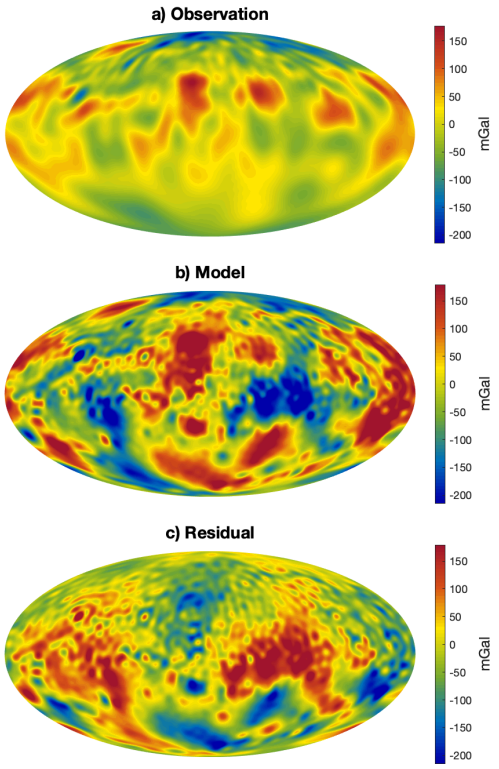

Figure 2.17: Comparison of the free-air gravity anomaly field and the gravity field from the crustal model of (James et al., 2014), enhanced with a varying crustal thickness in the southern hemisphere. (a) The observed free-air anomaly gravity field. (b) Gravity field resulting from James' crust, with ρ_c = 3200 kg/m^3, ρ_m - ρ_c = 200 kg/m^3 and $t_{c,avg}$ = 38 km. (c) Residual of the two fields. All fields are computed for spherical harmonic degree 2-50 (C_{20} is excluded). Images are in Mollweide projection with a central meridian of 180^{o}E.

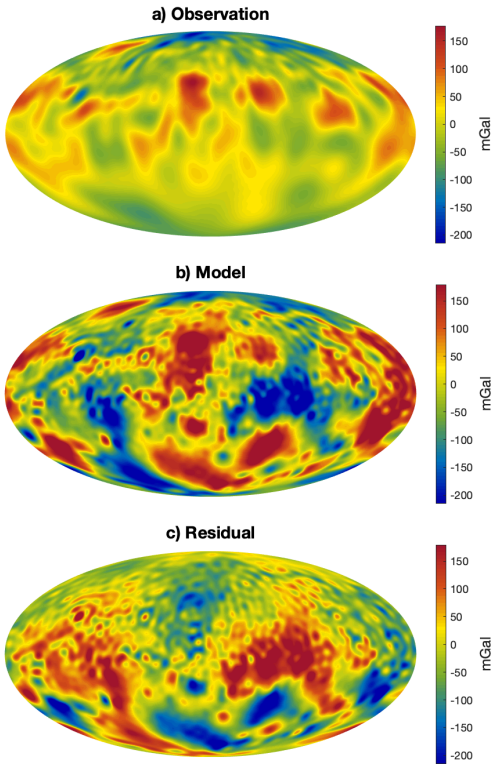

Figure 2.18: Comparison of the free-air gravity anomaly field and the gravity field from the crustal model of (James et al., 2014), enhanced with a constant crustal thickness in the southern hemisphere. (a) The observed free-air anomaly gravity field. (b) Gravity field resulting from James' crust, with ρ_c = 3200 kg/m^3, ρ_m - ρ_c = 200 kg/m^3 and $t_{c,avg}$ = 38 km. (c) Residual of the two fields. All fields are computed for spherical harmonic degree 2-50 (C_{20} is excluded). Images are in Mollweide projection with a central meridian of 180^{o}E.

2.6. Density fitting of crustal models to short-wavelength gravity field

In the previous sections it has been concluded that isostatic equilibrium does most likely not apply to Mercury as a whole, especially not in regions where special topographic features are observed, such as Caloris basin. More likely is the superposition of several compensation mechanisms. In Figure 13 in (James et al., 2014) it is visualised how crustal compensation and deep mantle compensation relate to each other in the spherical harmonic domain. The graph shows that shallow and deep compensation are equally likely, but that there is a preference of each compensation mechanisms for a specific range of the spherical harmonic domain. The compensation depths associated with the observations at SH<10 are ~ 100 km, which can not be explained by crustal compensation. It is therefore likely that deep mass compensation accounts for the majority of gravity anomalies up to SH10. At higher spherical harmonic degrees the topography is more likely counteracted by shallow measures, such as local or regional isostasy and lateral density variations. Furthermore, this distinction between SH<10 and SH>10 allows for analysis of whole planet Mercury, as the gravity measurement over the southern hemisphere are accurate up to SH10 (Mazarico et al., 2014).

The mechanism that is investigated in this section is lateral density variations in either the crust or the mantle. The crustal models from Sections 2.2 and 2.4 are used as input models. These crustal models are based on the gravity and topography field in the full SH domain. The crustal density of the models will be adjusted such

that the crustal model accounts for all gravity anomalies observed in SH10-50. The crustal compensation below SH10 is unadjusted, i.e. no density increments are added or removed to match the observations.

2.6.1. Method

The fitting model works by adding or removing crustal density increments at locations where the modelled data does not correspond to the observed data. The density increment at each longitude-latitude combination is a preset value multiplied with a so-called scaling factor at each location. This scaling factor is determined by normalising the data residual. This operation is iterated until convergence is reached, and per iteration the magnitude of the preset density value can be varied. The convergence criteria is said to be met when the residual at each location falls within a predefined range such that it does no longer allow for observable granularity in the residual of the fitted SH domain. This range is set to ±20 mGal at 0 km altitude for fitting of the gravity anomalies between SH10-50.

Within this fitting process the density increment can be added in two places, that is either in the crust or in the mantle. The top layer is now modelled as two layers - one crustal layer of which the thickness is based on the chosen physical principle, and one 'mantle layer' that reaches as deep as the preset depth of the analysis, constant across the whole surface. Density increments could be added to both crustal and mantle density (but for simplicity is now only done one at at time - so either crustal increments or mantle increments) and the sensitivity of the model is tested for both. The fitting procedure is also used in (Root et al., 2017). A diagram of the process is given in Figure B.3, which is a simplified version of Figure 4.1.

2.6.2. Results

The results of the fitting procedure are shown in Figure 2.19 for the Airy-Heiskanen crustal model with the distinction between fitting via crustal density increments and mantle density increments. In the left plots the density map after the fitting process is plotted. For the crustal density variation analysis this map is of the crustal density, for the mantle density variation analysis this map is of the mantle density. For both maps the same variation in the density is used for plotting, namely ±150 kg/m^3, to enhance the comparison (please note: the maximum and minimum values are different). The resulting residual in the gravity field is displayed in the middle plots. The right plots show the results in terms of spherical harmonic coefficients.

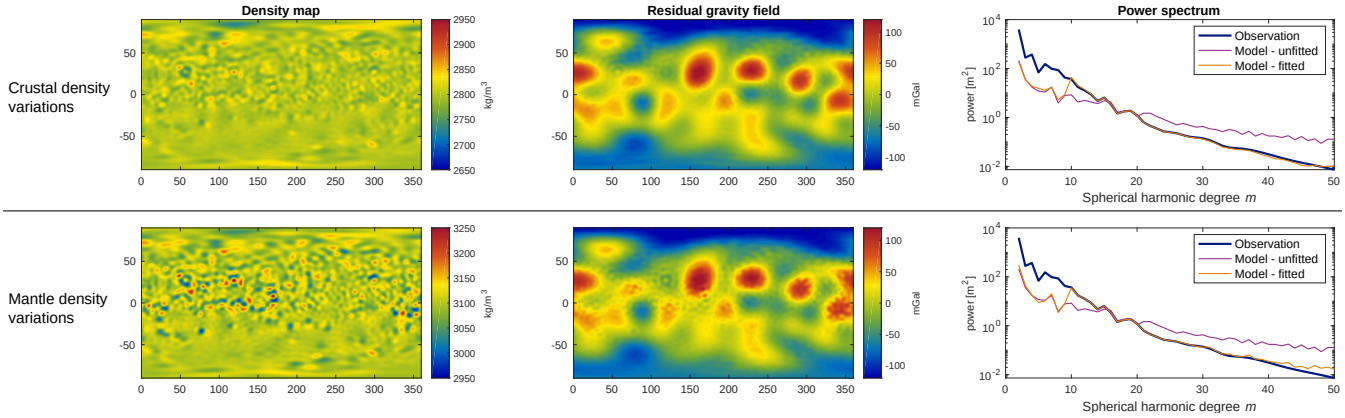

Figure 2.19: Crustal model for Airy-Heiskanen compensation assumption with ρ_c = 2800 kg/m^3, ρ_m = 3100 kg/m^3 and t$_{c,avg}$ = 50 km, fitted to the gravity by adding (top) crustal density increments and (bottom) mantle density increments.

Both fields still show some level of granularity. From the spectral plot it can be read that this granularity is caused by short-wavelength variations. The granularity is heavier in the model that is fitted using mantle density increments than in the model that uses crustal density increments. This is however expected to be the consequence of the settings in the fitting algorithm (mainly the convergence criteria and the fitting increment) and, in case one of these crustal models is required in later stages, the models can be further refined without changing the software largely. Furthermore, in Figure 2.3 is is clear that from SH40 onward the uncertainty in the gravity model is as large as the actual magnitude of the model, leaving the coefficients that cause the observed granularity unreliable.

A more interesting discrepancy between the models is observed in the density maps. In these maps it is seen that fitting via mantle density variations requires larger density increments than would be required when the gravity field is fitted with crustal density variations. This is the result of the centre of mass of a mantle density increment being located at a further distance than a crustal density increment would. Furthermore plays the thickness of the layer also a crucial role. The crustal models are constructed such that they contain the full crustal layer, and the mantle layer is only extended to the deepest root of the crustal layer. The mantle layer is thus relatively thin compared to the crustal thickness, 30 versus 47 km, and this explains the large density increments required to fit the crustal gravity field. If the mantle layer would be as thick as the crustal layer, the mantle density increments would be of a smaller magnitude than currently modelled, however still larger than the crustal density increments.

The lay-out of the density maps resemble the cratered landscape of Mercury. The craters are clearly visible in the topographic data, but not so much in the gravity data. The crustal model is based on the topography of Mercury and therefore shows high resemblance with that field. The discrepancy between the observed gravity and crustal gravity is therefore expected, and also that the fitting process will require density variations accordingly, to account for the discrepancy. Varying density in and around the craters is not uncommon. Impact events can induce partial melting of the mantle, and eventually lead to opening up of a new mantle region with new mantle material (Weider et al., 2015). Furthermore can impact ejecta spread around the crater, also inducing density variations. Density variations in both the crust and mantle can thus be explained by the impact events. The rather whimsical variations are more likely to exist in the crustal density field than in the mantle density field, because of the differences in viscosity. In the mantle, density variations are expected to be smoother than within the crust, and it is thus unlikely that the mantle density map displayed in Figure 2.19, with its granular outlook, holds.

The variation in the modelled crustal density is roughly ± 50 kg/m^3, which is considered to be a reasonable variation given possible variations in crustal material and the level of porosity.

- As was indicated in Table 2.1, the range for the estimates of the average crustal density of Mercury is rather broad, namely 2700 - 3200 kg/m^3. With the current settings of the algorithm, the crustal density variations remain well within these bounds. Weider et al. (2015) found substantial compositional variations across the surface of Mercury. They explained these observations by differences in mantle composition, potentially triggered by an impact event, temperature variations, oxygen fugacity and the depth. The difference in composition obviously also implies a difference in crustal density. Considering the crustal density ranges for Mercury as used in literature, it is expected that these observed compositional differences could induce the difference within the crust of Mercury.
  The resulting (upper) mantle density range is 2900 - 3600 kg/m^3. The mantle density that results from the fitting process requires much lower values, which are considered unrealistically low densities.

- Porosity in Mercury's crust and mantle can also cause crustal density variations. For Mercury porosity levels are unknown. However, for the Moon, often mentioned in close relation to Mercury, porosity levels are found to be up to 12%, or density variations of ± 250 kg/m^3. Furthermore, for the Moon it is observed that the porosity correlates with impact craters. (Wieczorek et al., 2013)

The comparison of crustal and mantle density differences leaves crustal density increments most probable, because of the seemingly relation between density variations and impact basins. and therefore this method is investigated for the other physical theories that are used for crustal modelling. The results of the analysis are plotted in Figure 2.20. The initial models, i.e. the models that are used as input for the fitting algorithm, are the models that were presented earlier in this chapter.
The observations:

- For all 4 methods it is observed that the fitting process is clearly applied to SH10 and higher, and that the coefficients of smaller degrees are almost unaffected. This is validation of the algorithm, but also indicates that density variations that are required to match the topographic gravity with the free-air anomaly do not affect the gravity of lower degrees. The spherical harmonic degrees are independent of each other.

- The crust computed in the Bouguer linear approximation shows the lowest residual field. The corresponding density map is within realistic bounds. This can be explained using the nature of the theory:

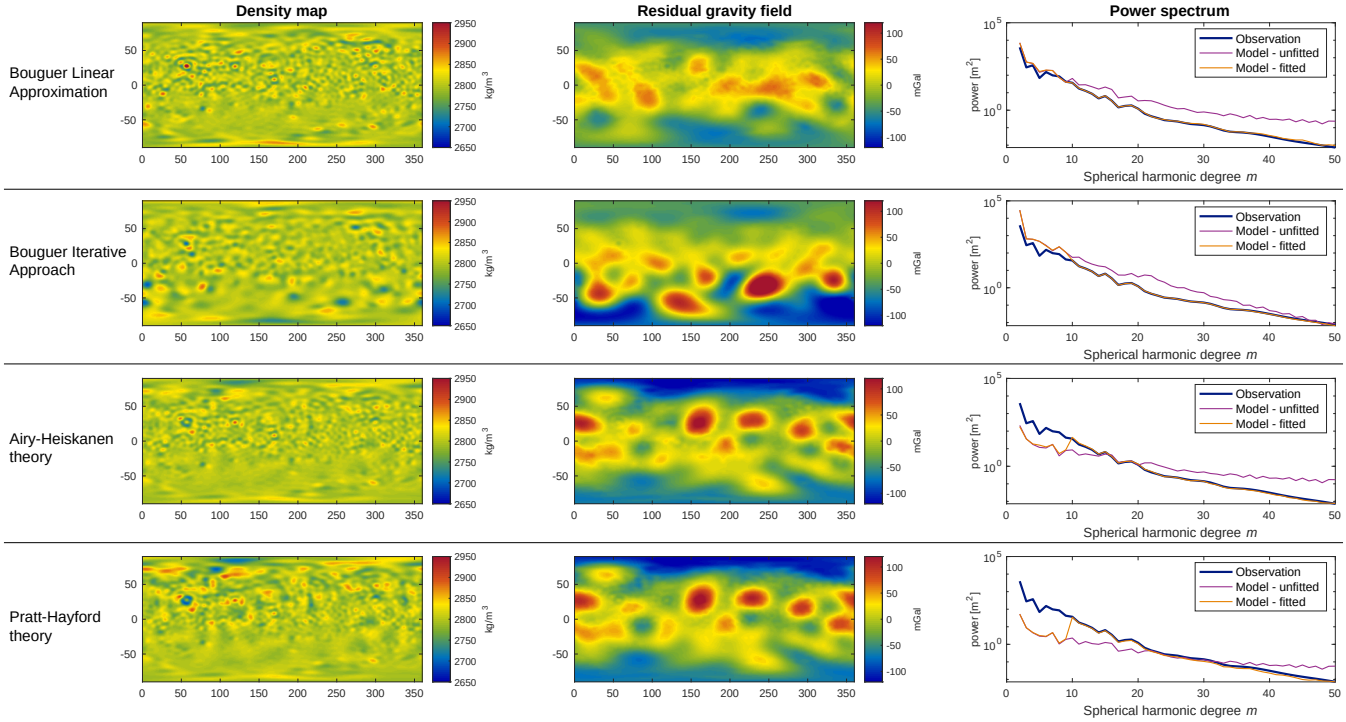

Figure 2.20: Results of the fitting process for the various crustal models that resulted form different mathematical theories. The left plot shows the final crustal density map. The Pratt density map only contains the density variations as a result of the fitting process, and not the density increments initially needed to achieve isostatic equilibrium. The middle plots show the residual field, that is the free-air anomaly minus the crustal gravity field, both in spherical harmonic degree 2-50 with C_{20} removed. The right plots show the results in terms of spherical harmonic coefficients. Note that in each column the same y-axis scale is used.

the crust is fitted to the Bouguer anomaly. The Bouguer anomaly is not necessarily similar to the free-air gravity field, however as all gravity anomalies resulting from spherical harmonic degree 10 and higher coefficients are fitted, the remaining residual is in degree 9 and lower. The Bouguer Linear approximation resembles this lower-degree gravity field well, and thus leaves a small residual.

- The crustal model of the Bouguer iterative approach requires relative few fitting and thus not that large density increments. The remaining residual is however rather large, and appears in an unexpected location, namely in the southern hemisphere. The strong residuals are mainly of positive sign, and a these locations the other Bouguer approach shows a light negative anomaly. The two approaches are thus clearly different. This anomaly in the southern hemisphere is hard to analyse, because of the scarce availability of data in this region.

- The fitted Airy-Heiskanen and Pratt-Hayford models shows a highly similar density and residual field. The long-wavelength coefficients of Airy are slightly larger than those of Pratt, resulting in smaller density increments in the Airy model than in the Pratt model. The effect is very minor, because of the large magnitude of the coefficients. Although the models produce a similar gravity field, the crustal models themselves are very different. While the Airy-Heiskanen theory requires only slight density variations - the rest of the free-air anomalies are compensated through crustal thickness variations -, the density variation for Pratt-Hayford is much larger as the only fitting parameter is the density - the crustal thickness is constant. The density variation for Pratt might be considered unrealistic, as not only the variation is broad, also does it require the full density spectrum in relatively small regions, for example across the equator. One could therefore argue that a combination of crustal thickness and density variations is more likely. On the other hand, the whimsical crustal thickness of the Airy-Heiskanen problem is also disputable. Therefore a smoothed crust-mantle boundary in combination with density differences might be the most optimal solution.

In this analysis it is assumed that the deep mass anomalies are encaptured in spherical harmonic degree 10 and lower, and that all gravity anomalies of spherical harmonic degree 10 and higher are accounted for in the upper mantle and crust. The validity of this assumption is further investigated in Section 5.7.

2.7. Conclusion

The theory of isostasy is proven to be well applicable to Earth (Watts, 2001). Mercury is, however, an undiscovered planet, about which many questions remain and for which it is not known whether the assumption of isostasy is valid. The limited availability of observational data hinders the progress in understanding Mercury. Therefore, although the principle of isostasy seems rigorous, it is one of the best measures we have to approximate the crustal thickness, in our attempt to better understand the internal structure of Mercury. The fully Airy-Heiskanen compensated and the fully Pratt-Hayford compensated crusts result in a similar residual gravity field, that also look much alike the free-air anomaly.

The Bouguer anomaly can give insight into the compensation mechanisms that are at play on Mercury. In several articles (for example (Smith et al., 2012) and (Wieczorek, 2015)) the Bouguer anomaly is analysed, and conclusions on compensation mechanisms of specific special features on Mercury are drawn from the observations in the Bouguer anomaly. The Bouguer correction is of stronger magnitude than the free-air anomaly, which is observed on more planets (Qingyun et al., 2018). Because of the uncertainty in the crustal composition and thus crustal density of Mercury, it is difficult to draw any conclusions for Mercury. Despite this, the Bouguer anomaly can be used in two mathematical approaches to calculate crustal thickness: 1) a linear approximation and 2) iterative approach. These models both use the same input data, but use this in a different fashion, resulting in two different crustal models. The iterative approach gives a more smoothed crust, because of short-wavelength features that are assumed to be compensated by the crustal strength, not showing any variations in crustal density or thickness, and that are thus filtered out. Both crustal models result in a relative small residual gravity field (the part of the gravity field that is not accounted for in the crust).

The crustal model that James et al. (2014) developed showed very interesting results, in which the residual gravity anomaly field showed a shift in the location of the "C22-lobs" as opposed to the observed free-air anomaly field. The crustal model is rather advanced with respect to other crustal models, because it relies on thorough analysis of different data sources and includes comparison with others planets. The crustal model is the result of a dual-inversion of topography and gravity models, in which the authors solve for mantle dynamic flow and crustal thickness. The residual gravity field can therefore be assumed to be caused by deep mass anomalies and the expected location of these deep mass anomalies from the residual, make the model so intriguing. The crustal model in the southern hemisphere is computed using the relation between topography and crustal thickness that is observed in the northern hemisphere, because of poor resolution in the data on the southern hemisphere.

The crustal models that have a crustal density adjusted such that they fit the gravity field in the short-wavelength gravity domain, can be categorised in two types: 1) Bouguer models and 2) local isostasy models. These types are based on two different theories, and therefore it is plausible that the models within one theory show similar results, and that between the two types discrepancies are observable. By fitting the crust to the free-air anomaly that corresponds to spherical harmonic degree 10 and higher, one essentially assumes that all gravity that is captured in spherical harmonic degrees smaller than 10 are caused by deep-mass anomalies, apart from the gravity that was already counteracted in that specific spherical harmonic domain by the initial model. This assumption (spherical harmonic degree (SH) <10 = deep mass anomaly) is roughly valid for Earth (Root et al., 2016) and research on Mercury points towards the same rule (James et al., 2014; Padovan et al., 2015). Therefore, these fitted models are expected to provide a constraint in the identification of deep-mass anomalies, while still capturing the effect of crustal compensation of topography. Because the the two isostatic models do not show large discrepancies in the residual gravity field, one of them is continued in the coming part of the research. As Sori (2018) stated it is unlikely that Pratt-Hayford isostasy plays a major role on Mercury, the Airy model is continued with. From the Bouguer approaches the linear approximation is used. The iterative approach mainly shows anomalies in the southern part of Mercury, of which the availability of data is scarce, and therefore this region is of less interest. The crustal model resulting from the linear approximation is therefore better suited.

The selected crustal models, *AiryFitted*, *BLFitted* and *JamesCorrelation*, that are continued with are pictured in Figure 2.21. In this chapter the gravity field was used as input because of its sensitivity to crustal variations, however in Figure 2.21 the Hermeoid is shown as it is most sensitive to deep mass anomalies. The depicted range of crustal models allows for the investigation of almost the full range of possibilities, namely 1) no significant crustal compensation, 2) 90^o shift of free-air anomalies and 3) something in between: an equatorial band of deep mass anomalies. Of course other outlooks of the residual fields are also possible, however given the gravity and topography data these models are most likely.

Another important conclusion from this analysis is that the observed gravity field is not directly linked to the topography. The observed anomalies are thus not necessarily caused by crustal variations, neither is this evidence for compensation by deep mass anomalies. Both options (crustal and deep mantle compensation) are still possible explanations for the observations, and the latter option is analysed in more detail in this thesis.

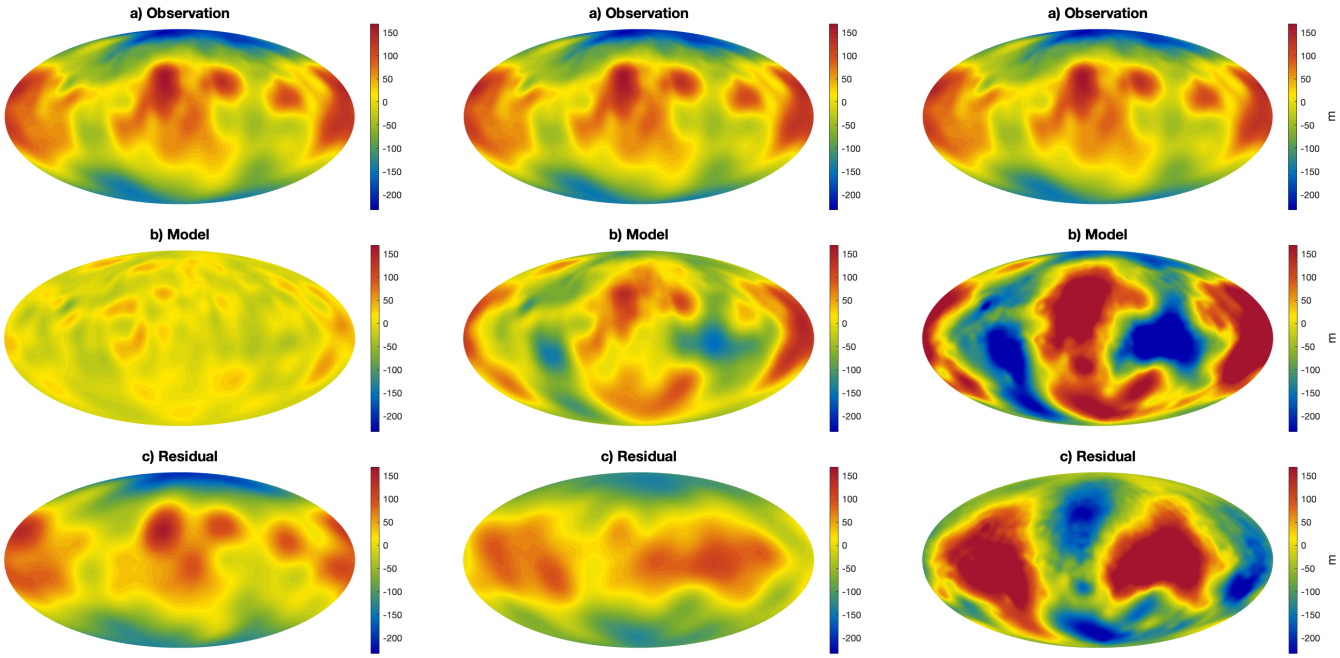

Figure 2.21: (a) Observed Hermeoid, (b) Hermeoid from crustal models, from left to right: *AiryFitted*, *BLFitted* and *JamesCorrelation* and (c) Residual after subtraction of crustal gravity field from observed gravity field. All values are in meters. Images are in Mollweide projection with a central meridian of 180^oE.

Flexural isostasy is also analysed in a preliminary fashion. This theory prescribes that Airy-Heiskanen local isostatic compensation is likely for spherical harmonic degrees smaller than ~10 (dependent on the assumption on elastic thickness), which complies with the previously stated assumptions. For larger degrees, the compensation is expected to be a combination of Airy-Heiskanen and Bouguer compensation and eventually, when the spherical harmonic degree is sufficiently high, solely Bouguer compensation is at play. Analysis of flexural isostasy worsened the fit to the observations and is therefore omitted. Development of a new crustal modelling method based on this principle is not considered to be within the scope of this thesis.

3

Volcanism

On the surface of Mercury several indications of volcanism are observed. Smooth plains are large crustal regions that have a crater size-frequency distribution that suggests that they were emplaced after the heavy bombardment of Mercury. The plains show clear indications of flooding and shorelines. Furthermore have the plains a distinct colour and composition (Denevi et al., 2013). Next to the smooth plains are there also signs of pyroclastic activity. Pyroclastic deposits are explosive volcanic eruption signatures, that are the result of the fragmentation and eruption of magma particles, propelled through the expansion of volatile species released from rising bodies of magma (Kerber et al., 2011). In this chapter the relation between the different residual models from Chapter 2 and the volcanic features if further assessed. Given the proposed relationship between LLSVPs on one hand and LIPS and hotspots volcanism on the other hand, it is hypothesised that a relation between the volcanic activity on Mercury and deep mantle mass anomalies exists. In Figure 3.1 the raw data is displayed, i.e. the location of the volcanic features without the relation the the geoid. The exact locations, size and age data is included in Table B.1.

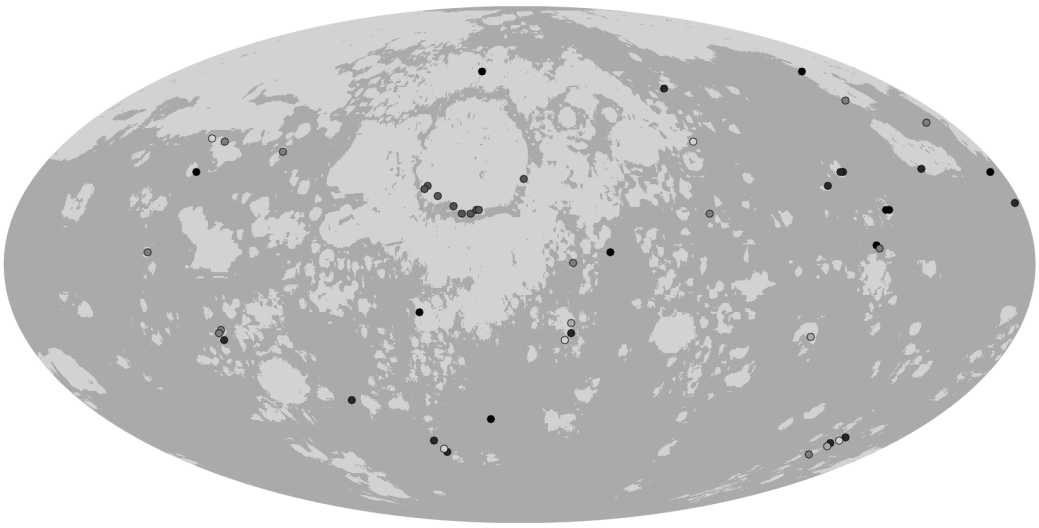

Figure 3.1: Location of the smooth plains and the pyroclastic vents on the surface of Mercury. The smooth plain data was retrieved from (Head and Wilson, 2015, Figure 40.8). The pyroclastic vent data has been displayed in various shades of grey, indicating different age classes, please see Figure 3.3 for the labelling. The data is from Goudge et al. (2014). Image is in Mollweide projection and has a central meridian of 180^{o}E.

3.1. Smooth plains

In Figure 3.2 the contours of the smooth plains observed in image data, as mapped by Denevi et al. (2013) and Head and Wilson (2015), is pictured over the various residual Hermeoids from the crustal models. The crustal models are assessed for their relation between the Hermeoid and the location of the smooth plains.

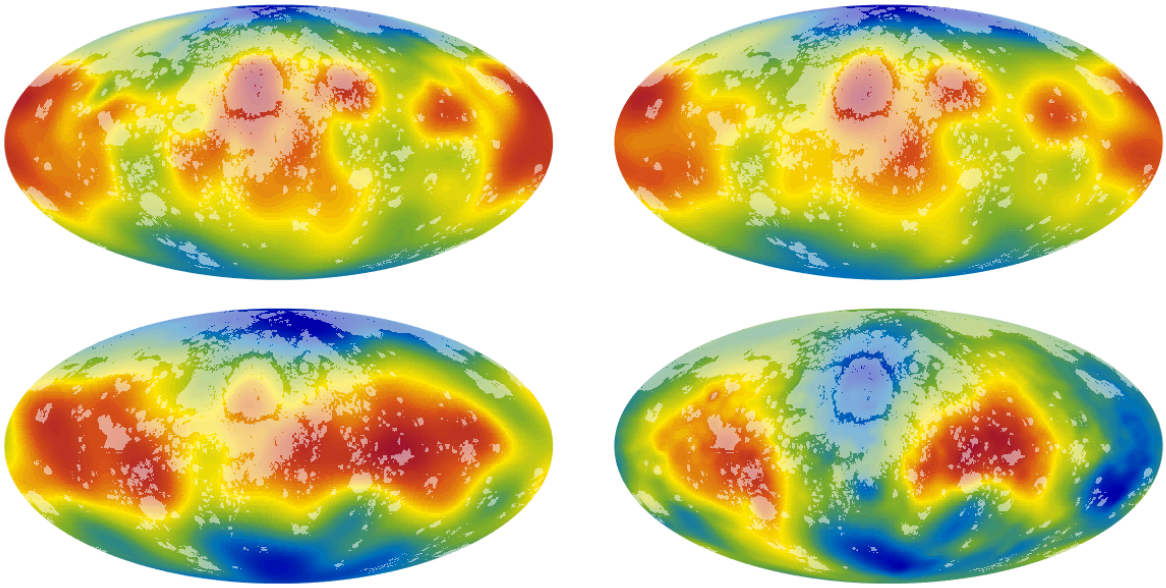

Figure 3.2: Distribution of smooth plains pictured on top the Hermeoid after subtraction of (top left) nothing (unadjusted Hermeoid), (top right) crustal model of Airy-Heiskanen, (bottom left) crustal model of Bouguer linear approximation and (bottom right) crustal model from James et al. (2014). The outlook of the smooth plains are indicated by the white overlay, retrieved from (Denevi et al., 2013). The colours indicate the magnitude of the scaled residual Hermeoid, on a scale from -1 (blue) to 1 (red). Images are in Mollweide projection and have a central meridian of 180^{o}E.

In Figure 3.2 the residual fields that results from the different crustal models are graphically overlain by the contours of the smooth plains as defined by Denevi et al. (2013). The top figures are the Hermeoid and the residual Hermeoid from the Airy crustal model. It was already observed that these fields are highly similar, i.e. the Airy crustal model does not interfere with the large gravity anomalies. The majority of the smooth plains is in these models located over the negative (blue) gravity anomalies in the northern hemisphere. For the negative anomalies on the southern part of the planet this relation is not observed, this could however be due to a lack of data. These two models show that the Caloris basin and its positive gravity anomaly are clearly associated with the smooth plains, both in and surrounding the basin. Also the Subkou basin, located to the east of Caloris, has a clear smooth plain over it. One could also argue that the smooth plains directly north and west of Caloris relate to the edge of the gravity anomaly, rather than to Caloris basin. The same relation seems to hold for the other positive gravity anomaly (in the figure located partially to the left and partially to the right of the Caloris basin); the smooth plains to the north of that anomaly stop at the 'yellow boundary', i.e. the edge of the LLSVP. Furthermore are some smaller smooth plains also located on its edge.

The James model in the bottom left figure of Figure 3.2 is totally different than the top figures, therefore the relation with the smooth plains is also different. In James' model the smooth plains mainly correspond to negative gravity anomalies, however the smooth plains also occur on the location of the LLSVPs and at the edges. The gradient in the shape of the smooth plains at the southeastern part of the Caloris basin shows the same gradient as the underlying LLSVP. The same but to a lesser extent holds for the gradient at the south-western edge. Despite these two relations, the smooth plains roughly show less correspondence with the residual field of James' crustal model. The Bouguer residual shows a broad band over the equator of positive gravity anomalies, and this is not in agreement with the outlook of the smooth plains. Apart from the concentration of the plains over the northern negative part, it is very difficult to observe any other relation between the smooth plains and the gravity residual.

To summarise, the unadjusted Hermeoid and the gravity residual of the crustal model that shows the highest level of resemblance with this anomaly, the Airy model, show the greatest correspondence with the smooth plains. However, the question remains whether these relations truly exist in Mercury, or that the suggested connections are too far-fetched. In any way, it can not be ruled out that a relationship between deep mantle mass anomalies and the smooth plains exists.

3.2. Pyroclastic deposits

Pyroclastic deposits can be located on Mercury using image data. The deposits are identified based on their spectral character, morphology and surface texture. They are characterised as irregular central depressions, appearing as bright signatures with diffuse edges. Furthermore do these pyroclastic deposits show a distinct spectral signature, that can be compared to the spectral characterisation of pyroclastic deposits observed on the Moon. (Blewett et al., 2011; Goudge et al., 2014)

A combined dataset of the pyroclastic deposits on Mercury is constructed from Kerber et al. (2011); Blewett et al. (2011); Goudge et al. (2014), resulting in a total number of 51 pyroclastic deposits spread over the planet. The currently identified pyroclastic deposits are, in comparison with the deposits on the Moon, relatively large, but this could be the consequence of the low resolution of the data (Kerber et al., 2011). Also, the pyroclastic deposits on Mercury seem to be redder and brighter in comparison with the surrounding terrain than is observed on the Moon. Furthermore, relatively few pyroclastic deposits have been identified on Mercury, but this could also be due to the sparse availability of data. Another explanation could be that pyroclastic deposits are simply less common on Mercury - because of a required specific combination of physical characteristics -, or that some of the deposits have been buried by other types of deposits (Kerber et al., 2011). Another important note made by Kerber et al. (2011) is that the incidence angle plays an important role in the visibility of the deposits in spectroscopic (low incidence is preferable) and morphologic (high incidence is preferable) data. Most deposits are identified on locations where the incidence angle was moderate, which might indicate that some deposits are still 'hidden' due to an undesirable incidence angle (Kerber et al., 2011).

Most of the pyroclastic deposits on Mercury, namely ~90%, are observed within or on the edges of impact craters and basins (Kerber et al., 2011). Some clustering is observed around the rim of the Caloris impact basin, and in an around large impact craters (Goudge et al., 2014). However, in general, the distribution of the deposits can be considered global, which indicates that the location of heat-producing elements is evenly distributed across the planet, or that the crustal thickness is relatively uniform (Kerber et al., 2011). A possible explanation for relation between the location of pyroclastic deposits and the location of impact basins is given by Goudge et al. (2014), who argue that the collision event could have fractured and thinned the upper crustal layer such that the propagation of magma-filled dikes was enhanced. Thermal contraction of Mercury has induced a high stress rate in the crust, and therefore it could in general be difficult for magma to penetrate through the crust. Possibly only at these 'weak crustal locations' the penetration could have been successful.

Despite the already observed correlation between pyroclastic deposits and impact basins, also the relation between the deposits and the Hermeoid is analysed. The Large Low Shear-Velocity Provinces (LLSVPs) in Earth are mentioned in relation with the C_2 geoid undulation (Anderson, 1982), hotspot volcanism and Large Igneous Provinces (Torsvik et al., 2006). The geoid undulation in the Earth's gravity field is *approximately* at the location where the LLSVPs are observed in seismic data. The volcanic features are observed at the edges of the LLSVPs, where the shear-wave velocity gradient is highest.

As seismic data is not available for Mercury, it is not possible to identify the location of the highest shear-wave velocity gradient. Instead of this, the approximate analogy between the location of these gradients and the edges of the gravity anomaly is used. In Figure 3.3 the location of pyroclastic vents in relation with the Hermeoid is visualised. The location of the pyroclastic deposits are mapped onto the the residual Hermeoid of several theoretical models that remain after subtraction of the different crustal models from the Hermeoid. Also, histograms are included that represent the distribution of the pyroclastic vents over the Hermeoid.

Firstly, the location of the pyroclastic deposits with respect to the Hermeoid are assessed (and thus *without* considering the different colours). In the Hermeoid it is observed that the pyroclastic deposits have the tendency to appear rather in higher Hermeoid regions than in lower Hermeoid regions, although this preference is not very strong. Furthermore, some grouping between -50 and +50 m seems to occur, which could point towards the edges of the LLSVPs that are hypothesised to be located where the Hermeoid switches sign. This would thus be an indication of the pyroclastic vents occurring at the LLSVPs edges.

Although the Airy model looks much like the Hermeoid, the spread of pyroclastic deposits is quite different. The pyroclastic deposits are more often located on the positive regions of the Hermeoid, and there is no longer an obvious concentration at a certain magnitude of the Hermeoid. For James' Hermeoid a similar note

can be made: there is not concentration around a certain Hermeoid value, however the pyroclastic deposits appear more often on location of negative Hermeoid. Both the Airy and James crustal model thus alleviate the relation between pyroclastic deposits and the edges of the LLSVPs, and are in favour of a relation between pyroclastic deposits with crustal/topographic features.

The Bouguer model shows again a different relation. The pyroclastic vents spread more evenly over full range of Hermeoid values, with a relatively strong preference for the positive parts. The pyroclastic vents thus mostly occur in the hypothesised LLSVPs, rather than on the edges.

The pyroclastic vents are further segregated based on age, depicted by the various shades of grey (Goudge et al., 2014). The geologic history of Mercury is divided into five periods, using a time-stratigraphic assessment of the surface (Head et al., 2007). By assessing the degradation state of the impact craters that host the pyroclastic deposits, the pyroclastic deposit can be assigned an 'upper age limit', i.e. a limit to its maximum age. This analysis does not necessarily show that there is a relation between temporal and spatial spread of the deposits over the planet, rather does this analysis suggest that the emplacement of pyroclastic deposits on the surface of Mercury took place over a prolonged time interval. This would then also confirm longevity of potential LLSVPs.

Although these observations do not rule out the existence of a relation between smooth plains, pyroclastic deposits and LLSVPs/Hermeoid undulation, the indications are not strong. Kerber et al. (2011) and Goudge et al. (2014) already concluded that the pyroclastic deposits show a strong correlation with the location of impact basins and craters. The parts of the crust that are weakened because of collision allow for the penetration of magma to the surface. This reasoning seems very likely, and it does not rule out the relation between the Hermeoid and possible mantle upwellings. There exist several different views on this matter:

- The high stress rate in the crust because of the thermal contraction of Mercury, might have prevented the mantle upwellings from reaching the surface. In that case, they are not visible as pyroclastic deposits or other volcanic features on the surface, however do exist in the mantle.
- Possibly not all pyroclastic deposits on Mercury are identified. The relatively large average size of the deposits might indicate that the smaller deposits are too small for the resolution of the data, and the incidence angle of the instruments has possibly obscured some of the deposits too. Although it is likely that the currently located deposits cover the planet on a global scale and therefore represent the deposit is a good fashion, this can not be concluded with 100% certainty.
- It is also a possibility that some of the deposits over time have been covered by other volcanic processes. The smooth plains that are covering Mercury globally, could potentially obscure previous pyroclastic vents.
- The geoid undulations that are associated with the LLSVPs in Earth do not exactly correspond with the location of the LLSVPs as seen in seismic data. This could distort the relation.
- Brož et al. (2018) numerically investigated the absence of kilometre-sized pyroclastic deposits. In his paper he argues that the these deposits are not necessarily absent, they do however not show as topographic features. One should thus use other information sources, such as compositional data, that could possibly be retrieved from BepiColombo.

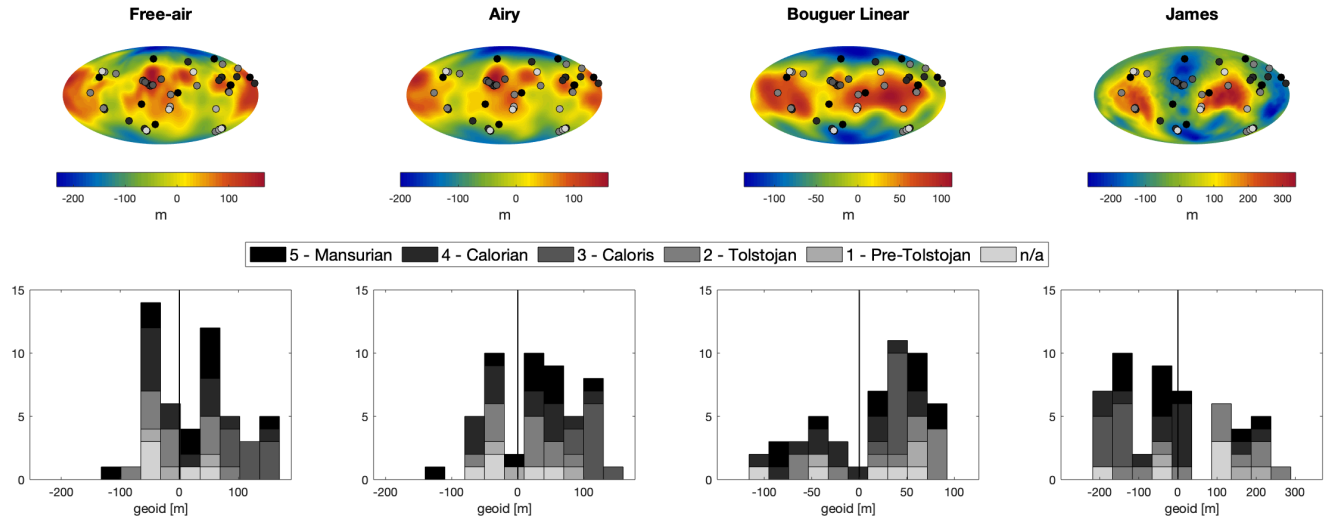

Figure 3.3: Categorisation of pyroclastic deposits by magnitude of Hermeoid at the location of the deposit, grouped by the age of the host crater of the deposit. Host crater age data according to (Goudge et al., 2014) retrieved via personal communication. Mansurian: 1 - 3.25 Ga, Calorian: 3.25 - 3.9 Ga, Caloris: 3.9 Ga, Tolstojan: 3.9 - 4.0 Ga, Pre-Tolstojan, 4 - 4.5 Ga (late heavy bombardment). Age data from Head et al. (2007). Images are in Mollweide projection and have a central meridian of 180^{o}E.

4

Deep Mantle

After the investigation of the crustal features and their possible compensation mechanisms, the constructed crustal models can be used as baseline for the in-depth investigation of deep mantle mass anomalies. This process is structured in three substeps. An initial investigation on mass anomalies is performed on a predefined search space for thickness and density variations, with the aim to develop a sense for the magnitude of deep mass anomalies in Mercury in Section 4.1. This analysis is in Section 4.2 followed by the assessment of how core-mantle boundary topography could account for the observed gravity anomaly. In Section 4.3 the developed algorithm is in the third phase expanded to allow for the investigation of the effect of a temperature anomaly in the mantle of Mercury. The implication of this possible temperature anomaly, and its consequent phase transitions and inherent density variations are taken into consideration. The aforementioned substeps include the investigation of a wide variety of causes for the observed gravity field. This is the inevitable result of the limited availability of data and therefore knowledge about Mercury, and specifically its interior.

In all models, the Hermeoid is taken as the input parameter, i.e. the C_0, C_1 coefficients and the C_{20} coefficient of the gravity field are omitted.

4.1. Density and thickness variations in basal layer

The possibility of a dense basal layer at the CMB of Mercury has been proposed before. The existence of this layer has been suggested to explain the low Fe-abundance observed on the surface of Mercury. However, little research on the shape and the consistency of this layer has been performed, hence this interior feature of Mercury is poorly understood. Hauck et al. (2013) used a thickness range of 0-200 km for the dense basal layer, and assumed a density within 3600-5400 kg/m^3. Using the constraints of the remainder of their model, assuming a crustal and mantle density of 2800-3600 kg/m^3 and a crustal thickness of 0-150 km, the presence of a basal mantle layer is rendered feasible, although not strictly required to meet the moment of inertia constraints. James et al. (2014) used the basal layer hypothesis to investigate to what extent domical swells observed in topographic data of Mercury can be explained by irregularities in the thickness of the dense basal layer. The analysis used a minimum basal layer thickness of 10-15 km.

4.1.1. Fitting algorithm

Based on this previously conducted literature research, the residual gravity field that results from several thickness and density combinations of the basal layer is computed. This initial search space analysis is then used as input for a more detailed fitting algorithm, that determines either the density variations in a constant-thickness layer or the thickness variations of the constant-density layer. The fitting is performed such that the Hermeoid matches with the observed data. The three crustal models established in Chapter 2 - *AiryFitted, BLFitted and JamesCorrelation* - are used as input, and are extended to include the mantle and basal layer.

The initial density and thicknesses of the basal layer are taken from literature. The edge of the outer core is simulated to be located between 400-440 km (referenced from the surface) (Margot et al., 2018; Smith et al., 2012). To allow for maximum thickness of the basal layer, in this simulation the CMB is modelled at 440 km. The crustal thickness was calculated to vary between 0-100 km (see Chapter 2), leaving a possible thickness

of the basal layer of 0-340 km. The included density variation is not limited to any magnitude. Reasonable values are expected to lie between the mantle density, 3100 kg/m^3 (Airy & Bouguer) and 3400 kg/m^3 (James), and an upper margin of 5400 kg/m^3 (Hauck et al., 2013). It is obvious that thinner basal layers require larger density contrasts. It is also clear that these larger contrasts are less likely to exists in the thinner layers. Therefore a careful balance is to be found between the two parameters.

As the CMB-location could potentially also be located at 400 km depth, and other analyses often also use this location of 400 km, this scenario is also investigated. The results for the basal layer fitting process are included in Appendix A.1. The maximum thickness of the CMB-layer is reduced accordingly, as the mantle thickness is decreased and the CMB-layer can not interfere with the crust.

The threshold that is used to determine whether the Hermeoid is sufficiently fitted, is 10 m. When a numerical model is constructed that produces a gravity field that at any location shows a discrepancy no larger than 10 m, the simulation is considered to be converged. This 10 m is based on the accuracy of the modelled gravity field and on that of the observation data. Mazarico et al. (2014) calculated the spherical harmonic coefficients of the gravity field from the MESSENGER data and verified that the error of this field lies within 0 and 10 mGal (see Figure 8a from (Mazarico et al., 2014)). The numerical model is proven to be accurate within ±4 mGal, resulting in a total spread of 8 mGal (Root et al., 2016). Given these values, the threshold for convergence of the gravity field is set to 10 mGal. Given the range of the free-air anomaly is as large as the Hermeoid, the threshold for the Hermeoid is taken to be 10 m. The fitting algorithm is visualised in Figure 4.1.

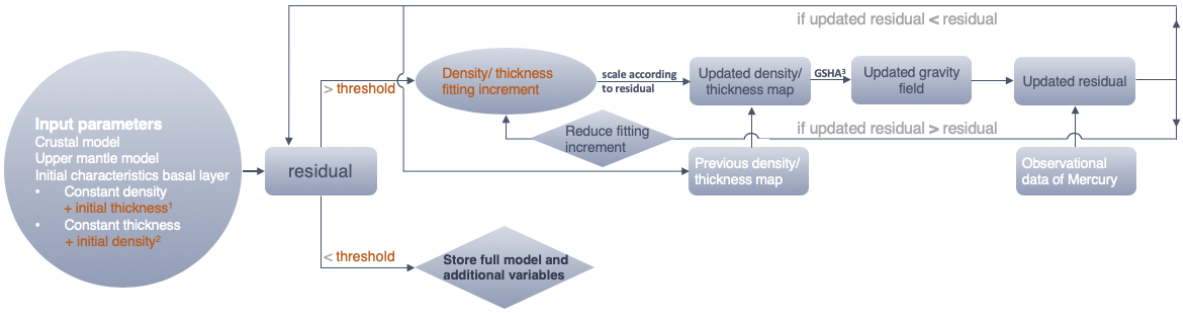

Figure 4.1: Graphical representation of the fitting algorithm. Orange text indicated variable input parameters (please also see Section 5.8). [1] Is only a variable input parameter when the layer *thickness* is fitted. [2] Is only a variable input parameter when the layer *density* is fitted. [3] GSHA = Global Spherical Harmonic Analysis (software package obtained from Root et al. (2016)).

4.1.2. Parameter range selection

The deep mass anomalies in Earth that are used as a means of comparison, are on average 300 km in height, have bulges of maximum 1000 km in height (measured upward from CMB) and cover 30% of the CMB (Garnero et al., 2016). For translation of these characteristics of the LLSVPs in the Earth to deep mass anomalies in Mercury, we use the information that the mantle thickness of Mercury is only 15% of that of Earth, the full radius of Mercury is 0.4 times the radius of the Earth, and Mercury's core size is 0.57 that of Earth. As it is yet unknown what determines the size of the LLSVPs and if and how their size relates to the size of the different layers, all radii are taken into consideration. This would translate to a basal layer in Mercury with a thickness between 45 and 580 km. As the crust of Mercury is taken to be ~80 km, the upper bound of LLSVPs in Mercury are set to 360 km (or 320 km in case of a CMB at 400 km) to prevent interference with the crust. The density increase in Earth - or decrease, scientists have not yet drawn an unequivocal decision on this - is estimated to be around 2-5%, given the sharp edges that otherwise would not sustain (Trønnes, 2010). For Mercury this would convert to a density anomaly of 60 - 150 kg/m^3, given that the mantle density is estimated to be around 3100 kg/m^3 and taking into account the undetermined height of the LLSVPs. Further review of these ranges have led to the parameter ranges as indicated in Figures 4.2 and 4.3, considering the accuracy of the available data and hypothetical detectability of density anomalies. The outer bounds of the fitted density and thickness values are summarised in Table 4.1.

The same analysis has been performed for Mercury model where the CMB is located at 400 km. This is done as the CMB is constrained to be located at 400 - 440 km depth. For the temperature anomaly analysis discussed later in this chapter, a CMB located at 400 km was used, hence this duplicate analysis. The results are given in Figures A.1 and A.2 and Table A.1. Given the very similar results, these are not discussed separately.

4.1.3. Density fitting results

In Table 4.1 and Figure 4.2 it is observed for all three crustal models that the constant thickness layer of 10 km did not reach the convergence criterion of 10m. This is understandable as the lower bound of the thickness was established to be 45 km in Mercury when comparing with Earth. A basal layer of 50 km already approaches more realistic density variations in the range of 190-525 kg/m^3. At this lower bound of previously established realistic thicknesses, the calculated required density contrast is still too large. For the Airy and Bouguer model the thicknesses 100 and 150 km give a density contrast that is similar to the 2-5% density increase that is observed in Earth. Thicker basal layers of 200 and 300 km yield density contrasts that are considerably less likely to sustain over long periods of time. James' model requires a slightly thicker layer that basically covers the entire mantle, implying not real LLSVPs at the base of the mantle but a more global density contrast throughout the mantle.

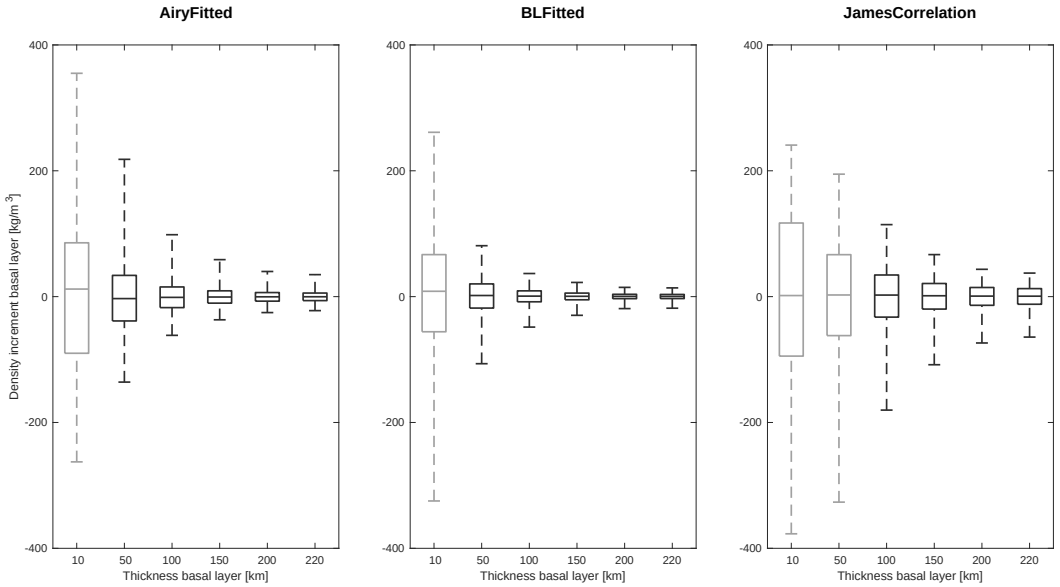

Figure 4.2: Results of the density fitting process. In all models a constant-thickness layer is included on top of the CMB (located at 440 km), that is allowed to vary in density laterally. The boxplots indicate the spread in the fitted densities, such that the interior models reproduce the residual gravity field (residual after subtraction of crustal gravity field - see also Chapter 2) and assuming a constant mantle density. Light grey boxplots indicate no convergence (within the preset number of iterations). Remaining residuals: Airy-10: ±80m, James-10:±200m, Bouguer-10:±30m, James-50:±30m.

In Chapter 2 it is observed that the James crustal model requires larger deep mass anomalies - so either large thickness or density variations. This is expected from the relatively large residual that is to be counteracted. The James crustal model did not converge initially, which is expected to be caused by the short-wavelength anomalies that still remain in the residual of the James' model but can hardly be fit by deep mass anomalies. Therefore only the gravity field up until spherical harmonic degree 10 is included (instead of spherical harmonic degree 50). Given that deep mass anomalies are investigated, this is considered a valid assumption.

4.1.4. Thickness fitting results

In case of thickness variations of an equal-density layer, the initial thickness is important. An initial guess is based on the density fitting analysis. A reduction in the thickness range of 20% is observed for the Airy case, when the initial thickness of the basal layer is increased from 50 to 100 km (see Figure 5.15). The layer with an initial thickness of 100 km thus results in a flatter layer with less frequent and extensive bulges. To exclude the influence of the initial thickness, an initial thickness of 100 km is set for all constant-density profiles.

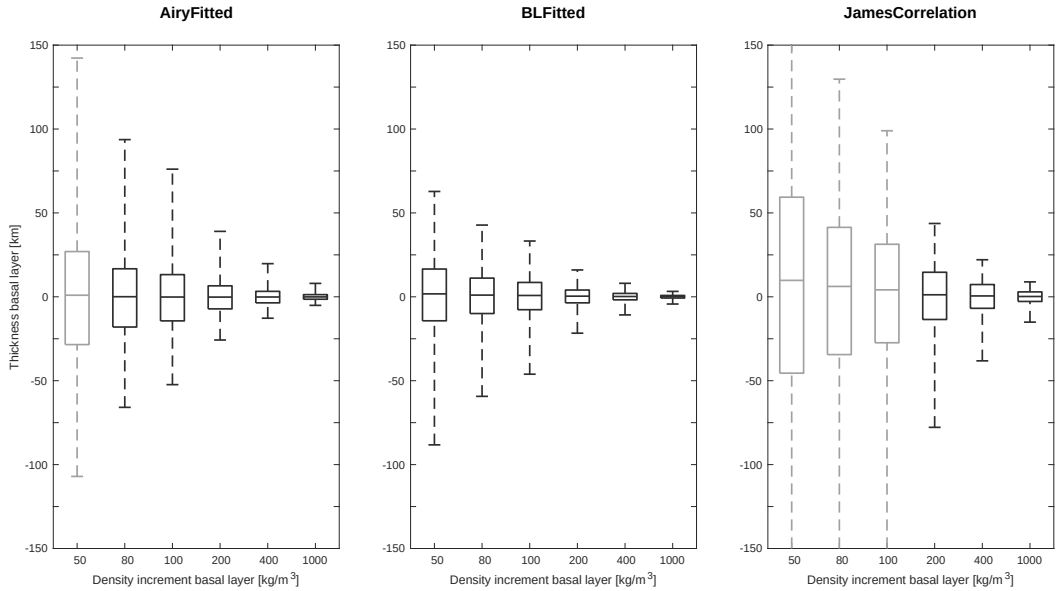

Figure 4.3: Results of the thickness fitting process. In all models a constant-density layer is included on top of the CMB (located at 440 km), that is allowed to vary in thickness laterally. The boxplots indicate the spread in the fitted thickness, i.e. the mean thickness has been subtracted, such that the interior models reproduce the residual gravity field (residual after subtraction of crustal gravity field - see also Chapter 2) and assuming a constant mantle density. Light grey boxplots indicate no convergence (within the preset number of iterations). The reason for non-convergence in all cases is a too thick layer, i.e. a layer that penetrates into the core. Initial thickness parameter is 100. Average thickness parameters: Airy [87,92,94,97,98,99], Bouguer [104,103,102,101,101,100] and James [124,116,112,106,103,101].

density fitting [kg/m^3]	Airy		Bouguer		James	
	min	max	min	max	min	max
t = 10 km	-263	355	-325	261	-377	241
50	-136	218	-107	81	-327	195
100	-62	98	-48	37	-180	114
150	-37	59	-30	23	-108	67
200	-25	40	-19	15	-74	43
300	-22	35	-18	14	-64	37

thickness fitting [km]	Airy		Bouguer		James	
	min	max	min	max	min	max
ρ = 50 kg/m^3	-107	142	-88	63	-406	151
80	-66	94	-59	43	-305	130
100	-52	76	-46	33	-196	99
200	-26	39	-22	16	-78	44
400	-13	20	-11	8	-38	22
1000	-5	8	-4	3	-15	9

Table 4.1: Minimum and maximum values of the density (top) and thickness (bottom) of the basal layer after the fitting process, in addition to the boxplots in Figures 4.2 and 4.3 Light grey entries indicate non-convergence.

.

From Table 4.1 and Figure 4.3 it is concluded that for neither of the Airy and James models convergence is reached for the 50 kg/m^3 density increment, because of unrealistic layer thickness that require to reach deeper than the CMB. For James the minimum density difference that allows for convergence is 200 kg/m^3. For both the Airy and Bouguer model convergence is achieved for the lower density increments of (50,) 80 and 100 kg/m^3. The basal layer with a 80 kg/m^3 density increment requires a thickness range of 160 km and 102 km respectively, for the 100 kg/m^3 density increments this is 128 versus 79 km. All values are within the previously established realistic thickness range. The larger density increments result in a flatter and thinner basal layer, however the combination of these thickness parameters and the density difference render it unlikely that these basal layers will sustain over a long period of time. All results show a concentrated thickness close to the mean thickness, with outliers that deviate relatively far from the mean. This is indicative for spiky bulges.

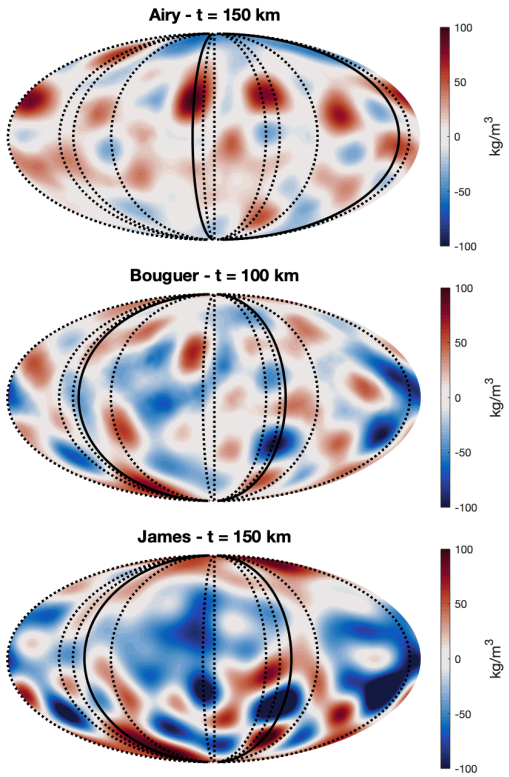

Figure 4.4: Outlook of the density variation in the basal layer of the best-fit models. The black lines indicate the cross-sectional cutting location of the images in Figure 4.6. The dotted lines are standard locations, the continuous line is the longitudinal location of highest variation. Images are in Mollweide projection and have a central meridian of 180^{o}E.

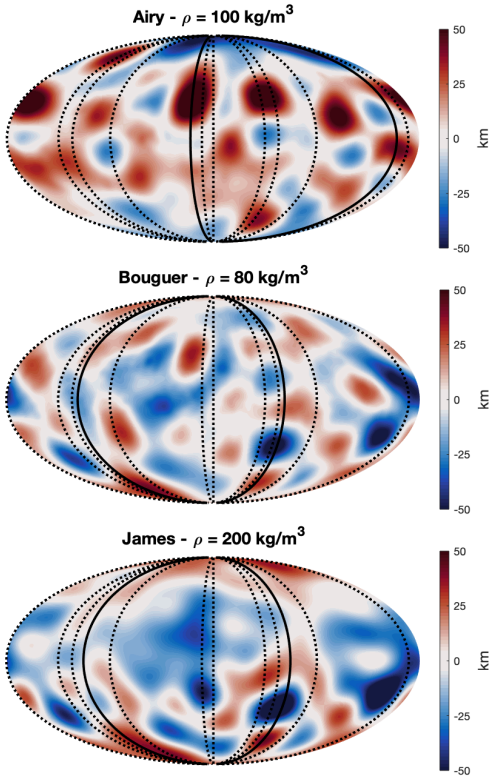

Figure 4.5: Outlook of the thickness variation in the basal layer of the best-fit models. The black lines indicate the cross-sectional cutting location of the images in Figure 4.6. The dotted lines are standard locations, the continuous line is the longitudinal location of highest variation. Images are in Mollweide projection and have a central meridian of 180^{o}E.

4.1.5. Cross-sectional analysis

For all six analyses (Airy - density, Airy - thickness, Bouguer - density etc.) the best basal layer characteristics are selected, displayed in Figures 4.4 and 4.5. The selection of these best characteristics is based on the comparison of the characteristics of the basal layers with the same characteristics of the LLSVPs in Earth, and which one shows the highest level of resemblance in terms of these density and thickness values. As the models corresponding to one of the crustal models are all based on the same Hermeoid input, the shapes of the basal layers throughout the models are similar and this is not used as a selection criterion. The selected models are Airy: 150 km and 100 kg/m^3, Bouguer: 100 km and 80 kg/m^3 and James: 150 km and 200 kg/m^3. Of these interior models, the outlook of the fitted basal layers is plotted in Figures 4.4 and 4.5. Cross-sectional

plots are made in Figures 4.6 and 4.7 as a means of verification, and to visualise the shape of the basal layers further. Please note that to enhance the visualisation, the core radius in the plots is decreased and the plots are thus not to scale. For all models several cross-sectional locations of interest are investigated: (1) 0^oE - the centre of the two basal layers, (2) 45^oE, (3) 57^oE - Rachmaninoff basin, location of thinnest crust, (4) 90^oE - in between the two basal layers, (5) 170^oE - the Caloris basin and (6) variable longitude, depending on largest thickness/density range in the basal layers. In Appendix A all plots are included and in this chapter the shape of the basal layers at 90^oE (and obviously 90^oW) is given, and the longitudinal cross section that shows the largest variation in either density or thickness.

All these plots show that the basal layers, although they were fitted to the Hermeoid fields, have high level of resemblance with the corresponding gravity field. Because deep mass anomalies are known to be best visible in the geoid/Hermeoid, the basal layers were expected to show resemblance with the Hermeoid. The implication of this notion on the to be drawn conclusions, and the consequential recommendations can be found in Chapter 6.

The Airy plots show that the pattern in the fitted basal layer resembles the observed free-air anomaly to a large extent. See for example the location of Caloris basin in the top right figure of Figure 4.6, indicated by highly saturated red colour. As can be seen in Figure B.2 by the level of detail of the crustal map, the Airy crustal model mainly counteracts the gravity field in the short-wavelength domain. Therefore the remaining field contains the larger oscillations and thus looks much like the observed gravity field. The latter field is used as input for the fitting process and hence the resemblance between the density profile of the basal layer and the residual gravity field. It should be noted though that the gravity field and the density profile of the basal layer are not 1-on-1. Although strong features are clearly distinguishable in both fields, smaller features are not as easily traced back, which indicates that the gravity field at one specific location is not only affected by the mass radially downwards, but also affected by its surroundings. The Airy thickness plots in Figure 4.7 are generated using the same input data. These plots visualise the shape of potential LLSVPs in Mercury. Please keep in mind that the figures are *not* to scale, and therefore the bulges in the basal layer are exaggerated. Interesting however is the location of these bulges. While in Earth the bulges are identified to be centred on the equator and slightly north, the bulges in Mercury are pointing towards the northern hemisphere. This could be the consequence of the poor data quality for the southern hemisphere of Mercury.

After subtraction of the Bouguer crustal model from the observed gravity field, a gravity field remains that shows a broad band of mass around the equator, but not necessarily bulky. The fitted basal layers show more indications of this bulky behaviour and therefore show more correspondence with Earth LLSVPs. This model seems to be a hybrid of the Airy & James model, which was also already concluded from the gravity models. The Bouguer model has the lowest residual and therefore requires the smallest density and thickness increments, and it can be questioned whether this model can really be compared to LLSVPs, or that the observed irregularities are just regular variations within a mantle.

The James crustal model requires a thicker basal layer than the other crustal models to remain within realistic density bounds. The required density or thickness variations in the James basal layer are much more gradual than in the Airy or Bouguer models. In the figures with fitted thicknesses in Figure 4.7 it becomes most clear how the James model is more gradual: the basal layer is fitting large anomalies. Especially in the bottom left plot the basal layer in Mercury shows two bulges on the equator - both slightly oriented towards the south. As the crustal model of James is not defined for latitudes smaller than -30^o, these results are disputable. The same holds for the middle right plot, that shows a deep cave at poor-constrained location.

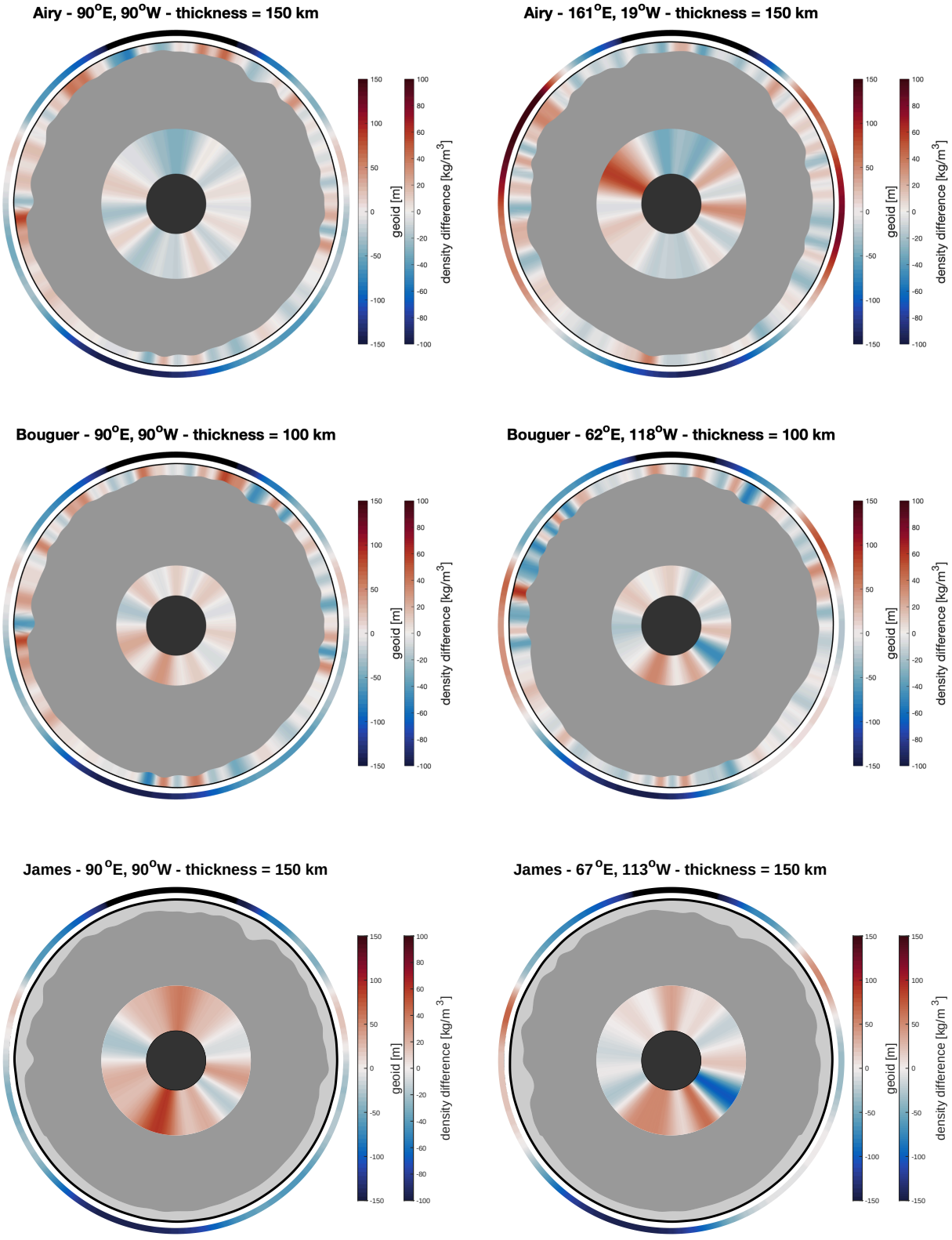

Figure 4.6: Cross sections of inner Mercury after fitting the density of the basal layer to the observed gravity field, at different longitudinal locations for three different models. The outer ring indicates the magnitude of the observed geoid. From the black line outside to inside: crust, mantle, basal layer, core. The size of the core has been reduced to enhance the legibility of the figure, and therefore the figure is *not* to scale.

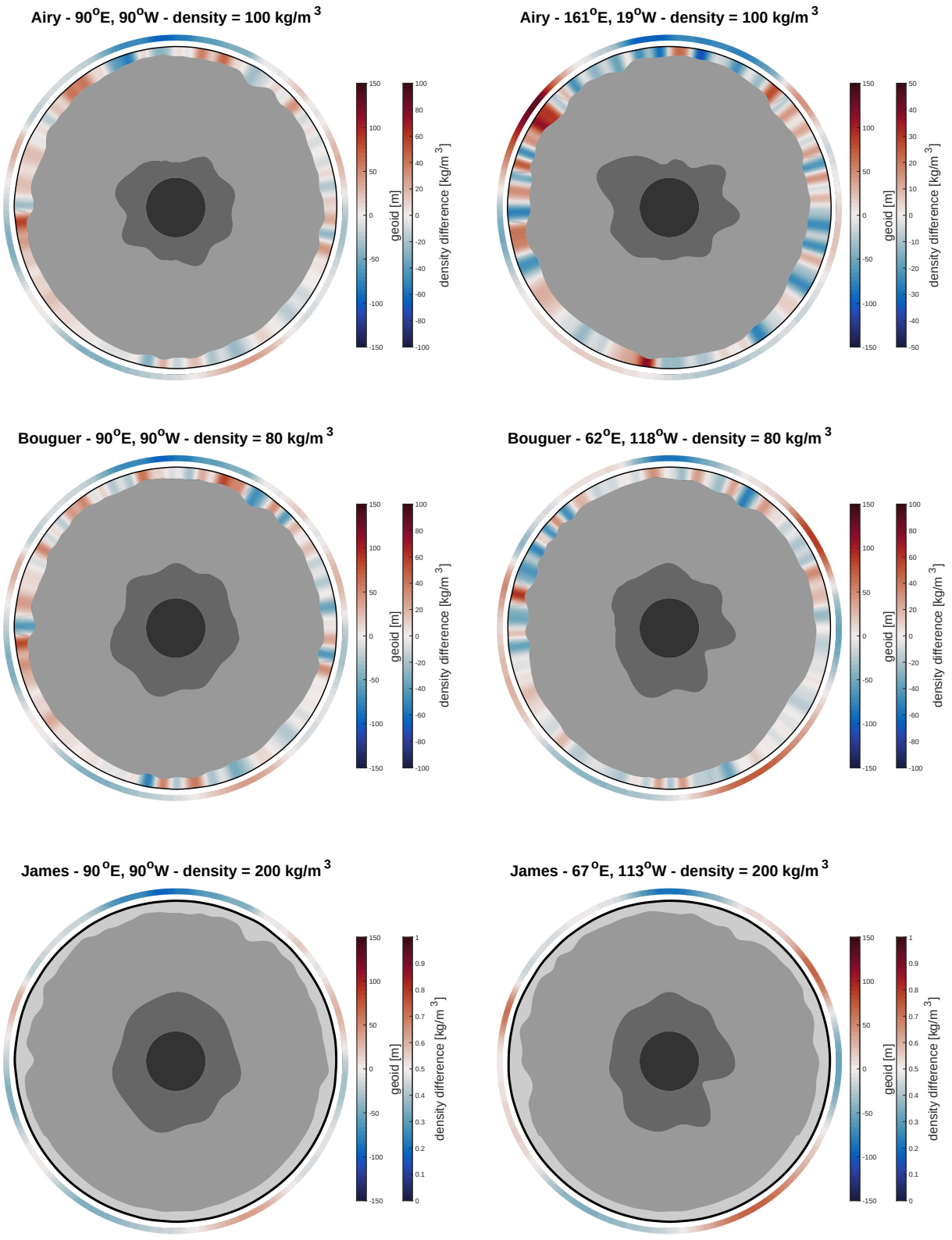

Figure 4.7: Cross sections of inner Mercury after fitting the thickness of the basal layer to the observed gravity field, at different longitudinal locations for three different models. The outer ring indicates the magnitude of the observed geoid. From the black line outside to inside: crust, mantle, basal layer, core. The size of the core has been reduced to enhance the legibility of the figure, and therefore the figure is *not* to scale.

4.2. Core-mantle boundary variations

In the previous analyses it is assumed that the core is perfectly spherical and of homogeneous density, hence causing no gravity anomalies. CMB topography is however not uncommon, and therefore in this section it is assessed what the CMB variation should be to counteract the observed gravity anomaly.

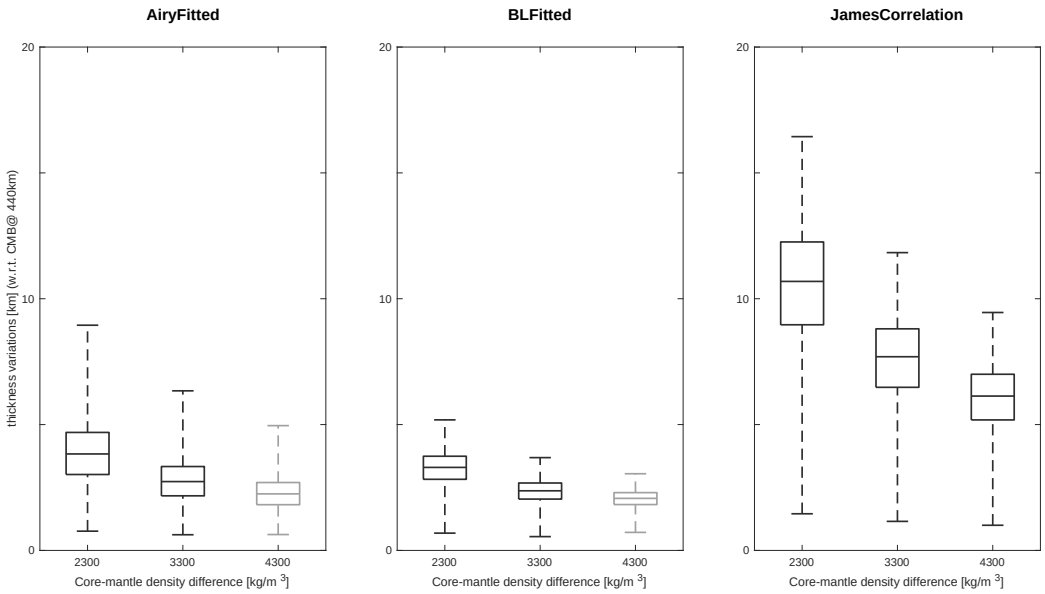

Figure 4.8: Results of the CMB topography fitting process. In all models the depth of the CMB is allowed to vary laterally. The boxplots indicate the spread in the fitted thickness, i.e. the mean thickness has been subtracted, such that the interior models reproduce the residual gravity field (residual after subtraction of crustal gravity field - see also Chapter 2) and assuming a constant mantle density. Light grey boxplots indicate no convergence (within the preset number of iterations). The reason for non-convergence is a remaining residual of ±15m, which is outside the convergence range of 10m remaining Hermeoid. Initial thickness parameter is set to 0.

In Figure 4.8 the results are visualised. Immediately evident is the trend that was observed earlier as well: Bouguer requires the smallest variations, Airy slightly more and James has a significantly larger range. The CMB variations are in the range of 1-17 km, depending on the core-mantle density contrast and the selected crustal model. The initial thickness of the layer is set to 0 km. In each iteration the algorithm scales the added thickness of the core to the residual. As the location of minimum residual changes per iteration because of the fitting process that the model undergoes, eventually there is no location where 0 thickness is achieved. The core is thus extended as a whole, but this is in all models merely 1-2 km.

CMB variations are also observed in Earth, and are found to be at maximum 12.4 km (Soldati et al., 2013). Given that the core radius of Mercury is approximately 0.6 × the core radius of the, only the CMB variations corresponding to a large core-mantle density contrast are viable, and then especially the Airy and Bouguer model. The core mantle boundary contrasts currently modelled are 2300, 3300 and 4300 kg/m^3. These contrasts are based on values in literature (Tosi et al., 2015; James et al., 2014), however these are in comparison with Earth rather small. The core-mantle density contrast in Earth is ~5000 kg/m^3 (Volgyesi and Moser, 1982). Given the higher pressure and temperature at which this transition takes place in Earth, it is not likely that the CMB in Mercury also depicts this steep gradient.

4.3. Temperature anomaly

It is suggested by Tosi et al. (2015) that the surface of Mercury is unevenly exposed to solar insolation and that this induces temperature variations across its surface. This is the result of the 3:2 spin orbit resonance that Mercury is captured in, its high orbital eccentricity and the low obliquity (Tosi et al., 2015). Would this specific resonance pattern have sustained over a long time, than there is possibility that the uneven temperature distribution has propagated to the deeper layers, as deep as the CMB. The temperature pattern would show hot poles of ~430 K at 0^o and 180^o longitude, where the surface is always illuminated by the Sun. Warm poles

of ~345 K are located at 90^o and 270^o longitude, where the insulation is still strong, albeit not permanently. At both the north and south pole cool poles of ~260 K would be located. This uneven temperature distribution would induce a density anomaly in the mantle that possibly can account for the long-wavelength Hermeoid undulations observed in Mercury. Tosi et al. (2015) noted that a locations of hotter material, there would be a negative density anomaly, leading to negative Hermeoid undulations, which is in contrast with the observations. Therefore, they argue that the alleviation on the CMB that is associated with this reduction in density could allow for an uplift of the CMB, which in turn would counteract the Hermeoid reduction and even flip the sign of the Hermeoid. Tosi et al. (2015) investigated this by quantifying the variation in elastic thickness that would result from the temperature anomaly. They calculated that the result would only be a few tens of meters of uplift of the CMB, using a density contrast of 3600 kg/m^3 and assessing only the Hermeoid in spherical harmonic degrees 2 & 4. In this chapter the temperature profiles from Tosi et al. (2015) are used (conduction & convection profile) to construct the accompanying density model and use that together with the crustal models as input for the calculation of required CMB variations.

4.3.1. Mantle models

There is little knowledge of the mantle composition of Mercury. It is known that the planet has a large metallic core and that the surface is depleted of FeO. Also in volcanic regions, where the mantle material is expected to be solidified on the surface, the abundance of FeO is low (Margot et al., 2018).

Taylor and Scott (2005) made a summary of the most plausible bulk mantle compositions for Mercury in wt.%, see Table 4.2. Rivoldini et al. (2009) converted these mantle minerals to a depth-dependent volume fraction overview. These models are used as input for the density profiles of Mercury, or more specifically, for the difference in density between the high-T and low-T locations. A short summary of these models:

- FC - evaporation model (Fegley and Cameron, 1987). This model assumes that protoplanet Mercury formed under very high temperatures, leading to the evaporation of silicate and increasing the metal/silicate ratio, complying to our current day observations. The models have a high abundance of MgO. Taylor and Scott (2005) selected of the models the one with an FeO-content closest to the observations. However, more recent studies have already indicated that the temperature ranges considered in this study are unlikely at the location of Mercury. Furthermore, the surface composition measurements done by MESSENGER indicate a high abundance of volatiles such as SiO_2, which is in conflict with this model (Nittler et al., 2018).

- GT - refractory condensation (Goettel, 1988; Taylor and Scott, 2005): this model assumes that Mercury contains high-temperature condensates: metallic iron and FeO-free silicates. The abundance of other volatiles such as Al, Ca, Mg, Na and K is high. This model could explain the large metallic core, however it does require that Mercury accreted rapidly, maybe more rapid than is reasonable. Taylor and Scott (2005) considered this model as an interesting end-member case, but pointed out that this is not a likely mantle composition for Mercury, as was also already concluded by others.

- MA - refractory volatile mixtures (Morgan and Anders, 1980; Rivoldini et al., 2009): this model assumes that Mercury experienced a fractionation process during the solar nebula. The core mass, FeO content and moon-like abundances of other materials result in this model.

- TS - combination GT & MA: (Taylor and Scott, 2005; Morgan and Anders, 1980; Goettel, 1988): this model is a combination of the model by Goettel (1988) and the model developed by Morgan and Anders (1980). Taylor and Scott (2005) assign Mercury a higher percentage of refractory materials (heat-resistant materials) to take into the account the immense heat at the location where Mercury formed. The composition of the primitive mantle of the Earth is taken as the other end-member. The two end-member are mixed such that the final mantle model contains 3 wt% FeO.

- MC - metal-rich (Krot et al., 2001; Taylor and Scott, 2005): this model is based on the suggestion that the composition of metal-rich chondrites could be indicative of the composition of Mercury. The composition of two metal-rich chondrites is averaged out, resulting in a mantle composition slightly lower in FeO than generally assumed, slightly lower in refractory elements and also in volatiles. This mantle model is similar to the MA model, however it has the advantage that it is based on the analysis of the composition of actual objects.

	FC	GT	MA	TS	MC
SiO_2	19.9	32.6	47.1	37.6	50.8
TiO_2	0.6	0.7	0.3	0.5	0.2
AL_2O_3	14.4	16.6	6.4	11.7	5.2
Cr_2O_3	0	0	3.3	0.2	0.7
FeO	3.4	0	3.7	3.0	2.0
MnO	0	0	0.06	0.05	0.1
MgO	50.0	34.6	33.7	36.1	37.4
CaO	11.7	15.2	5.2	10.7	3.6
Na_2O	0	0	0.08	0.1	0.04
K_2O	0	0	0.01	0.01	0.04
Th (ng g^{-1})	380	293	122	207	93
U (ng g^{-1})	0.2	81	34	58	26

Table 4.2: Overview of the different models of the bulk chemical composition of Mercury's mantle. The grey entries are not included in the model, because of a lack of data about the thermal properties of this component in the specific solution models. Modified from (Taylor and Scott, 2005).

The temperature profile for Mercury's mantle is taken from Tosi et al. (2015), who computed a convective and conductive model to assess how variations in insolation at the surface would propagate into the deep mantle. The pressure profile $P(r)$ is calculated using Equation 4.1, where GM is the gravitational constant × the mass of the planet, in this case 2.2032· 10^{13} m^3s^{-2}, and R the radius of the planet, in this case 2439.35 km (Lissauer and de Pater, 2013; Margot et al., 2018). The derivation of Equation 4.1 is included in Section 5.11.

$$P(r) = \frac{3GM^2}{8\pi R^4} - \frac{3GM^2 \cdot r^2}{8\pi R^6} \tag{4.1}$$

The temperature and pressure profile of Mercury are required to compute the density of Mercury's mantle at various location, to determine the lateral density difference.

Perple_X

The software package Perple_X calculates and displays phase diagrams, phase equilibria and thermodynamic data. For a given composition and with information on the mineral elastic properties, Perple_*X* solves the equations-of-state to compute the elastic mineral properties at each point in a predefined pressure-temperature range. This allows for the analysis of various material characteristics, including density and several seismic properties. The software is developed and maintained by Jack A.D. Connolly from the Eidgenössische Technische Hochschule (ETH) Zürich (Connolly, 1990). It is open source available as software package[1] and offers, in combination with the elaborate documentation, endless possibilities, also for inexperienced users.

A flow-chart diagram of the working procedure of Perple_X is included in Figure A.3. One starts with stating the problem definition in the BUILD file. This file requires information on the computational and physical settings of the problem in the *option_file*. The BUILD file requires the selection of a *thermodynamic dataset*. The default thermodynamic dataset from Holland and Powell (2004), expanded to comply with the Perple_X input requirements and constructed from experimental data, is used for this research. This data file is suited for generic analyses, rather than for extreme cases, and contains the information about the main mantle components. The selected *solution model* describes the mixing properties of the included minerals. Again, the default solution model is used as these data points are representative for the analysis case. In the BUILD file one can also include or exclude specific (new) minerals, alter other characteristics concerning saturation and define the pressure-temperature range. Once the BUILD file has been generated, this information can be inserted into VERTEX and WERAMI programs. The VERTEX program performs the actual calculations and the WERAMI software converts this information to a usable output of a desired number of data points. The other software tools indicated in Figure A.3 are not used.

Perple_X is used to calculate the mantle density and compute the density difference between the hot and cold mantle regions of Mercury. In this analysis the density difference along an isobar is calculated and therefore

[1] `http://www.perplex.ethz.ch`

the effect of pressure need not to be investigated. The results of this computation are displayed in Figures 4.9 to 4.12, along with the results of the fitting process. The coloured lines indicate the density contrast that would exist between the hot and cold mantle region. The grey bars are the results of the fitting process, and show either the required density variation in a layer of constant depth or the required thickness variation in a layer of constant density. The boxplots indicate the spread in the modelled density or thickness variation, to give an impression of what the average parameter is, and it spread. It is clear that the fitting process requires positive density anomalies at the location of positive gravity anomalies, while the temperature anomalies cause negative density anomalies at this specific location. In Section 4.2 the interaction between the mantle and the core is further investigated, aiming to explain this seemingly conflicting observation.

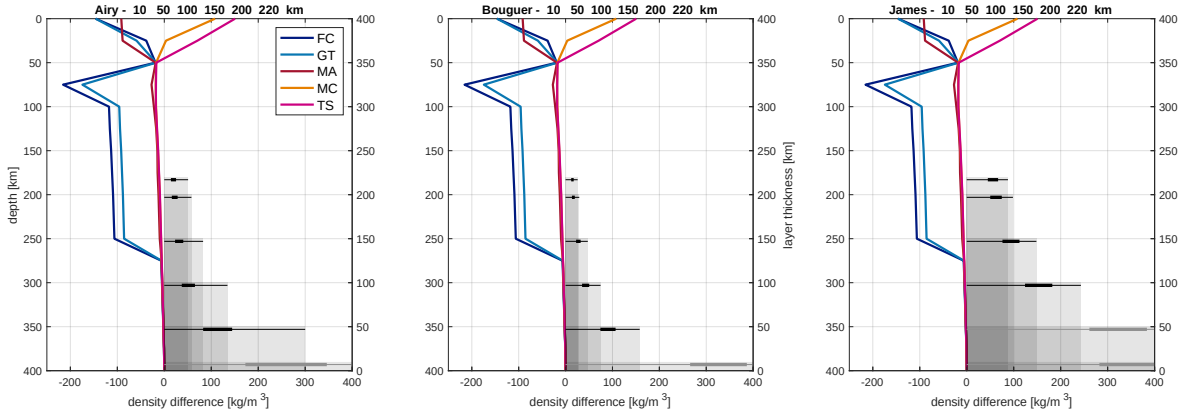

Figure 4.9: The results of the fitting process plotted along with the density contrasts that would arise between hot and cold poles in a *conductive* mantle. The boxplots atop the grey bars indicate the spread in fitted density differences, to give a rough indication of the average required density difference.

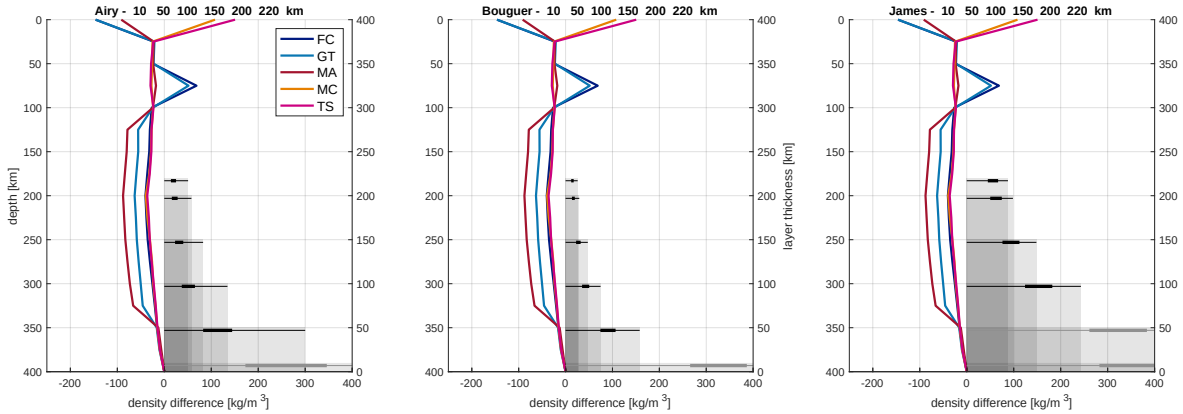

Figure 4.10: The results of the fitting process plotted along with the density contrasts that would arise between hot and cold poles in a *convective* mantle. The boxplots atop the grey bars indicate the spread in fitted density differences, to give a rough indication of the average required density difference.

The convection and conduction results are plotted separately to enhance the legibility of the graphs. The density difference is calculated as the density in the warm regions minus the density in the cool regions, hence negative differences indicate a mass excess in cool regions. In the regions where the LLSVPs are modelled, up to ~300 km, only negative density differences are observed. The FC and GT models show a strong peak in density, potentially pointing towards a phase transition, however this transition occurs outside of our region of interest. The MA, MC and TS models show much more gently density differences. Although these differences are not as significant as the density differences that could be associated with a phase transition, occurrence of this small discrepancy throughout the whole mantle could still induce a significant gravity anomaly.

It also becomes clear that the largest density differences occur halfway in the mantle, which relates to the temperature differences being maximum there. The temperature anomaly is not adjacent to the CMB, and therefore it is likely that density differences associated with this temperature anomaly occur midway the mantle, rather than near the CMB region.

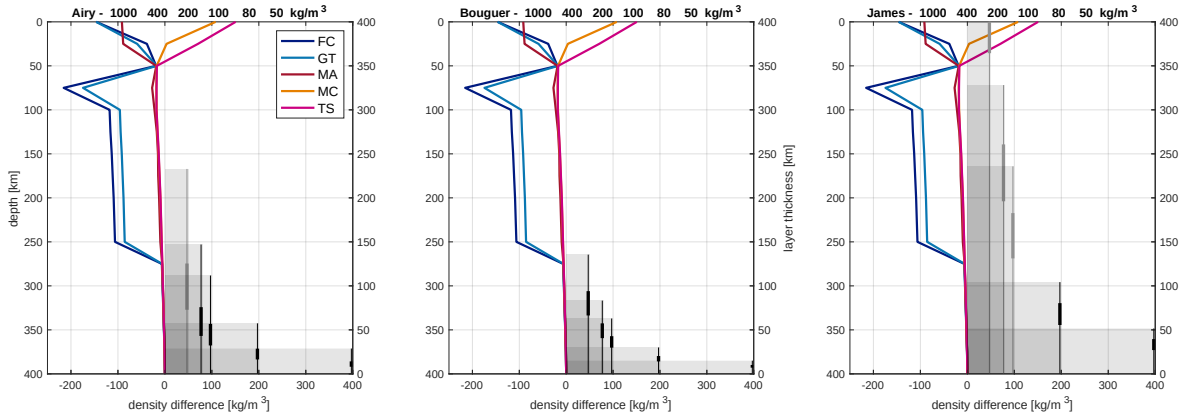

Figure 4.11: The results of the fitting process plotted along with the density contrasts that would arise between hot and cold poles in a *conductive* mantle. The boxplots atop the grey bars indicate the spread in fitted thickness of the basal layer, to give a rough indication of the average required thickness.

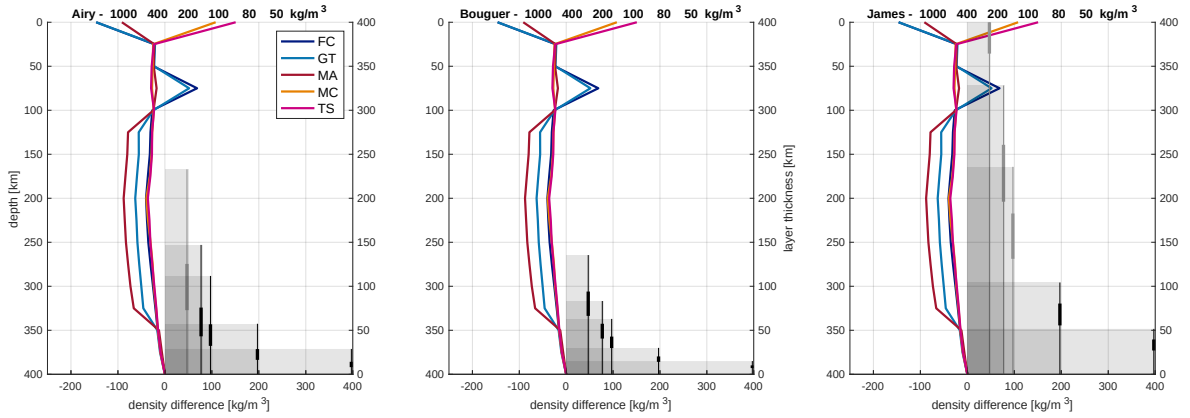

Figure 4.12: The results of the fitting process plotted along with the density contrasts that would arise between hot and cold poles in a *convective* mantle. The boxplots atop the grey bars indicate the spread in fitted thickness of the basal layer, to give a rough indication of the average required thickness.

4.3.2. Thermal expansion of differentiated interior models

An often suggested explanation for the low FeO content in the mantle and surface composition of Mercury is the existence of a distinct chemical layer wrapped around the CMB. This iron-sulfur/iron-silicate/iron-sulfur-silicate-layer (FeS-/FeSi-/FeS-Si) would explain the observation of a very dense metallic core, while also observing a low FeO content in the mantle.

The possible existence of this layer in Mercury could also function as the dense basal layer of varying thickness that was modelled in Section 4.1. Thickness variations in this layer, for example initiated by a certain mantle convection pattern or because of tidal forces, could account for the gravity anomaly. In this case we are talking about major density differences, but densities that are still smaller than the core density. Hauck et al. (2013) constrained the upper bound of this basal layer density to 5400 kg/m^3, implying a density difference between the mantle and the layer of at maximum 2300 kg/m^3. James et al. (2014) used as density difference between the mantle and the basal layer a value of 1000 kg/m^3. They set the thickness of the layer

to an arbitrary value of 100 km, arguing that it would fit within the interior structural models of (Smith et al., 2012; Hauck et al., 2013). James et al. (2014) used this model to calculate how thickness variations in the basal layer would induce topography, however in this study these data points are used in a different way. A 100 km thick basal layer in a 400 km thick mantle with a density difference of 1000 kg/m^3 is modelled for the James crustal model in Figure A.2. The required thickness variation to counteract the gravity field is calculated to be 21 km (-13 to +8). This is in line with the findings in (James et al., 2014), who concluded that thickness variations of 10-15 km would induce a few kilometres of topography.

Another possibility in this FeS-/FeSi-/FeS-Si-layer are density differences as a result of the temperature anomaly. Equation 4.2 gives the density of an FeSi alloy with a certain percentage χ of Si. Equation 4.3 gives the equation that corrects for temperature differences in the mantle. The density of the FeSi alloy is indicated by $\rho_{0,Fe-Si}$, $\rho_{0,a}$, $\rho_{0,b}$, $\rho_{0,c}$ are constant values based on experimental data, given in Table 4.4. The weight percentage of silicate is indicated by χ. In Equation 4.3 the equation is given that is used to correct for thermal expansion. The parameter α is the thermal expansion coefficient and needs to be determined experimentally. In this study the density is only corrected for varying temperatures, and the effect of varying pressure is not included. Therefore, the absolute densities at a certain location in Mercury are not representative, however the density difference along an isobar is. As only density *differences* along these isobars are required in the calculation of gravity *anomalies*, the results are still valid.

$$\rho_{0,Fe-Si} = \rho_{0,a} \cdot \chi_{Si}^2 + \rho_{0,b} \cdot \chi_{Si} + \rho_{0,c} \tag{4.2}$$

$$\rho = \rho_0 \cdot \left(\frac{1}{1 + (T - T_{\text{ref}}) \cdot \alpha} \right) \tag{4.3}$$

Figure 4.13 (and also Figure 4.14) shows that the convective solution would imply larger density differences than the conductive solution. Also the pattern of the two is distinctive; the conductive model shows a gradual reduction in density difference, while the convective model clearly displays a maximum. This is the result of the temperature profiles. The top 75 km of the planet is likely to be crust and therefore not consisting of FeS. Furthermore, a *basal* layer comprising FeS is often suggested in literature, which would only generate interest for the density differences in the lower region of the mantle. In the regions near the CMB the temperature difference is relatively small, hence the density difference is also small. Although the differences are minor, they are not negligible, especially not in the case of a convective model. The difference between either the liquid or solid phase of FeS is not of high influence, the resulting density differences are nearly the same, especially in the lower mantle region.

For the FeSi results in Figure 4.14 the expected density differences following from the data of (Dumay and Cramb, 1995) (indicated with a continuous line) and the data of (Lin et al., 2003) (indicated with an X and a dashed line) are computed and show to be of larger magnitude than the FeS differences. The density differences of Dumay and Cramb (1995) show that the addition of Si reduces the density difference, and that this reduction in the density difference flattens out as one adds more Si: Fe-17wt%Si and Fe-20wt%Si depict almost similar density contrasts. The results for Fe-17wt%SiX show a much smaller density difference than is predicted by Dumay and Cramb (1995). It is difficult to select one of the Fe-17wt%Si and Fe-17wt%SiX as more reliable, as both experiments require some remarks. The Dumay and Cramb (1995) density values are the result of an empirical relation constructed from measurements at various weight percentages of Si, and not necessarily 17wt%. Lin et al. (2003) performed measurements specifically for Fe-17wt%Si, however did this at a much lower temperature - and thus for a basal layer a less representative temperature - than Dumay and Cramb (1995) did. Comparing the errors induced by either assuming the relation between densities and weight percentages of Si or the temperature correction that is required is not possible and therefore no conclusion can be drawn on the relative reliability of the results.

In general, a similar conclusion can be drawn for the FeSi density results as for the FeS. Again, a large difference is observed between the convective and conductive solution, as a result of the temperature profiles. Repeatedly, it is not likely that the whole mantle consists of an FeSi-alloy and a basal layer of ~15 km is more probable. In this lower region, the density differences are then for all weight percentages of Si roughly equal.

	FeS - liquid	FeS - solid	Fe-0wt%Si	Fe-10wt%Si	Fe-17wt%Si	Fe-17wt%SiX	Fe-20wt%Si
ρ_0 [kg/m^3]	3900 ± 98	4400 ± 110	7079	6401	5955 ± 179	7147	5770
T_{ref} [K]	1473	1000	1723	1723	1723	300	1723
α [K^{-1}]	$1.1 \cdot 10^{-4}$	$10.4 \cdot 10^{-5}$	$9.2 \cdot 10^{-5}$	$9.2 \cdot 10^{-5}$	$9.2 \cdot 10^{-5}$	$6.4 \cdot 10^{-5}$	$9.2 \cdot 10^{-5}$

Table 4.3: FeS and FeSi parameters that are used to quantify the density differences between different temperature regions. The Fe-17wt%SiX is the data that is retrieved from dedicated Fe-17wt%SiX experiments, rather than from the experimental relation. (Hauck et al., 2013)

$\rho_{0,a}$ [kg/m^3]	2361
$\rho_{0,b}$ [kg/m^3]	-7015
$\rho_{0,c}$ [kg/m^3]	7079

Table 4.4: FeSi parameters for the calculation of the density of an FeSi-alloy with an x percentage of silicate (Hauck et al., 2013).

As expected, and as also observed previously in the Perple_X results, the density at the warm regions, i.e. the positive gravity anomaly regions, is relatively low. This is contradictory with the observation that at these warm regions there is a positive density anomaly. If indeed the surface temperature anomaly propagates through the mantle as Tosi et al. (2015) predicts that it will, this negative density anomaly needs to be counteracted by a larger positive anomaly to explain the gravity observations. A possibility is that the alleviation of the lack of mass in these regions allows for a slight rise of the CMB, inducing at this same location a positive gravity anomaly. This hypothesis is further tested in Section 4.3.3. For that analysis the FeS liquid density profiles are used (as there is merely any difference between FeS liquid and solid material), and the FeSi alloy with 10wt% silicate. Lower weight percentages would imply very high mantle densities (~7000 kg/m^3) and higher weight percentages imply density differences similar to the FeS-alloy.

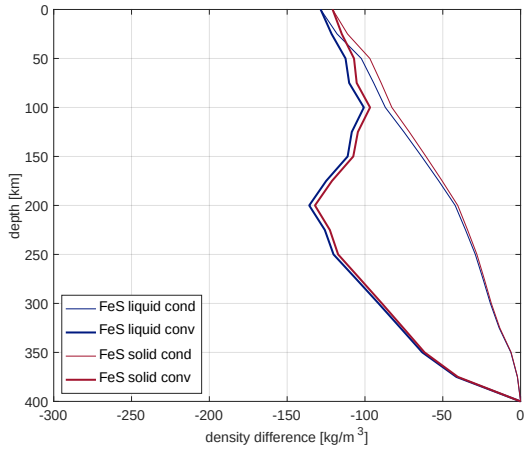

Figure 4.13: The density differences in an FeS model at a certain depth in Mercury, as a consequence of temperature differences.

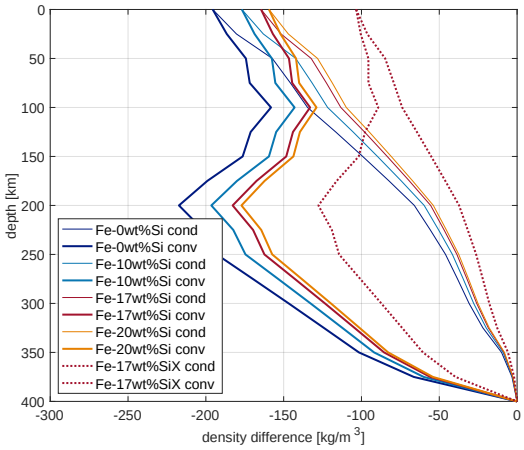

Figure 4.14: The density differences in an FeSi model at a certain depth in Mercury, as a consequence of temperature differences.

4.3.3. Core-mantle boundary topography

From the density differences calculated in Sections 4.3.1 and 4.3.2 eight models are selected that are subjected to further analysis. All these mantle models predict a negative density difference in the high-temperature region with respect to the low-temperature region. The density profiles are plotted in Figure 4.15. The gravity fields that these mantle profiles produce are included in Figure 5.24.

Please note that in the figures the density *differences* are plotted. Gravity anomalies are sensitive to density differences, rather than to absolute values of the density. Therefore, the value of the actual density does not matter (at least not in the domain that is studied in this research) and the density differences are leading. A density difference of 7400-7200 [kg/m^3] will give the same results as a density difference of 5400-5200

[kg/m^3]. Therefore, the density models that are selected for further investigation are found to be a representative reflection of all the models. They comprise a wide range of density models, including convective and conductive, simple and complicated models.

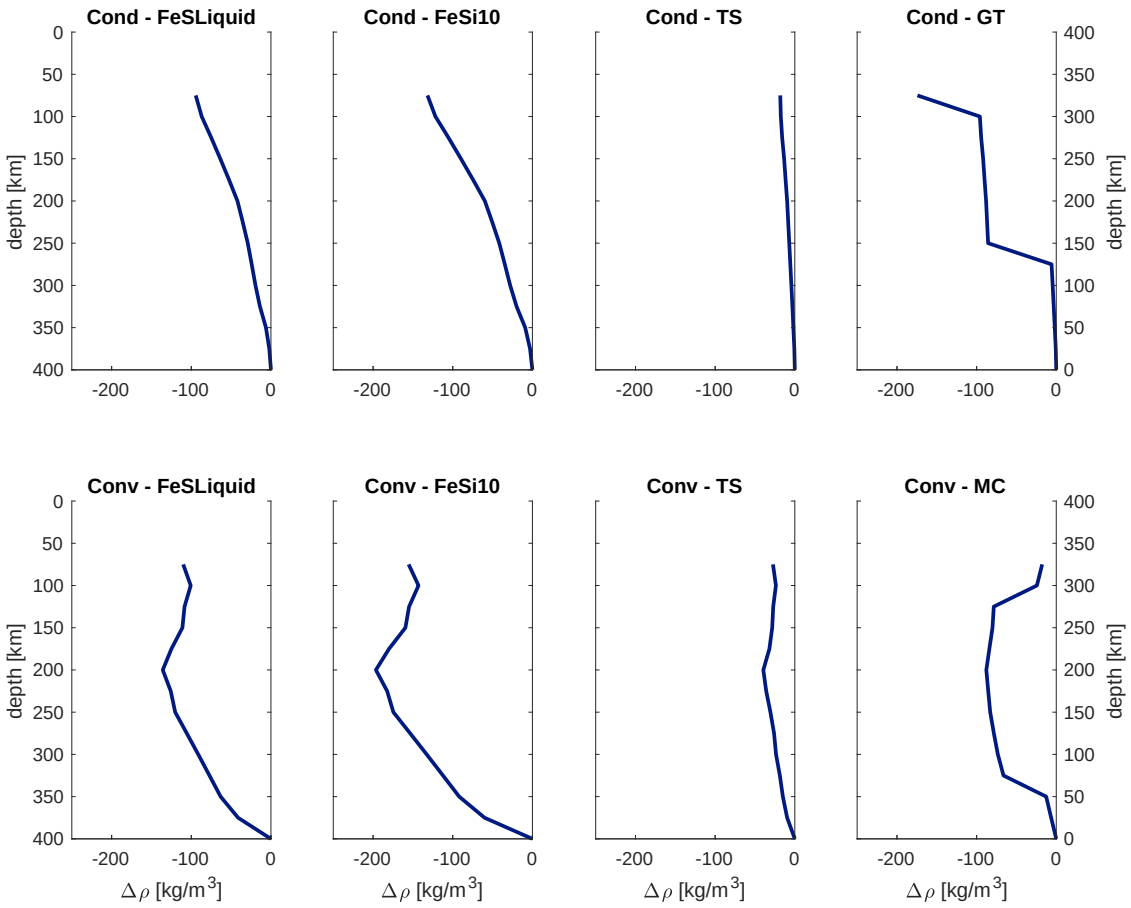

Figure 4.15: Mantle density profiles selected from previous analyses that are used as input for the fitting of CMB variations. The top figures represent a conductive mantle, the bottom figures a convective mantle. The CMB is on average located at 400 km.

The eight selected mantle profiles are displayed in Figure 4.15 and combined with the three crustal models from Section 2.7. The residual of these crust-mantle models are subjected to fitting of the CMB. This fitting is established by allowing the CMB to rise, and in that way inducing gravity anomalies. This scenario is probable to actually exist in planets (Tosi et al., 2015). In Figure 4.16 the required CMB variations are plotted for each combination of crust and mantle model. Two possible mantle-core density contrasts are considered: 2000 kg/m^3 (Hauck et al., 2013) and 3600 kg/m^3 (Tosi et al., 2015). Given the temperature and pressure characteristics of Mercury, these are considered realistic values - as a comparison: the core-mantle density difference in Earth is observed to be ~5000 kg/m^3 (Volgyesi and Moser, 1982).

Comparison with Figure 5.24 immediately shows that there is a clear relation between the size of the CMB variations and the magnitude of the density anomaly. For the Airy and Bouguer models it is observed that the spread in the CMB location is proportional to the average thickness of the layer, i.e. with a thicker layer the variations also become larger in absolute magnitude. For James this relation does not hold. This is most likely the result of the approximate similarity between the induced gravity anomalies, Figure 5.24, and the residual gravity field after subtraction of the James crustal gravity field, Figure 2.21c. Relative to the previous results, where the James model always required the largest density and thickness compensation, the results of James seem to be dampened, which indicates that the James crustal gravity field matches well with a mantle models that contain a temperature anomaly. Furthermore it is observed that, with respect to the previous results in for example Figure A.2, the results of the different crustal models are in a much more similar range. This is

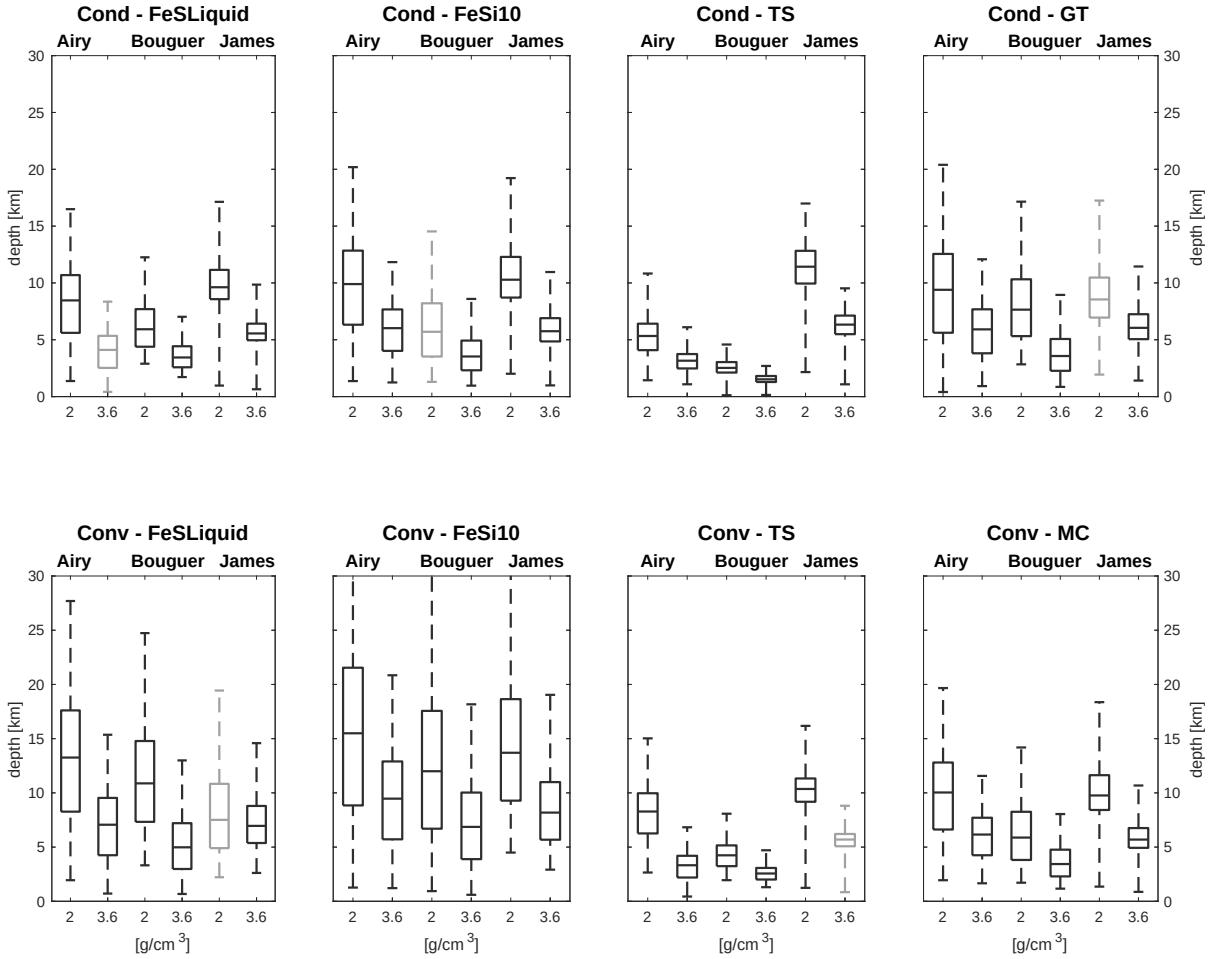

Figure 4.16: The results of the CMB fitting, including the mantle density anomalies as a results of temperature differences. Each subplot represents one density profile and contains the results for Airy (left), Bouguer (middle) and James (right). The density increments are 2 and 3.6 g/cm^3. The grey boxplots indicate non-convergence, i.e. a remaining residual > 10 m.

the result of the additionally induced gravity anomaly that dominates the total gravity anomaly and therefore the CMB variations. For the *Cond - TS* model, where the induced mantle density anomaly is small and where the crustal features are still best visible, it is evident that this equalisation has not happened, hence the large differences.

The reason that the variations in CMB location do not commence at 0, i.e. at the initially modelled location of the CMB-layer, is the results of how the fitting algorithm works. The software adds mass at locations where it is expected that this is needed, and to prevent the CMB to be deeper than 440 km, the software does not allow for subtraction of mass. The only solution for the compensation of negative anomalies is creating a mass excess at other locations, hence the layer does not start at 0 km.

The modelled density anomalies are rather extreme in the sense that they range over a large depth and comprise large density differences between the hot and cold regions. It is the question whether such large density differences would sustain over longer times, and whether it is not more likely that a form of convection would equal these anomalies out. The consequential CMB variations are also of extreme proportion. Comparing these modelled CMB variations in Mercury with the modelled CMB variations in Earth of ~12 km (Soldati et al., 2013), these results seem too high.

James et al. (2014) also investigated a rise of the CMB but in a slightly different context. He investigated how thinning of a hypothetical FeS-layer would allow for a rise of the CMB, scaled according to the density difference. He related the effect of these anomalies to the topography, and found that 10-15 km of thinning of the basal layer would induce 1 km of topography. The observed topography on Mercury is in the range of -4 to 2 km, and in terms of CMB rises this would lead to of several kilometres of upward deflection, depending on the density ratio between the thinned basal layer and the core. This would roughly comply with the values found in this study.

The CMB topography calculated by the model of Tosi et al. (2015) is only a few tens of meters, which is not in line with the findings in this thesis. This could be the result of the spherical harmonic degrees that are included, namely merely SH2 and 4 by Tosi et al. (2015) versus SH2-10 in this study. Furthermore, Tosi et al. (2015) include, apart from density variations induced by the irregular insolation pattern of the Sun and CMB variations, also the 1) flexural loading of the crust by including the elastic thickness of the lithosphere in the calculations and 2) take into account viscosity by considering mantle convection. Where in this analysis it is investigated how the (almost) full SH10 gravity field can be compensated by CMB variations, Tosi et al. (2015) considered a part of this field and add additional compensation factors on top of this. Looking at the results for a flexural response filter in Figure 2.9 of a model with T_e = 100 km (Tosi et al. (2015) used an elastic thickness of 110-180 km), the flexural response model (thin, blue line) shifts the gravity signature of the crustal model indeed closer to the observations (thick, red line). This would then indeed result in smaller CMB-variations, however not likely with the magnitude that is required to explain the discrepancies between the two studies. This can be explained by Tosi et al. (2015) also running mantle convection models and thus considering the viscosity of mantle material. This alters the analysis further and (apparently) allows for even smaller CMB variations. The two studies are thus not comparable.

5

Verification & Validation

Verification and validation is performed throughout this study. When applicable the verification and validation measures are explained along with the methodology and/or results. In addition to these practices, also the steps outlined in this chapter are taken, to assure the veracity of the results and conclusions.

5.1. Data set verification

The datasets that are used are the gravity field coefficients up to spherical harmonic degree 50 (GGMES_50v06 or HgM005) and topographic field coefficients up to spherical harmonic degree 150 (GTMES_150v01). These are verified using the available publications about these datasets. The datasets are given in spherical harmonic coefficients, however they are often presented in the form of a map. Therefore, software is needed that converts these coefficients into a map of Mercury. The software that is used to do this is in this way also verified. It should be noted though that this software has already been verified before, however testing it again can do no harm.

In Figure 5.1 the topographic map is compared to the topography map constructed by (Wieczorek, 2015). The high resemblance between the two plots is immediately clear. The topographic map of (Wieczorek, 2015) is overlain by a gradient map of the topography, therefore the image seems to be of higher resolution, however this is not necessarily the case. Based on this comparison the coefficient data and the code that computes a topographic map from the coefficient data is verified.

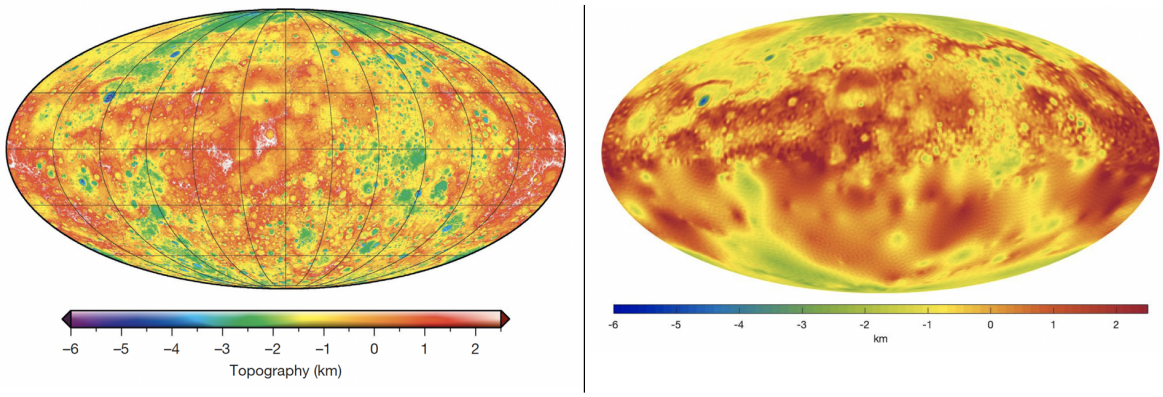

Figure 5.1: Verification of the topography. Left plot is retrieved from (Wieczorek, 2015).

There are several models of the gravity data available, constructed from the data that the Mariner 10 flyby's and the MESSENGER flyby's and its orbital period provided us with. Literature often does not show the full gravity field of a planet, but the so-called free-air anomaly. With the GSHA software package the free-air disturbance instead of the free-air anomaly is constructed. The difference between these two is the altitude that

the gravity field is references to. In case of the free-air anomaly the gravity at the location of the ellipsoid is subtracted, while for the free-air disturbance the gravity at the location of the geoid is deducted. Because of the high resemblance between the two and the very low number that we are taking about, it it assumed that the free-air disturbance can be verified with the free-air anomaly. To assure the veracity of the free-air disturbance, several tests are performed. (N.B.: The software is already verified by Root et al. (2016).)

Firstly, the HgM002 gravity field (or GGMES_20v04) is verified. Wieczorek (2015) computed a map of the free-air gravity anomaly, that is displayed in Figure 5.2, along with the computed map. Although it was not specifically stated, it looks as if the author models the same gravity field as is used throughout this study. The field maps show a high level of resemblance, and only minor differences are observed. This not only verifies the data (and the software), but also confirms the validity of the assumption about what coefficients to use.

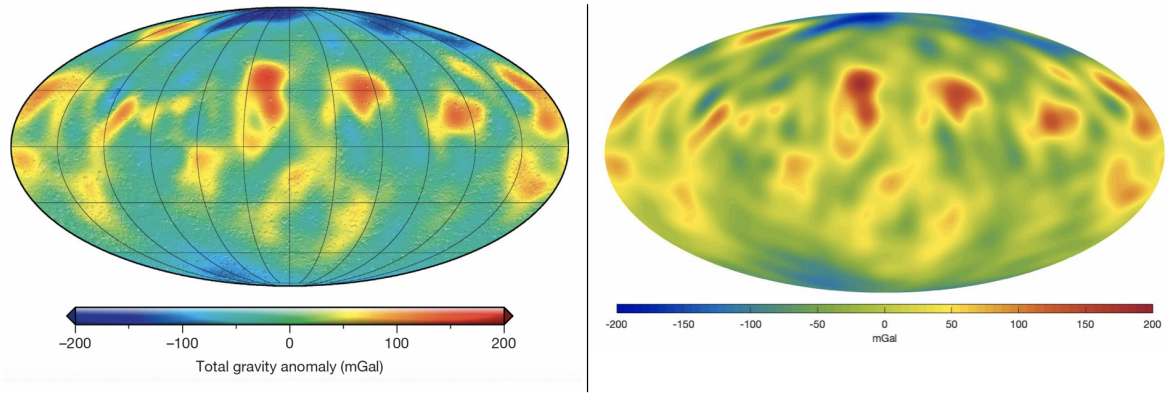

Figure 5.2: Verification of the free-air gravity anomaly from GGMES_20v04, both of the software that transforms the retrieved coefficients into a map and verification of the actual coefficients. Verification data (left plot) is retrieved from (Wieczorek, 2015).

In Figure 5.3 the free-air anomaly of the HgM005 model (or GGMES_50v06) as described by (Mazarico et al., 2014) is compared to the free-air anomaly that was constructed for this thesis. It is difficult to properly verify the data, as 1) it is again not clearly stated what is meant by the free-air anomaly and 2) the field map is at every location expanded to the available local degree strength. The results in Figure 5.3 do, as expected, not fully correspond, and the constructed map seems to have a positive offset with respect to the verification data. Playing around with the coefficient set did however not yield any improvement, and contacting the authors did unfortunately not give any response. Based on the roughly similar structure of the gravity field it is however concluded that the data is correct and that the software is indeed doing what it is supposed to do.

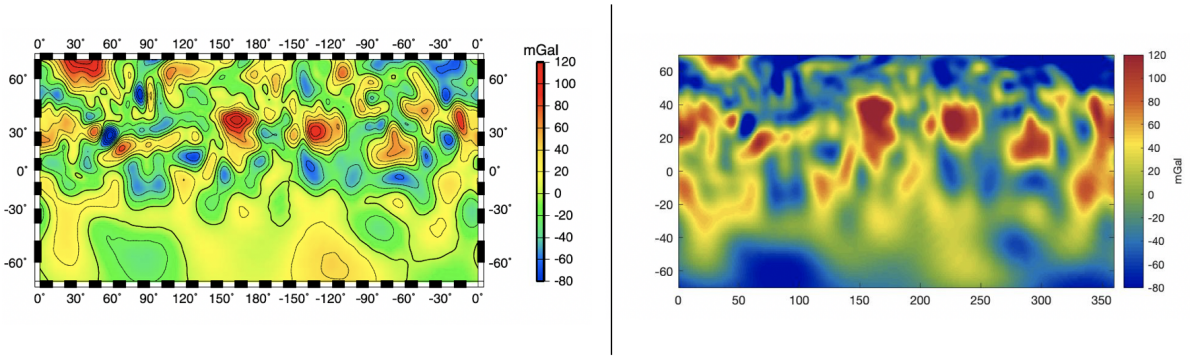

Figure 5.3: Verification of the free-air gravity anomaly from GGMES_50v06, both of the software that transforms the retrieved coefficients into a map and verification of the actual coefficients. Verification data (left plot) is retrieved from (Mazarico et al., 2014).

5.2. Spectral analysis

As a means to further inspect the power of the coefficients and relations between them, a spectral analysis is performed such as Wieczorek (2015) does. The two plots are presented together in two upper plots in Figure 5.4, and use the datasets that were available at the time of writing of (Wieczorek, 2015) (GGMES_20v04 and GTMES_24v01). The comparison of the two upper figures and the two lower figures show that the coefficients that are at hand are indeed the same, but most important of all that the mathematical method to calculate the power spectra and admittance and correlation spectra are correct. In the rest of this study the datasets with spherical harmonic degree 50 (gravity) and 150 (topography) are used, and this verification is thus mainly useful for the calculation method of the power spectra and admittance and correlation.

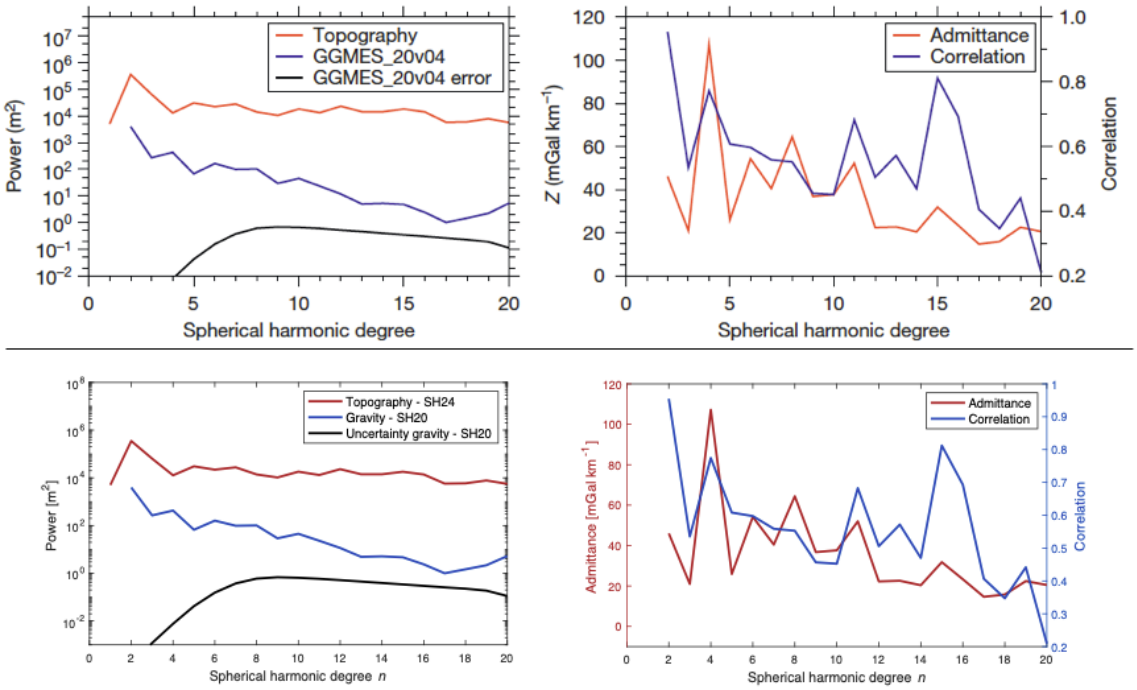

Figure 5.4: Verification of the power spectra of gravity and topography and the admittance and correlation calculations. Verification plots (upper plots) are retrieved from (Wieczorek, 2015).

5.3. Bouguer Anomaly

The Bouguer anomaly is constructed using the gravity and topography data. Although the Bouguer anomaly is often used in literature for the analysis of topographic features or estimation of the crustal thickness, not so many actual maps of the Bouguer Anomaly are available. The verification of the Bouguer Anomaly is therefore performed using data from (Qingyun et al., 2018), that unfortunately does not analyse a fully reproducible situation. The major difference is the free-air gravity anomaly field that is being used. The verification data is based on the HgM007 model, the gravity field of Mercury expanded to spherical harmonic degree 70. This gravity field was constructed by the authors themselves, and is not open source available online. Furthermore do the authors not fully specify the settings and assumption they made, making the comparison rather arbitrarily. Differences between the two plots could also be the result of the reference Bouguer anomaly being the extended Bouguer anomaly, while the computed gravity field is the result of topographic reduction. Although the two should be highly similar, minor differences could occur.

The reliability of the Bouguer gravity anomaly map from (Qingyun et al., 2018) was validated in their study based on the topographically obvious impact basins. In Figure 5.5 the comparison of the two maps is shown, and the two plots are assigned the same scale. It is immediately obvious that the constructed Bouguer anomaly shows a positive offset with resepct to the reference Bouguer anomaly. Characteristic features are more prominent in the reference anomaly, although they are also still clearly distinguishable in the anomaly that was constructed for this thesis. Based on the (roughly) similar outline and magnitude of the Bouguer

anomalies, the Bouguer anomaly is considered to be verified.

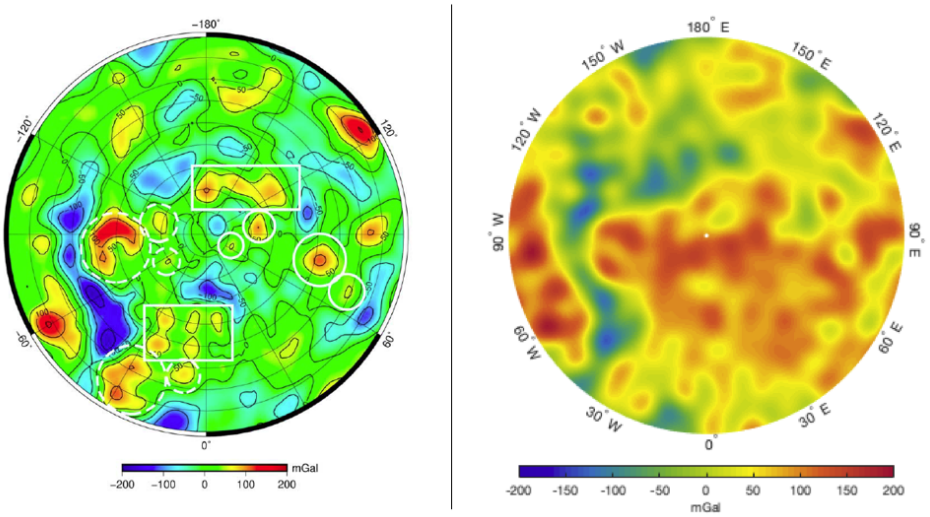

Figure 5.5: Verification of the Bouguer anomaly. The left plot shows the Bouguer anomaly as constructed by Qingyun et al. (2018). The right plot is the calculated Bouguer anomaly, that is based on the free-air gravity anomaly up to spherical harmonic degree 50 and the topography of similar accuracy. The crustal density is set to 2800 kg/m^3.

5.4. Crustal models

5.4.1. Bouguer - iterative approach

The crustal thickness that is calculated from the Bouguer anomaly using the iterative approach, is verified using (Wieczorek, 2015). Wieczorek (2015) calculated the crustal thickness based on the data sets that are expanded up to spherical harmonic degree 20 and the reproduction of this crustal thickness map is given in Figure 5.6. Both maps show an almost 1-on-1 similarity and give the same crustal thickness range. Although (Wieczorek, 2015) does not fully state the assumptions he made, the maps seem to correspond and with this comparison the code is verified.

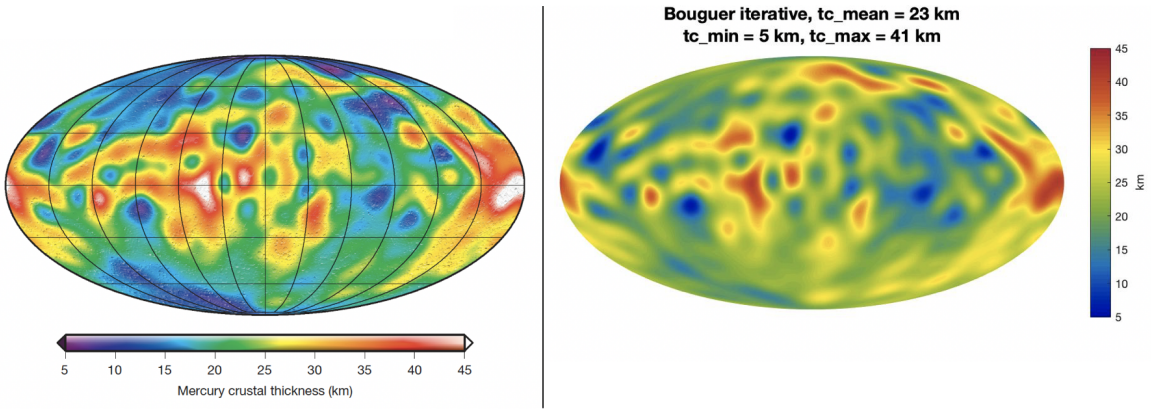

Figure 5.6: Verification of the Bouguer crustal thickness calculation method. The left plot shows the crustal thickness that was constructed by Wieczorek (2015). The right plot is the calculated crustal thickness, that is based on the free-air gravity anomaly expanded up to spherical harmonic degree 20 and the topography of similar precision. The crustal density was set to 2900 kg/m^3, the crust-mantle density difference to 300 kg/m^3 and the mean crustal thickness to 23 km.

The Bouguer correction, Bouguer anomaly and also the crustal thickness that results from these maps are further verified using the results of (Mazarico et al., 2014). Again, Mazarico et al. (2014) use the data expanded up to the local degree strength. As this data is not widely available, the comparison between the reference

data and the calculated data is not one-one-one. The comparison is shown in Figure 5.7. Both the calculated Bouguer correction (top figures) and the subsequent Bouguer Anomaly (middle figures) are relatively large in magnitude. The outline of the left ((Mazarico et al., 2014)) and right plots (self computed) are similar however. The plots of Mazarico et al. (2014) have a smoother outlook, probably because of the degree strength that are used. Based on the comparison of the plots, it is concluded that the code, method and produced data is verified, however one should keep in mind the relatively large magnitude of the maps in comparison with literature and possibly correct for this in later stages.

The resulting crustal thickness maps are displayed in the bottom plots. Mazarico et al. (2014) do not describe the exact approach they use, nor the settings of their approach, making the comparison again difficult. The outlook of the crustal maps are again similar, although the resemblance is to a lesser extent when compared to the upper plots of the Bouguer correction. The magnitudes of both maps seem reasonable as well. Based on this comparison it is decided that the computed crustal thickness map is reasonable can be used as input for the rest of the research.

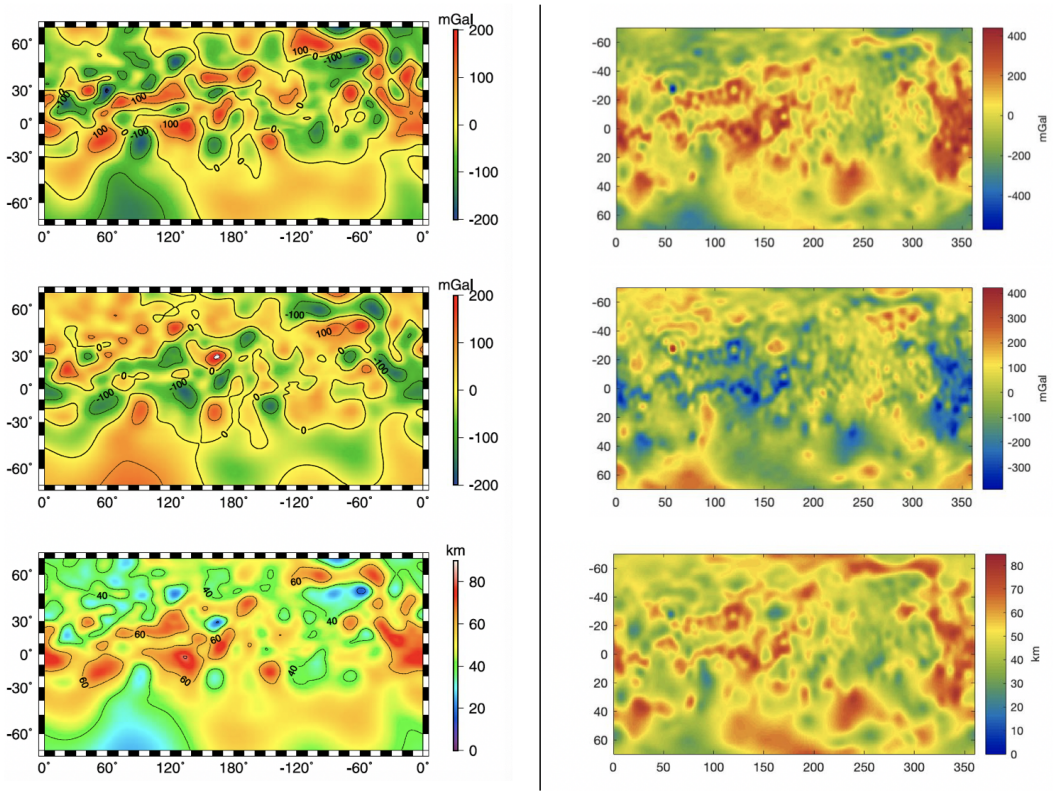

Figure 5.7: Verification of the (top) Bouguer correction, (middle) Bouguer anomaly and (bottom) resulting crustal thickness. The left plots show the data as constructed by Mazarico et al. (2014), at each point plotted up to the local degree strength. The right plots are the calculated values, based on the free-air gravity anomaly up to spherical harmonic degree 50 and the topography of similar accuracy. The crustal density is set to 3200 kg/m^3 and the crust-mantle density difference to 250 kg/m^3.

5.4.2. Airy, Pratt & Bouguer - Linear

The other three approaches in crustal modelling are relatively simple calculations, and allow for verification by hand. Using Equations 2.1, 2.2 and 2.6 the values calculated by the algorithm can be compared to the values calculated by hand. Of course, this only verifies single values, not all, and does not say anything about the actual approach. To verify the methods in a more general fashion, crustal thickness plots were regularly plotted - to check their magnitudes, orientation, outliers etc. This gave satisfying results.

5.5. Flexural isostasy

Verification of the flexural isostasy method and code is performed by comparison of a flexural isostasy analysis for Earth as performed by (Watts, 2001). The plots in Figure 5.8 show identical results and therefore it is concluded that the code performs as it should. Of course, for the case of Mercury the input parameters are changed. These input parameters will be based on literature and own experience/judgement. There is however no comparable study been published for Mercury, and therefore verification of Mercury's case is not possible.

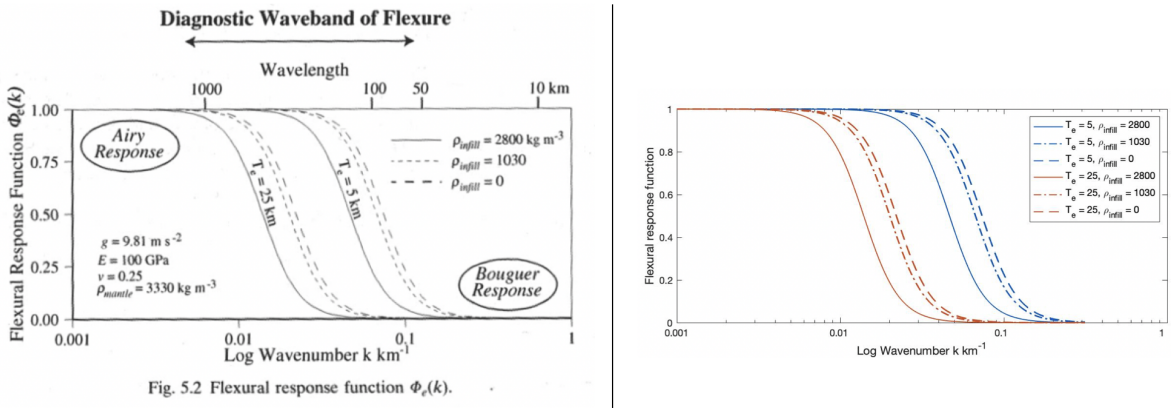

Figure 5.8: Verification of the flexural response function for Earth's crust. Verification plot (left plot) retrieved from (Watts, 2001).

5.6. Convergence

Two types of convergence need to be assessed in this analysis, namely the maximum thickness of a layer, $t_{c,max}$, and the maximum variation of the radial location of the crustal bounds, $t_{c,variation}$. The difference is illustrated in Figure 5.9.

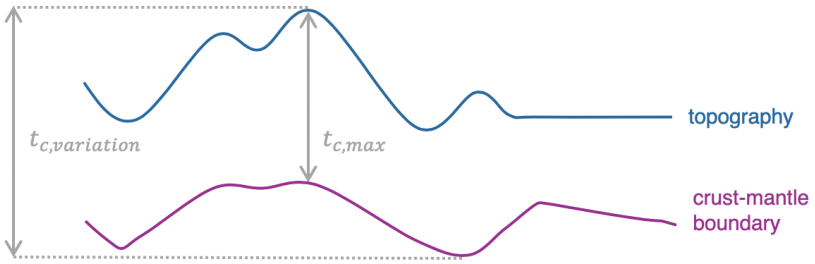

Figure 5.9: Illustration of the two different convergence criteria that are being used. $t_{c,max}$ indicates the maximum thickness of a layer, $t_{c,variation}$ indicates the maximum variation in radial location of the crustal bounds.

Root et al. (2017) performed an extensive analysis to assess the $t_{c,max}$ of the GSHA software package. It was calculated at what combination of analysis depth and spherical harmonic degree the error would exceed a 50% margin. According to Figure 3 in (Root et al., 2017), for spherical harmonic degree 50 this error margin would be exceeded at a layer depth of 180 km, for the case of Earth. As Mercury is a smaller planet, and therefore spherical harmonic degrees correspond to different wavelengths, the convergence requires new attention. In Figure 5.10 the spherical harmonic degree is calculated up to which the calculated gravity of a layer at a certain depth is accurate.A slight shift in the curve is observed, that can be attributed to the difference in radii. For a given accuracy of spherical harmonic degree 50, the layer depth can be up to 200 km. This means that that according to this calculation, the layer thickness must not exceed 200 km to preserve a calculation within 50% error margin. This thickness will generally be too large, because of the expected density variations within a 200 km bound. Furthermore is the error margin of 50% too large for this study, and we require a more accurate model.

In Figure 5.11 the power spectrum of the gravity model for a fully compensated Airy-Heiskanen model is plotted, calculated using different thicknesses of the layers, to asses the impact of $t_{c,variation}$. In this wording, *a layer* does not point to the whole crustal layer or mantle layer, but with *a layer*, a layer subject to analysis is meant. This layer contains in most cases a part of the crust or a part of the mantle. To allow for convergence, the maximum radial variation of the bounds of such a layer is of importance. This thickness is not only constrained by the thickness of a layer, but also by the range in the radial location over which it extends. In Figure 5.11 it is observed that a maximum thickness of 80 km, which results in one topography layer, one crustal layer and one mantle layer gives erroneous results. From a maximum range of 40 km onwards the software shows convergence, and therefore for the analysis 40 km is set as maximum variation in the crustal bounds of a layer.

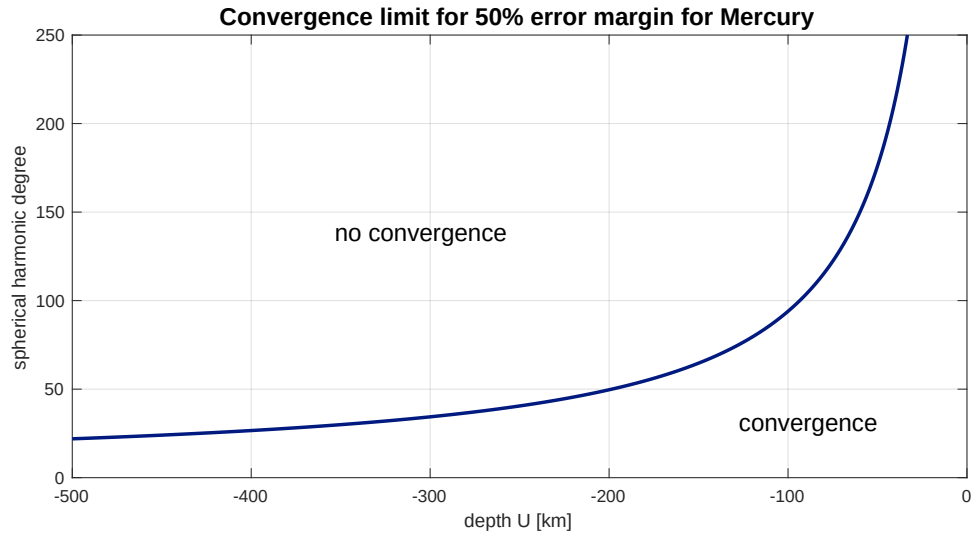

Figure 5.10: Convergence testing of the software for Mercury - analysis of the effect of the depth of a layer

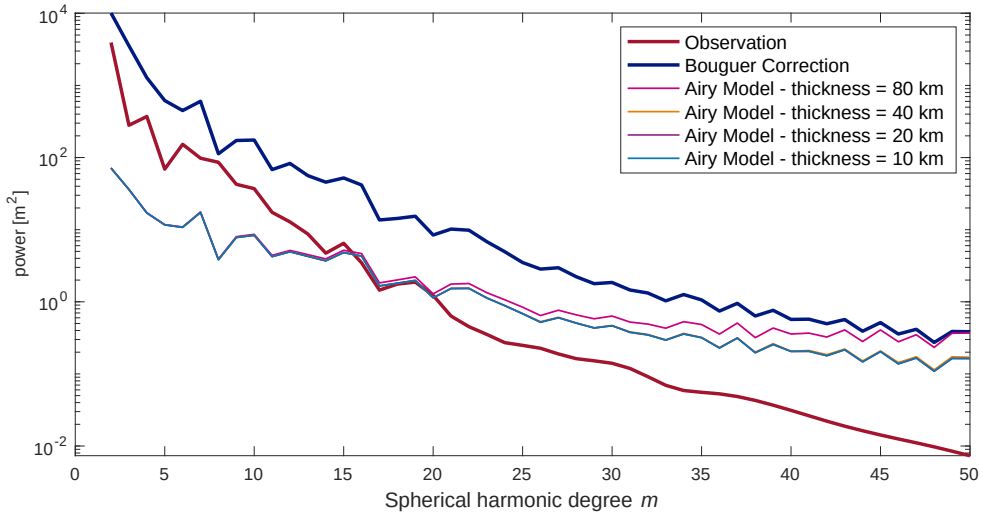

Figure 5.11: Convergence testing of the software for Mercury - analysing the effect of the range in depth that the layer spans. In this particular plot the gravity from the Airy crustal model is calculated.

5.7. Spherical harmonic truncation

In Figures 5.12 and 5.13 the residual gravity fields are shown for the Airy-Heiskanen and Bouguer linear approximation crustal models of which the density is fitted to the observed gravity field corresponding to a certain spherical harmonic degree and higher. For example, for the upper plot in Figure 5.12, the crustal model that results from Airy-Heiskanen isostatic compensation is used, and the density of the crust is adjusted such that it fits the observed gravity field for spherical harmonic degree 5 and higher.

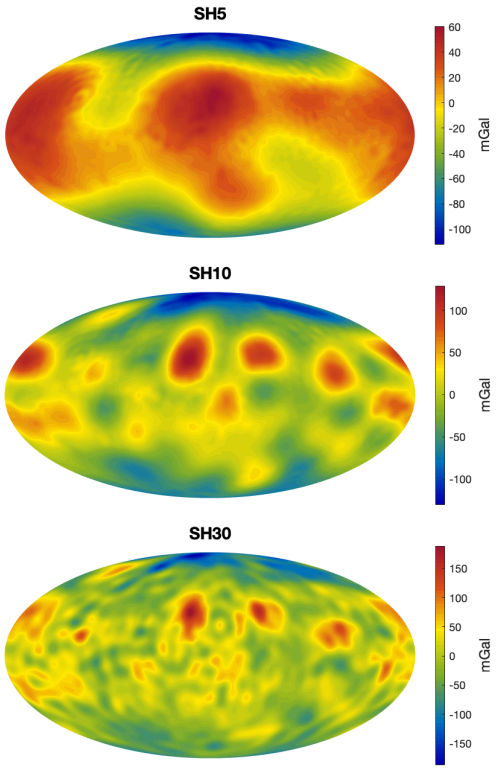

Figure 5.12: Comparison of gravity field strength for different resolutions in spherical harmonic degree for the Airy-Heiskanen model. The spherical harmonic degree in the title of each plot indicates the spherical harmonic degrees that are included, and all higher degrees are compensated by fitting density increments.

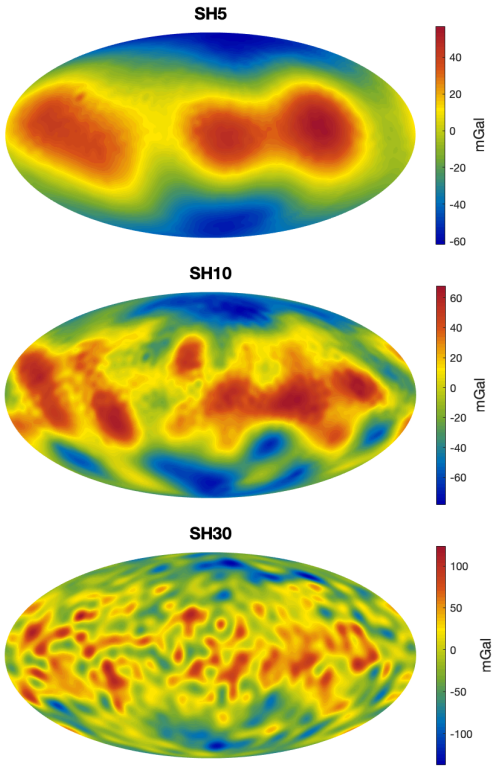

Figure 5.13: Comparison of gravity field strength for different resolutions in spherical harmonic degree for the Bouguer linear approximation model. The spherical harmonic degree in the title of each plot indicates the spherical harmonic degrees that are included, and all higher degrees are compensated by fitting density increments.

In Figure 5.12 it is observed that the SH10 and SH30 fields look similar. The SH30 field shows, as expected, a more granular outlook, as a result of the smaller-wavelength features that are included. The magnitude of both fields is comparable: in the negative (blue) range, the fields are of equal magnitude, in the positive range (red) the SH30 field is slight stronger than the SH10 field, reaching maxima of 150 mGal and 100 mGal respectively. The global outlook is similar however, and apart from the discrepancy in the maxima, the magnitudes of the fields are roughly the same, (keeping in mind the differing colour scales being used). The cut-off at spherical harmonic degree 10 is a valid assumption in terms of the upper threshold.

Between the Airy SH5 and SH10 fields a relative large discrepancy is observed in comparison with the number of spherical harmonic degrees that are excluded additionally. The long-wavelength features (low SH degree) are often stronger in magnitude and therefore the discrepancy can be expected. Again, the minima of the models is the same, the maxima differ. The outlook of the SH5 is much more global and does not indicate characteristic features as clearly as the other models, that are also observed in the topography. This might be an indication that these features are more likely caused by crustal anomalies rather than deep mass anomalies, given that they occur more obviously in the shorter-wavelength gravity field and are evident in the topography. The data sources are however too scarce to confidently draw this conclusion.

In all three Bouguer models in Figure 5.13 a similar outlook is observed, with increasing granularity with increasing spherical harmonic degree. The magnitude of the field slightly increases from SH5 to SH10 (~ 25%), and increases even more towards SH30 (~ 50%).

With this analysis the variation of the gravity field with spherical harmonic degree is quantified, in order to assess the effect of the SH10 assumption. The consequence of the assumption is fair, however not significant. The magnitude of the gravity field increases reasonably with the inclusion of more spherical harmonic degrees, however this behaviour does not render the assumption of the division between deep mantle and crustal variations at SH10 invalid.

5.8. Sensitivity analysis of fitting algorithm

In Figures 5.14 and 5.15 the sensitivity of the density and thickness fitting results to the input parameters are investigated. As is visualised in Figure 4.1, the variable input parameters for the density fitting process are the 1) initial density increment - that is the increase in density that is initially added to the basal layer, before the start of the fitting procedure - 2) the initial fitting increment - so the initial variation in the density across the basal layer that is incorporated - and 3) the magnitude of the threshold that is set as the criterion for convergence. The sensitivity of the algorithm to these input parameters are investigated in Figure 5.14, from left to right respectively.

The selection of the initial density increase has no effect of the final density range that is calculated. Free-air gravity anomalies are caused by relative density variations, and the absolute magnitude of the densities - that can also be seen as an offset - does not affect the results. The absolute values of the densities are obviously, variable across the different runs, however the spread in the density values is not. To constrain the absolute magnitude of the density, one should include mass and moment of inertia calculations to determine the compatibility of the mantle model with these results. The selection of the fitting factor - that is the amount of density that is added/deducted per iteration, with the aim to fit the gravity anomaly field - does not influence the final outcome. This parameter thus affects the computational effort that is required, and from that perspective optimisation is desirable, however in terms of mathematical correctness this parameter is of no concern. The selection of the threshold does affect the results: with an increasing threshold (so a larger margin in the residual), the range in density decreases. A margin of 1 or 5 m is too tight and can not be achieved, up until a value of 20 m the density range is similar. Therefore the 10 m margin is considered good convergence criterion.

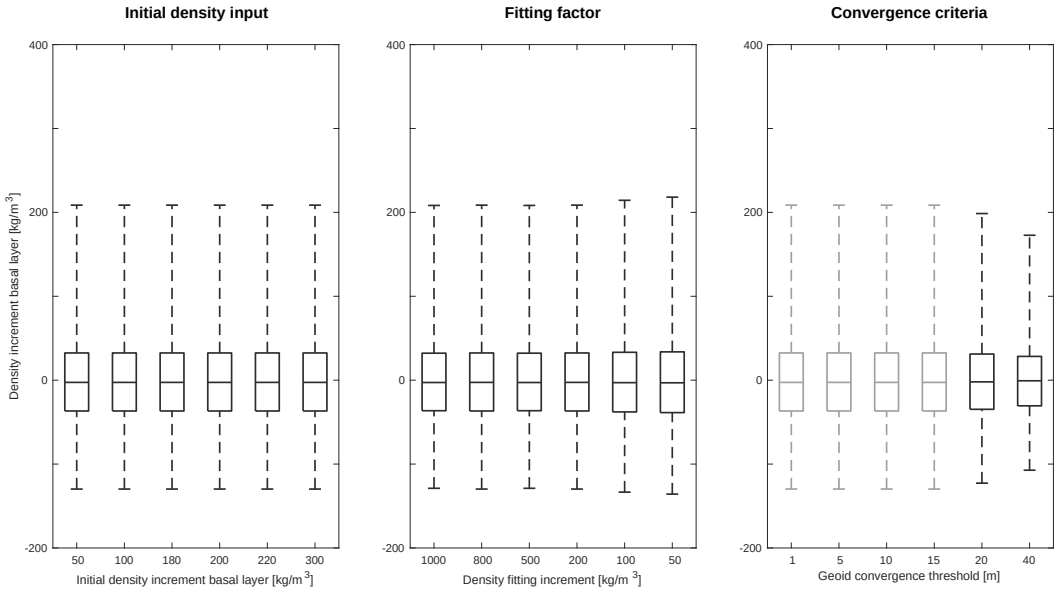

Figure 5.14: Sensitivity analysis of the density fitting technique for the Airy crustal model. A light grey curve indicates no convergence, i.e. the threshold is exceeded.

The variable input parameters for the thickness fitting process are slightly different than for the density fitting. 1) Initial thickness increment - that is the initial thickness of the constant-density basal layer, before the start of the fitting procedure - 2) the initial fitting increment - so the initial variation in the thickness across the basal layer that is incorporated - and 3) the magnitude of the threshold that is set as the criterion for convergence. The sensitivity analysis shows that the the fitting factor (middle figure) again has barely any influence on the outcome. The non-convergence for the fitting increment of 2 km is the result of a too small fitting increment, resulting in a maximum deviation between the upper and lower bound of 15 iterations * 2 km = 30 km, which is too small, given the other results (-30,+45km).

The initial thickness input is of importance in this case. That has to do with the fact that when the thickness is adjusted, not only the thickness is adjusted, also the location of the centre of mass of that specific column is shifted. The change of one parameter thus influences two other parameters, resulting in the observation that the initial thickness of the basal layer is of importance: in case the initial thickness is located further away from the crust, larger thickness variations are required to obtain the same result. This is because of the relative smaller difference in the centres of mass when comparing to adjacent columns, when the layer is located further away from the surface of the planet.

In the third plot, similar behaviour as for the density fitting algorithm is observed. The difference is that already at a threshold of 10m the fitting algorithm starts to show discrepancies.

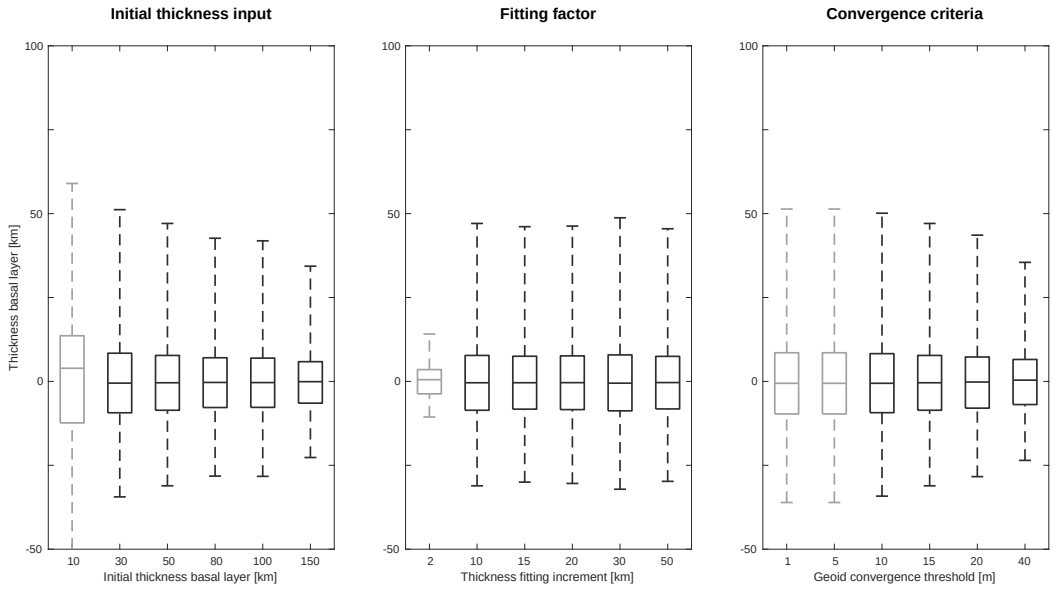

Figure 5.15: Sensitivity analysis of the density fitting technique for the Airy crustal model. A light grey curve indicates no convergence, i.e. the threshold is exceeded.

This sensitivity analysis is in line with the Airy-Heiskanen theory (Watts, 2001) and therefore this research verifies the outcomes of the density algorithm.

5.8.1. Further checks

Automatic checks are built in that make sure no impossible models are outputted, such as models where the mantle becomes too thick to leave room for a crust. In addition, during and after running the algorithm, several plots are outputted that allow for the investigation of the veracity of the results - is the algorithm indeed working towards convergence?, are the orientations correct?, do the numbers make sense?, etc.

5.9. FeS & FeSi density parameters

The calculation of the density of FeS and Fe-xxwt%Si alloys at various temperature conditions is based on the data stated in Hauck et al. (2013). The FeS data is available for both the solid and the liquid state of the alloy, and the density of both the materials include an error margin as indicated in Table 5.1. This error margin is narrow, and the impact of this error reduces even further in the context of this research. In this study the density contrast between two locations is used. Assuming that at these two locations the error in the density is most logically similar, the error would reduce to 0.

The maximum error that could possibly result from the input parameters, i.e. the maximum possible density in the cool region minus the minimum possible density in the hot region, is indicated in the shaded regions in Figure 5.16. The plot shows the error margin for the solid and liquid FeS material, both for a conductive and and a convective temperature profile. Each shaded region indicates the error margin that can result from the uncertainty in the input parameters for one specific case. For all four cases, the margin is rather small, at maximum 10 kg/m^3, an accuracy that can not even be detected in the current data of Mercury.

	FeS - liquid	FeS - solid	Fe-17wt%Si	solid Fe
ρ_0 [kg/m^3]	3900 ± 98	4400 ± 110	7147 ± 179	8170 ± 82
T$_{ref}$ [K]	1473	1000	300	298
α [K^{-1}]	1.1· 10^{-4}	10.4· 10^{-5}	6.4· 10^{-5}	6.4·10^{-5}

Table 5.1: FeS parameters (Hauck et al., 2013).

$\rho_{0,a}$ [kg/m^3]	2361
$\rho_{0,b}$ [kg/m^3]	-7015
$\rho_{0,c}$ [kg/m^3]	7079
T_0 [K]	1723
α [K^{-1}]	9.2· 10^{-5}

Table 5.2: FeSi parameters (Hauck et al., 2013).

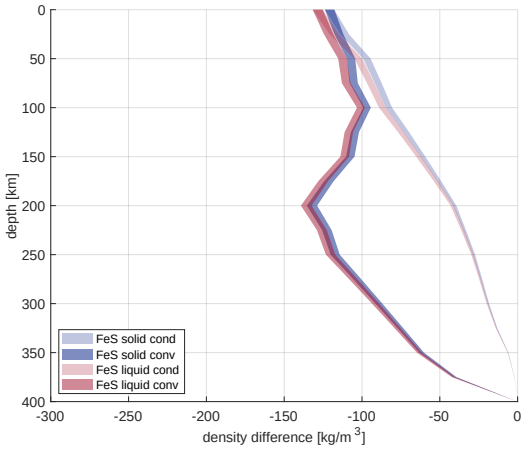

Figure 5.16: Verification of FeS calculations (Hauck et al., 2013).

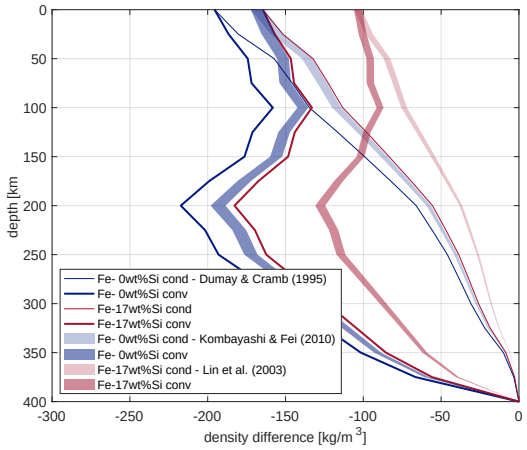

Figure 5.17: Verification of FeSi calculations (Hauck et al., 2013).

The density of Fe with an xx wt% of Si in it is calculated using a quadratic parametrisation of the Fe-Si liquid reference density at 1723K as a function of Si mass fraction (Dumay and Cramb, 1995; Hauck et al., 2013), see Equation 4.2. This relation is based on a scarce number of datapoints, although obtained from experiments conducted by several researchers. As a means of verification of the applicability of the relation in this specific thesis, data from measurements on the alloys containing the weight percentage Si of interest are used for comparison - namely that of 0 wt% (Komabayashi and Fei, 2010) and 17 wt% Si (Lin et al., 2003). The verification data contain an error margin that is, like for the FeS data, indicated as a shaded region for the four cases. The continuous lines indicate the values that are calculated using the experimental relation of Dumay and Cramb (1995). Both verification datasets confirm that the addition of silicon to an Fe member reduces the density. A discrepancy is observed however in level of reduction: the quadratic parameterisation overestimates the density difference up to 30 kg/m^3 at low weight percentages of silicon in the alloys, and underestimates the density differences in case of higher weight percentages (>17) up to 60 kg/m^3. These are numbers that need to be considered when interpreting the results. Actual measured data points are preferred over the experimental relation and experimental data from measurements closer to the reference temperature have preference as well.

5.10. Perplex

The Perple_X open-source software has built-in checks during the installation that verify that the code is working properly. Furthermore, as a means of verification I ran the *Seismic Velocity Tutorial*[1] to both become familiar with the software and verify the results. To verify my Perple_X results specifically, I ran three different thermodynamic models for each mantle composition.

1. The *hp02ver.dat* thermodynamic data file contains the data that resulted from the experiments conducted by Holland and Powell (2004). The *hp02ver.dat* is the default solution model used for the analysis of mantle compositions, and can handle all mantle components listed in Table 4.2 except for Cr_2O_3, Th and U. As the abundance of these minerals is very small for all mantle compositions, it is assumed that this has no severe implications on the calculation of the density, nor on the density differences.

2. The *stx08ver.dat* thermodynamic data file (Xu et al., 2008) can specifically handle the mantle materials of Mercury well, such as garnet, spinel and olivine. The disadvantage of this model is that it does not allow for the inclusion of mantle minerals other than SiO_2, Al_2O_3, MgO, FeO and CaO and Na_2O. This model is therefore used as a means of verification.

3. The third solution model *hp02ver.dat - reduced* is again the *hp02ver.dat* file, however all the elements that are not contained in *stx08ver.dat* are set to 0, to allow for comparison between the two.

In Figures 5.18 to 5.22 the density distributions in the five mantle models are plotted, using the aforementioned three solution models. All plots are displayed using the same density scale. It is observed that the three solution models produce quite similar results. The *hp02ver.dat* and the *hp02ver.dat reduced* show merely any discrepancy, indicating that the exclusion of TiO_2, MnO and K_2O does not affect the results. Given that a similar concentration holds for the fully omitted mineral Cr_2O_3, it is assumed that this has no severe implications either. The same holds for the very low abundances of Th and U.

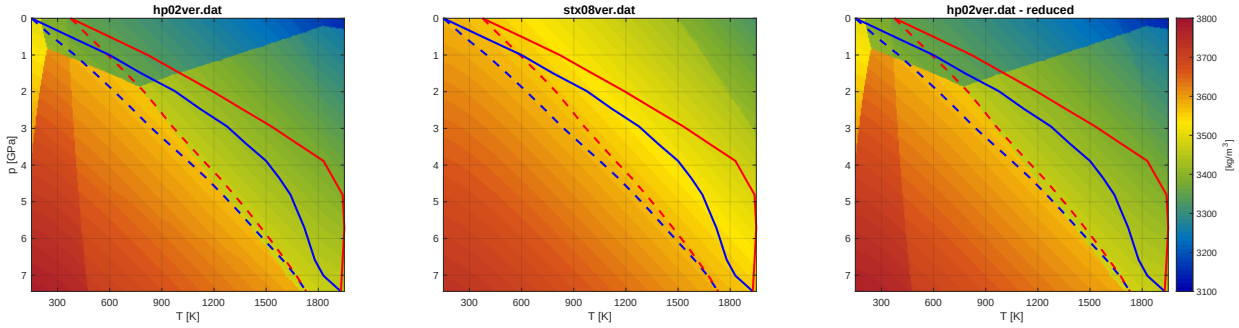

Figure 5.18: Density distribution of the FC model for different inputted solution models. The continuous line indicates the temperature distribution in the hot and cold part of the convective mantle, the dotted lines indicate that of a conductive mantle.

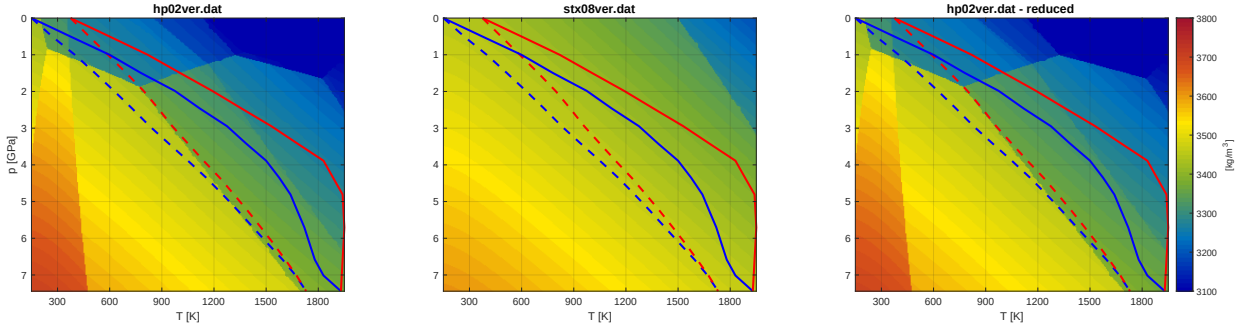

Figure 5.19: Density distribution of the GT model for different inputted solution models. The continuous line indicates the temperature distribution in the hot and cold part of the convective mantle, the dotted lines indicate that of a conductive mantle.

[1] `http://www.perplex.ethz.ch/perplex_66_seismic_velocity.html`

Comparing the *hp02ver.dat* model with the *stx08ver.dat* model shows that the latter produces often more smoother results, with less abrupt density transitions. The differences between the models mainly occur outside our regions of interest (the p,T-profiles indicated) and therefore are accepted. The magnitudes of the densities are in a similar range, however the minor discrepancies between the models is something to keep in the back of our head. Minor density differences throughout the whole depth of the mantle could induce a relatively large gravity anomaly.

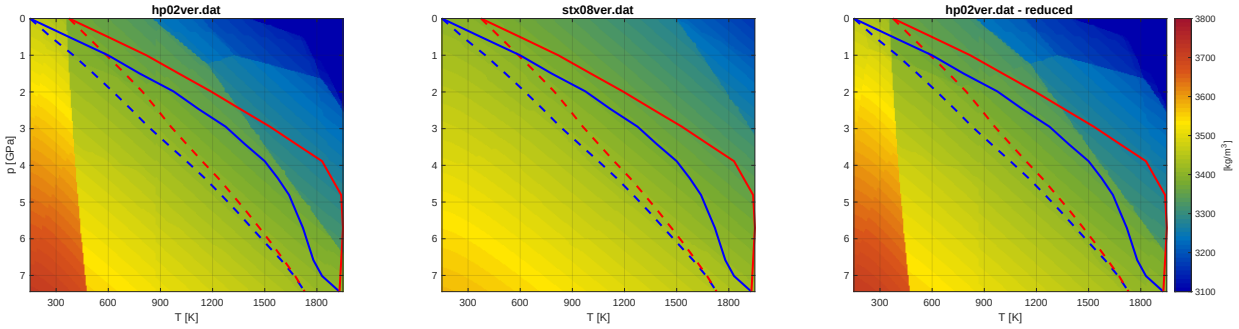

Figure 5.20: Density distribution of the TS model for different inputted solution models. The continuous line indicates the temperature distribution in the hot and cold part of the convective mantle, the dotted lines indicate that of a conductive mantle.

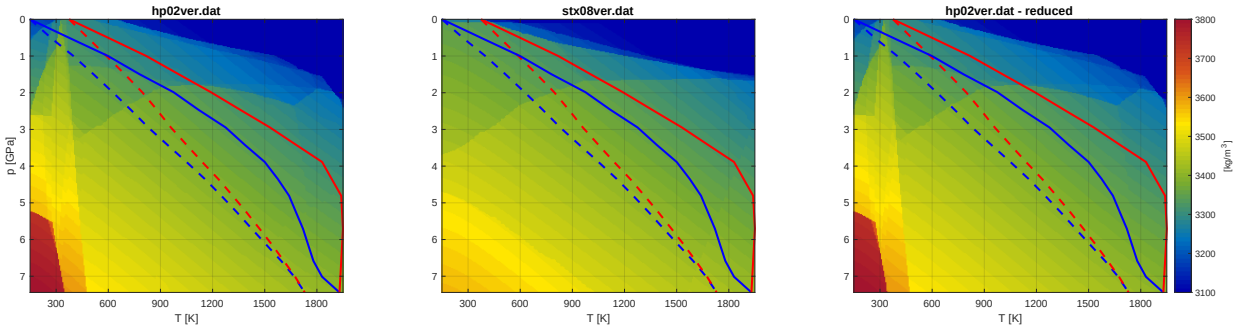

Figure 5.21: Density distribution of the MA model for different inputted solution models. The continuous line indicates the temperature distribution in the hot and cold part of the convective mantle, the dotted lines indicate that of a conductive mantle.

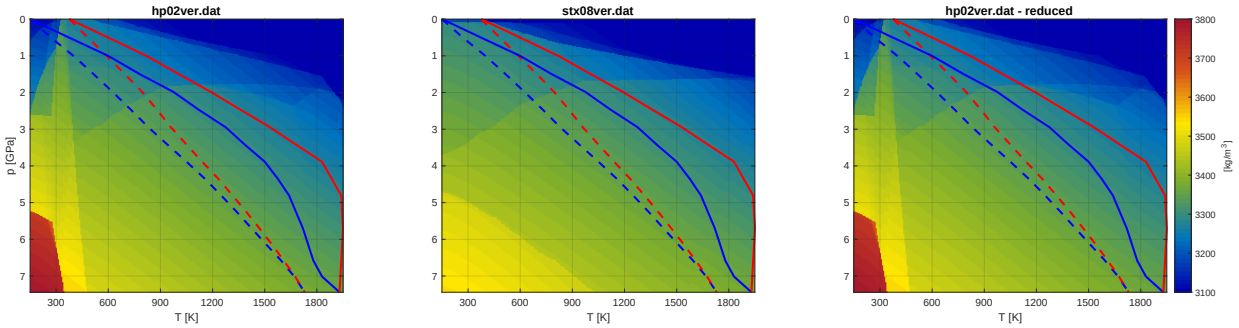

Figure 5.22: Density distribution of the MC model for different inputted solution models. The continuous line indicates the temperature distribution in the hot and cold part of the convective mantle, the dotted lines indicate that of a conductive mantle.

The density models are also compared to the estimations for the average density as performed by Rivoldini et al. (2009). For each of the models, except for the GT model, Rivoldini computed a hot and cold mantle density model. This hot and cold does not refer to a temperature variation within the mantle, but to two possibilities for the temperature of the whole mantle in general. The findings are given in Figure 5.23. The plot shows that the FC mantle model is most dense, followed by TS, MA and MC. This trend is also observed in the computer density models, except for the GT model that is not included in the analysis of Rivoldini et al. (2009). The density data computed with Perple_X are slightly denser than the density values of Rivoldini et al. (2009), but as we are using density differences, this is not a major concern. The temperature difference between the hot and cold mantle in the models of Rivoldini et al. (2009) is roughly 200 K, which is about the temperature difference in the models that are used in this study. The density difference associated with the temperature variation is approximately 10-50 kg/m^3, which is similar to our values.

As the three models comprise very similar density ranges and also density ranges that are considered reasonable within the temperature and pressure bounds, it is concluded that the density differences between the cold and hot profiles can be used to investigate their effect on the mantle.

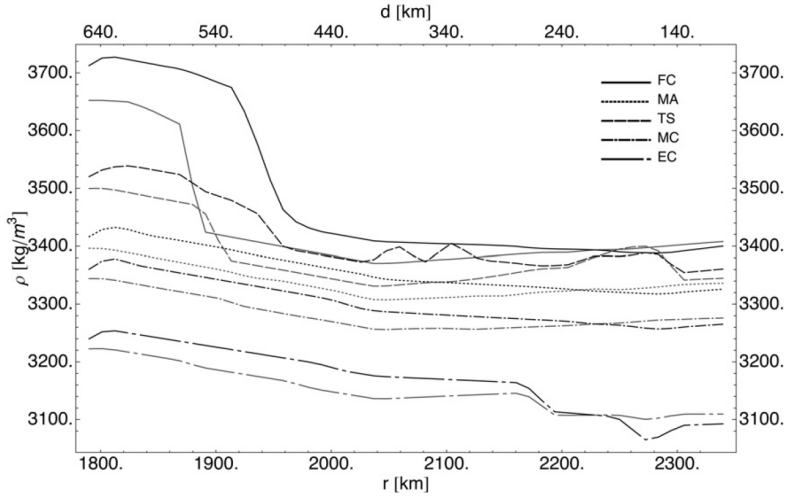

Figure 5.23: The densities calculated by Rivoldini et al. (2009) for the several potential mantle models of Mercury.

5.11. Pressure profile

The pressure throughout a planet is calculated using Equation 4.1, for which the derivation is given in this section. For this derivation a constant density profile throughout the planet is assumed. The result of this derivation is verified with Equation 3.21 from (Lissauer and de Pater, 2013).

The equation for hydrostatic equilibrium is started with, as the internal structure of a planet can be considered as a balance between gravity and pressure forces.

$$P(r) = \int_r^R g_p(r')\rho(r')dr'$$

Filling in Poisson's equation for gravity

$$P(r) = \nabla^2\phi_g(r) = 4\pi \cdot \rho(r) \cdot G$$

and assuming a constant density profile throughout the planet, $\rho(r) = \rho$, yields

$$P(r) = \int_r^R \frac{4\pi G\rho^2 r'}{3} dr'$$

Substituting

$$M = \frac{4\pi R^3}{3} \cdot \rho$$

yields the final equation for the pressure profile throughout a planet

$$P(r) = \frac{3GM^2}{8\pi R^4} - \frac{3GM^2 \cdot r^2}{8\pi R^6} \tag{4.1}$$

This equation is further elaborated upon and used in Section 4.3.1.

5.12. Gravity anomaly due to mantle density profiles

The gravity anomalies associated with the density profiles that incorporate a temperature anomaly, are verified by comparing them with the Bouguer anomaly. The various mantle gravity responses are plotted in Figure 5.24. All gravity fields show a strong signature of the induced density anomaly. The strength of the anomaly varies per model and therefore the visibility of the crustal gravity field varies per model. For example, the density difference in the TS-model is very moderate, resulting in a clear signature of the crust.

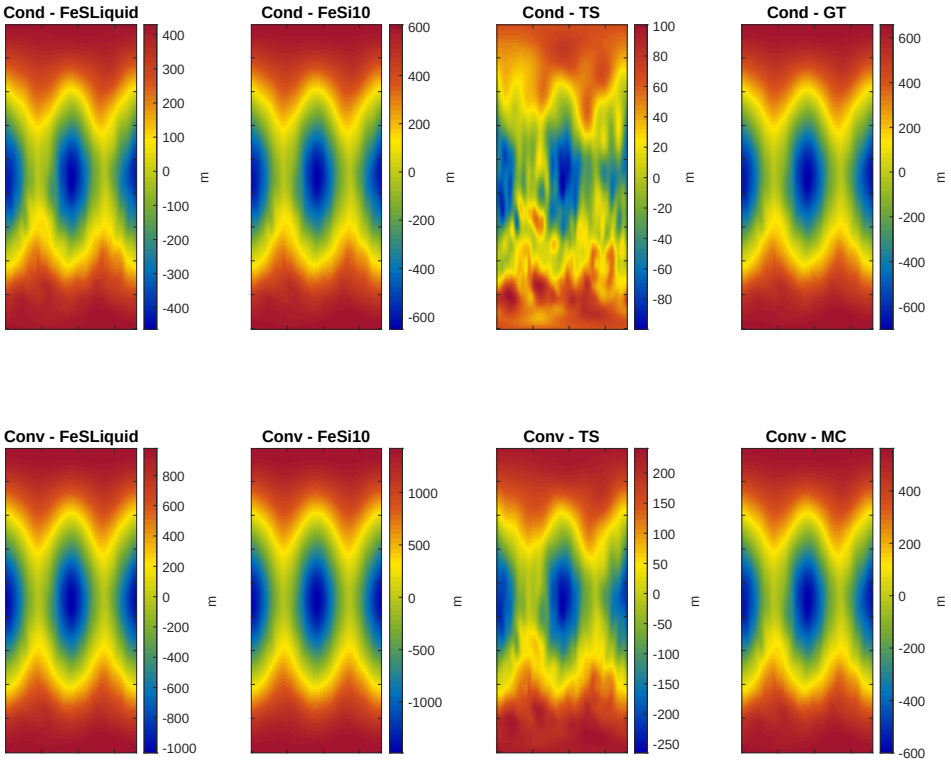

Figure 5.24: The gravity fields that are produced by the temperature anomaly in a conductive or convective mantle model. The temperature anomaly can translate to various density differences, depending on the assumption on the mantle composition. For more information on the mantle models, see Section 4.2.

6

Discussion

In this chapter the conducted research is put into perspective. The limitations of the analysis and considerations during interpretation of the results are laid out.

Crustal model

The crust of Mercury is investigated to preclude that the C_{22}-anomaly that we observe in the gravity field of Mercury, is compensated by the crust. Using the gravity and topography data independently and combinedly, it was preliminary concluded that the crust does likely not account for the long-wavelength gravity field that is observed. An independent study of James et al. (2014) yielded a similar conclusion; although the approach is vastly different and the exact outlook of the deep mantle gravity field is in contrast with the conventional approaches, this model does as well predict deep mass anomalies. This leaves us with a wide variety of crustal models and hence different expected deep mass anomalies, which should all be considered in further investigation.

An assumption in the rest of the investigation is that the crust accounts for all gravity anomalies in the short-wavelength domain (SH>10) and that only long-wavelength gravity anomalies need to be accounted for by the deep mantle. Although this is a proven concept for Earth (Watts, 2001), for Mercury this assumption is disputable. The small size of Mercury and the shallow location of the CMB, make the investigation of Mercury much different. It is questionable whether this SH10 assumption is valid for Mercury, and whether this number should be altered for the case of Mercury. In Figures 5.12 and 5.13 the effect of this assumption is assessed. The short-wavelength features (up to SH30) clearly do not add much gravity to the field, rather they make the outlook more whimsical. This peculiar contour of the gravity field is not characteristic for deep mantle gravity anomalies, and therefore rightfully not considered. The comparison between SH5 and SH10 fields is more arguable. Although the features in the SH5 field are more smooth and of global nature for both options, they are also of a considerable smaller magnitude. Furthermore does the SH5 field display gravity features that are nowhere to be found in the SH10 field, which makes the choice for either one of them challenging. To this observation should be added that the available data is poorly constrained in the southern hemisphere, as the result of a highly eccentric orbit of the MESSENGER satellite. A consideration in line with this, is the strong anomaly around the Caloris basin. The Caloris impact basin is a clear topographic feature, that also shows a strong signature in the gravity field. A relation between the topographic and gravity seems evident, the question however remains where the gravity anomaly would be located radially. If the impacting body would have penetrated through the crust and still be located beneath Caloris basin, SH5 would be more appropriate. If the impact event has triggered a more long-term process in terms of heat and pressure waves, the anomaly is more likely to have penetrated to the deep mantle and hence result in deep mantle anomalies.

If one would only consider the northern hemisphere of Mercury, the SH5 fields would not clearly indicate two gravity bulges on the equator, rather one would observe a gravity high along the whole equator. As a clearer sign of LLSVPs is observed in the SH10 field than in the SH5 field, the SH10 field is rightfully selected to be more appropriate to consider in further analysis.

Volcanism

Torsvik et al. (2006) discovered that LIPs and hotspot volcanism relate to the LLSVPs. These forms of volcanism can not be related to plate tectonics, and therefore a different origin for them is sought. It is proved that these volcanic features were at the time of their formation almost all located radially on top of the edges of the LLSVPs. Their location is not entirely unrelated to mantle convection, i.e. without mantle convection the mantle upwellings that resulted in the LIPS and hotspots would not have existed (Tan et al., 2002). The edges of the LLSVPs are detected in seismic data as the location where the shear-wave velocity gradient is steepest (Torsvik et al., 2006). The constructed LLSVP outlines *roughly* correspond to the geoid highs in Earth (Trønnes, 2010; Anderson, 1982), hence we can perform an equivalent analysis for the volcanic features on Mercury and the hypothesised LLSVPs. The edges of the Hermeoid highs are thus not necessarily the actual edges of the LLSVPs, however they are the best approximation currently available.

The smooth plains on Mercury are compared to the LIPs on Earth and the pyroclastic vents observed on Mercury are taken as the equivalent of Earth's hotspot volcanism. Although there is not yet any sign of mantle convection in Mercury, which is a prerequisite for the LIPs and hotspots on Earth, it is worthwhile to investigate the hypothetical equivalence. This hypothesis is of course arguable, as volcanism can show as various signatures on a planet's surface and be caused by various mechanisms (Lissauer and de Pater, 2013). Again a limitation in the data on Mercury is the incomplete coverage of the planet, and on top of that the accuracy of the data. Although the currently mapped smooth plains and pyroclastic vents seems to be of a global coverage, the poor coverage might hide more of these features. Brož et al. (2018) confirmed this by investigating why kilometre-sized pyroclastic deposits are not observed on Mercury, and concluded that this is the results of the quality of the data. Another possibility could be that volcanic activity in the planet or impact events of a later stage have vanished the signs of pyroclastic activity or less likely smooth plains over time, inhibiting us to generate a full overview.

Goudge et al. (2014) observed a strong relation between pyroclastic vents and impact basin. 90% of the pyroclastic vents is located near the rim or in an impact basin, pointing towards a relation between the two. Crustal weakening at impact locations could explain why specifically these locations show pyroclastic activity. The global contraction of Mercury could have induced such a large crustal stress state that mantle upwellings can not penetrate through the crust in general, but only at weakened locations. In case the mantle upwellings would relate to the edges of the LLSVPs, one would hypothesise to see the pyroclastic vents only near or in impact basins that are located radially above the (edges of the) LLSVPs. In case pyroclastic vents are also located at impact basins that do not lie above LLSVPs, the relation between pyroclastic vents and LLSVPs is either obsolete or of a more complicated nature. A more complete map of the pyroclastic vents (and possibly the smooth plains) could shed light on this hypothesis, and could possibly be used to determine the location of LLSVPs on the CMB.

Conventional LLSVPs

With the constructed crustal models and their resulting residual gravity field, it is investigated what the size and density of deep mantle mass anomalies have to be in order to match with these residual fields. The analysis showed that LLSVPs with characteristics similar to the Earth are most viable. Higher density variations require a very thin layer, and vice versa very low density difference require LLSVPs sometimes thicker than the actual mantle. One shortcoming of this approach was that thickness and density variations were not considered simultaneously. One could assume that the combination of density and thickness variations could allow for more realistic scenarios, especially in the most extreme cases.

The model of James et al. (2014) did not allow for fitting of the full gravity field. It was identified that this non-convergence was caused by the inclusion of short-wavelength gravity anomalies that still remain in the gravity field after subtraction of the crustal model. It was considered to be beyond the scope of this thesis research to alter the James crustal model such that it would also compensate short-wavelength gravity anomalies. It remains for future research to assess the required adaptations to James' crustal model in order to match full gravity field.

The method of fitting assumes a linear relation between mass and gravity, i.e. at the location of a negative gravity anomaly mass is subtracted at a point radially downwards and vice versa. This method works well at

this stage, requiring a fit within bounds of 10 mGal and considering the available accuracy of the data. It is however noticed that as the gravity anomalies that need to be fitted become smaller, the more computational effort this requires. In some cases, the algorithm is not able to reach a fit within 10 mGal bounds and gets stuck in the range of 10-20 mGal. As these remaining anomalies are of very small size, they are not expected to influence the results in a clearly noticeable manner. Improvements to the fitting algorithm, to incorporate the spherical shape of a planet and the different radial locations where mass increments are added, could allow for easier and less computationally intensive fits. Also the development of a fitting procedure that sizes the mass increments not only using the input of the gravity residual radially located upwards, but also considering the surrounding gravity field, could aid in mitigating these minor remaining residual of several mGals.

Temperature anomaly

The temperature anomaly modelled by Tosi et al. (2015) is in this study subject to further analysis. Tosi et al. (2015) modelled a convective and conductive scenario for the mantle of Mercury, where the peculiar insolation pattern of Mercury induced a temperature anomaly on the surface that propagated through the mantle to the CMB. They use this temperature profile to assess the effect on elastic thickness and with that the effect on the degree-2 and -4 Hermeoid. Interesting about this hypothesis is the similarly proposed thermal cause for the LLSVPs in Earth. Subduction of MORB material could penetrate into the deep mantle (Trønnes, 2010; Garnero et al., 2016), and induce, apart from a chemical discontinuity, also a thermal anomaly, leading to the formation of LLSVPs (Hirose et al., 2006). Tosi et al. (2015) found that the temperature anomaly could account for the even-degree anomalies, but concluded that a different reasoning needed to be found to explain the odd-degree anomalies. The variation in the location of the core-mantle boundary was only several tens of meters, indicating the the inclusion of flexural response of the crust and dynamic topography has a large influence on the final results.

In this study, the temperature profiles, or to be precise the differences between the temperature profiles, are used to calculate the differences in the density profiles. These density profiles are then assessed for their effect on the gravity field. The crustal models as introduced before are used, rather than the flexure model used by Tosi et al. (2015). Furthermore, this analysis includes all spherical harmonic degrees up to 10 (C_0,C_1 and C_{20} are discarded), and not only degree 2 and -4. The fact that in this study density differences are considered, rather than absolute values for the density, make the analysis more widely applicable, i.e. to various mantle compositions that would induce a similar density difference.

The modelled density differences are rather extreme in the sense that they cover large density difference throughout the whole mantle. The temperature difference spans the whole mantle, and in some mantle composition this leads to a major density contrast. It is unproven that the insolation pattern that Mercury is currently facing has sustained over a long time. The peculiar insolation pattern is a result of the 3:2 orbital resonance that Mercury is captured in, but it is unknown when this capture took place. Therefore it could well be that the temperature anomaly on the surface has not yet or differently propagated in the mantle than Tosi et al. (2015) modelled. One of the interesting characteristics in the Earth is the seemingly longevity of the LLSVPs, and with this statement this claim for Mercury is undermined.

On top of that comes the veracity of the modelled mantle compositions. The density difference in the FeS and FeSi-layers are largest, but it is highly unlikely that the whole mantle composition constitutes of one of these alloys. A more realistic scenario would be the combination of one of the other modelled mantle composition with a basal layer of FeS- or FeSi near the CMB. The complication would then be that the basal layer experiences merely any temperature differences, hence barely any density difference either. Furthermore does the calculation of the density difference in an FeS/FeSi composition not include the effect of pressure. This assumption is justified by the fact that the two points between which the density difference is computed, are on a line of equal pressure. Therefore one can assume no pressure difference, and as the thermal expansion coefficients are experimentally calculated for equal-pressure situations, this assumption can be justified. In reality it is however not likely that there is no pressure difference between two points at equal depth, and the effect of pressure should be incorporated. For the mantle models analysed by Perple_X the pressure profile is a rough approximation. The complication arising with the calculation of the density differences computed with Perple_X is the lack of knowledge and experience of the author in this field of expertise. The mantle com-

positions are taken from literature and therefore considered to be representative, however the truthfulness of the exact density differences remain unknown, also given the other complications in the determination of the temperature and pressure profiles. Furthermore, some of these models are aged, originating from the pre-MESSENGER era. This is however accepted, as, apart from the information that the crust of Mercury contains many volatiles and few FeO content, MESSENGER did not yield much more information about the mantle composition (Nittler et al., 2018). Another important consideration is the unknown cause for the thin mantle of Mercury. Suggested causes for the thin mantle are a slightly more effective aerodynamic removal process of silicate than of iron (Weidenschilling, 1978), vaporisation of the mantle by the immense heat coming from the solar nebula (Cameron, 1985) or an hit-and-run scenario, where the mantle of Mercury was ripped off (Asphaug and Reufer, 2014). These events would likely all have an effect on the present mantle composition of Mercury. More understanding of the formation of Mercury could aid in the determination of the mantle composition.

Core-mantle boundary fitting

Following the results of the temperature anomaly it is investigated how CMB topography could account for observed and modelled gravity anomalies. As a benchmark the required CMB topography is calculated that would be required in a density anomaly free mantle. This calculation is followed by numerically simulating the density differences that result from a temperature anomaly (Figure 5.24), and the consequently needed CMB topography (Figure 4.16). Although the introduced gravity anomalies are relatively large, ranging from $\pm$100 to $\pm$1200 mGal, the accompanying increase in the CMB topography is of a lesser magnitude.

According to James et al. (2014), the core-mantle boundary topography can be related directly to the surface topography, in case of the simultaneously existence of a basal layer. The interaction of instantaneous radial velocities in the mantle can interact in such a manner that surface topography arises. CMB topography of several kilometres could induce 1 km of topography. Given the observed topography on Mercury, this would translate to CMB variations of 10-15 km which would well match the results in this thesis.

This observation might support the possibility to use surface topography to determine the outlook of the LLSVPs. If topography (partially) relates to CMB variations, a prerequisite for this hypothesis is the existence of mantle convection, which is not proven yet to exist on Mercury.

Future outlook

From the discussion of these results it can be concluded that a lot of questions remain concerning the deep mantle structure of Mercury. The ambiguity in the incompleteness of the crustal model, and then mainly the translation to the deep mantle gravity field, hinders the progress in our understanding. The uncertainty in the crustal model of Mercury inhibits to draw any conclusions on the relation between volcanism and LLSVPs, which can be very valuable in the future determination of the location of deep mass anomalies. The topography can be likewise. In future analysis, the effect of the potential temperature anomaly in Mercury is highly interesting, because of the interaction it would have with the CMB and the crust.

Fortunately, BepiColombo is on its way to reveal more information about the mysteries of Mercury and shed light on the many questions. Improved topography data, compositional constraints and a more global gravity field would highly aid in the explanation of the C_{22} anomaly in Mercury. Seismic data would be the ultimate data source to constrain the interior of Mercury, however the set-up of a global seismic network on Mercury is a distant dream. The possibility for LLSVPs on Mars has also already suggested (Burke et al., 2012). Considering the seismometer that has currently been deployed on Mars, one might want to shift the focus to Mars in the progress of understanding deep mantle structures, although Mars does not have the advantage of a shallow location of the CMB.

7

Conclusion & Recommendations

In this research project a preliminary investigation is conducted to identify deep mantle structures in Mercury equivalent to the LLSVPs that are observed in the deep mantle of Earth. By combining the observations and considerations from this study, a preliminary answer to the research question could be formulated:

Could density anomalies in the deep mantle structure of Mercury, similar to the Large Low Shear-Velocity Provinces in Earth, account for the observed long-wavelength gravity field of Mercury?

The answer to this question is that it is definitely possible, however the question remains how likely their existence is. The analysis of Mercury's topography and gravity shows that the crust can likely not account for the full gravity field. Many short-wavelength features can be filtered out, but long-wavelength features are less likely explained by the crust. It is thus indeed likely that there are long-wavelength gravity features that are caused by the structure of the deep mantle and/or core. Throughout the various crustal models that are constructed, quite some variations are identified. The Airy model leaves a residual model that is much like the unadjusted free-air anomaly. The inversion of the Bouguer anomaly leaves a smaller anomaly that is more spread around the whole equator. The crustal model constructed by James et al. (2014) shifts the observed deep mantle anomalies by 90^{o} and enlarges them. The selection of the crustal model is thus determinant for the deep mantle structure and for the sake of completeness all crustal models are continued with.

For the rest of this section, deep mantle mass anomalies are divided in two parts: 1) deep mantle structures and 2) core-mantle boundary topography. Investigation of the size and density of the deep mantle structures in Mercury yielded that deep mantle structures can be present that have equivalent density and thickness characteristics as the LLSVPs in Earth. Because of the shallower location of the LLSVPs the density contrast is smaller in absolute magnitude, however percentage wise it is comparable. The size of the deep mantle structures is comparable after scaling it to the planets' core, mantle and total radii. The structures in Mercury have a rather whimsical three-dimensional shape, that shows the same contours as the gravity field that it is fitted to, which is in line with the LLSVPs in Earth (Cottaar and Lekic, 2016). The mean location of the CMB in Mercury is not narrowly constrained (within 400 - 440 km depth (Margot et al., 2018)), but this showed to be of second-order importance in the determination of the size and density difference in deep mantle mass anomalies.

It is also investigated how CMB topography can account for the observed gravity field. It is concluded that the high core-mantle density contrast allows the CMB topography of small size in comparison with the size of the previously modelled LLSVPs, however that in comparison with the predicted CMB variations in Earth (~12 km (Soldati et al., 2013)) the fluctuation in Mercury would be rather large (~1 - 17 km depending on selected crustal model and core-mantle density contrast). It is questionable whether such a whimsical shape of the CMB is likely, given that high density contrasts are not likely to sustain over long periods of time, especially not when these are only small features. A combination between CMB variations and anomalies in the mantle or crust might be more likely.

The temperature anomaly that might be present in Mercury adds another complication to this analysis. It is not known whether the temperature difference on the surface has indeed propagated through the mantle to the CMB, and to what extent. The temperature anomaly is located such that it causes an absence of mass in high-gravity regions, and an excess of mass at locations where low gravity is observed. Although this might seem contradictory, Tosi et al. (2015) suggested that the alleviation on the CMB by the lack of mass allows the CMB to rise up. Vice versa, in cold, high density regions the CMB is suppressed. This would result in an a-spherical core, inducing gravity anomalies that counteract the density contrast and result in observed gravity anomalies of the magnitude and sign that we observe now. This temperature anomaly is thus highly interesting for its interaction with the CMB, but requires more constraints to quantify the effect further. For the analysis of the gravity field the temperature differences are of main importance, as the consequential density differences are determinant in the magnitude of gravity anomalies. More knowledge on the exact mantle composition would thus not yield a large improvement in this research, since the density differences are of main importance, rather than the absolute value of the density. The suggestion of a phase transition in the mantle of Mercury inducing a steep density contrast has not been confirmed within the mantle compositions that were analysed. Given the uncertainty in the magnitude of the temperature anomaly and in mantle composition, it is not possible to draw any conclusions from this.

Given the large number of unknowns regarding the interior of Mercury, to be able to draw some more definitive conclusions about the deep mantle, it is needed to fix the crustal model. The following conclusions can be drawn if we assume the existence of a certain level of crustal compensation:

- An Airy-Heiskanen compensated crust would yield a gravity residual resulting from the deep mantle that shows contours much like the free-air gravity anomaly. The investigation of the size and density of deep mass anomalies required to counteract this anomaly reveals that Earth-like parameters would be feasible. Given the magnitude of the density contrast, it seems most probable that these anomalies result either from an irregular shape of a high-density basal layer or from a phase transition. At the shallow location of the CMB of Mercury, where pressure and temperature are still relatively low, it is unlikely that a major density contrast can be achieved otherwise. A temperature anomaly as proposed by Tosi et al. (2015) would complicate the analysis, as even larger gravity anomalies in Mercury would then have to be explained.
- The James crustal model has a large remaining residual, that fits well with the density contrast that is induced by a temperature anomaly in the mantle. With relatively minor variations in the location of the CMB, the combination of the James crustal model and a mantle model of laterally varying density can be matched to the observed gravity field. Another possibility would be a phase transition, however it is questionable whether at the temperature and pressure conditions in Mercury such a large density increase is reasonable.
- The residual of the Bouguer crustal model is smallest in size, and shows an equatorial belt of mass. It is therefore disputable whether this residual indicates actual LLSVPs, or rather a more symmetric concentration of mass along the equator in the form of for example an a-spherical core.

In concert of these above stated explanations for the observed gravity field, CMB topography is also a likely cause for the observation. Only minor variations in the location of the CMB can already compensate large gravity anomalies, due to the high crust-mantle density contrasts that are assumed. Also in the case of the propagation of the surface temperature anomaly through the mantle, the induced density anomaly can be counteracted.

The comparison between volcanism on Earth in relation to the LLSVPs and volcanism on Mercury in relation to deep mantle anomalies reveals no new insights. The smooth plains on Mercury concentrate on the northern hemisphere and not specifically near the geoid highs. The suggested relation between impact basins and pyroclastic vents by Goudge et al. (2014) might be more complex than they suggest and pyroclastic vents might have an additional relation with the geoid highs. However to support this hypothesis a map of the pyroclastic vents of a more global coverage is required. Also, a limitation in this comparison is the lack of seismic data for Mercury that allows us to draw the edges of the LLSVPs at the edges of the geoid highs, rather than at the location of steepest shear wave velocity. Additional to this is our lack of knowledge about movement of the crust with respect to the CMB. This is also the case for Earth and would complicate our study.

Recommendations

From the conducted research some recommendations for improvements of or additions to the current research follow, listed below.

- A major help in the research on Mercury would be to have **better coverage of the southern hemisphere**. Deep mantle anomalies as are currently investigated are of a global scale, and the lack of data on the southern hemisphere inhibits our understanding of Mercury as a whole. Improvements in the analysis on volcanism will also be achieved by more global coverage of Mercury, allowing for a better quantification of the relation between high-Hermeoid and pyroclastic vents.

- With or without this extra data, better understanding of crustal formation, compensation and interaction with the rest of the planet could lead to an **improved crustal model**. It is noticed that the crustal model largely determines the outlook of the deep mantle field and that this residual is determinant in the size and density of the deep mantle mass anomalies. Better understanding of the role of the crust in the gravity field would largely aid in our understanding of the deep mantle as well. A possibility for improving the crustal model would be to consider regional isostasy: flexural rigidity of the crust. This was slightly touched upon in Section 2.3 but left as is because of its immaturity.

  Quantification of what **spherical harmonic degrees** likely result from the **deep mantle**, and what spherical harmonic degrees more likely relate to for example impact basins like Caloris, would give a better view on the interior of Mercury. A comparison with the mass concentrations observed on the Moon, for which the origin has been researched intensively (Melosh et al., 2013), could for example shed more light on the crust of Mercury. The normal modes theory discussed by Koelemeijer et al. (2017) could also aid in this. Quantification of the relevant spherical harmonic wavelengths associated with the LLSVPs in Earth, and consequently translating these to the spherical harmonic degrees in the gravity field of Mercury that correspond to similar wavelengths, would also be a valuable improvement. This analysis would then most optimally also consider the radial location of the LLSVPs, i.e. the differences between the radial location of the CMBs.

- Regarding the deep mantle:

  - The **temperature anomaly** in Mercury has only preliminary been investigated. If this thermal anomaly indeed plays such a major role in the mantle (and crust) and thereby in the gravity field, it is worthwhile to investigate its existence, magnitude and effects further. Also the consequential interaction between mantle and core is of interest in this research, as minor CMB variations have proven to be of major impact.

  - Advances in the current **fitting algorithm** could allow for tighter and less computationally expensive fits with the Hermeoid. The current method subtracts and adds mass increments according to the observed residual. However, in this process it does not take into account the differences in the radial location of the mass increments, nor does it consider the spherical shape of the planet and the consequential varying volume of the mass increment. Furthermore, assumes the fitting algorithm that a gravity signature is only influenced by the mass located radially beneath it, which is strictly not the case. (Please note: the fitting algorithm makes this assumption only in the process of sizing the density increments, the computation of the gravity field does include the effect of the whole body.) A gravity signature at a specific point is influenced by the mass of the whole planet, however the nearest masses have the largest influence. The fitting process works therefore well for larger anomalies, as these are mainly influenced by large masses located nearby. But when one requires to fit the small anomalies, an adaptation in the sizing of the density increments is required to converge to a tight match with the Hermeoid. A possibility is to use Green's filters as explained by Pawlowski (1994).

  - In this study either density variations or thickness variations are considered, but the two are not assessed simultaneously. **Concurrent consideration of size and density** variations would highly complicate the investigation as it will broaden the search space. This is considered to be out of the scope of this study. To successfully implement this, a well-thought out procedure and parameter range selection need to be set up.

A

Additional Results

A.1. CMB @ 440km

density fitting [kg/m^3]	Airy		Bouguer		James	
	min	max	min	max	min	max
t = 10 km	-261	356	-321	259	-377	241
50	-115	185	-89	69	-321	187
100	-52	82	-42	32	-152	91
150	-32	50	-27	20	-94	55
200	-23	35	-16	13	-62	36
300	-20	31	-14	11	-56	32

thickness fitting [km]	Airy		Bouguer		James	
	min	max	min	max	min	max
ρ = 50 kg/m^3	-100	133	-79	56	-407	147
80	-60	87	-48	35	-226	102
100	-45	67	-36	27	-156	80
200	-23	35	-17	13	-67	37
400	-11	17	-8	7	-33	19
1000	-4	7	-3	3	-13	7

Table A.1: Minimum and maximum values of the density (top) and thickness (bottom) of the basal layer after the fitting process for the CMB-layer located at 400 km depth, in addition to the boxplots in Figures A.1 and A.2. Light grey indicates non-convergence.

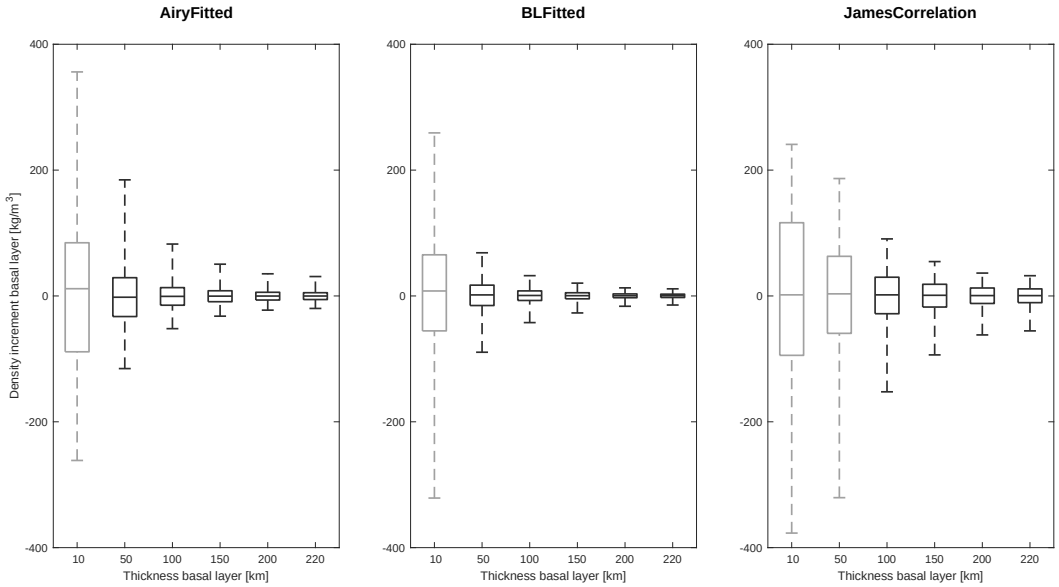

Figure A.1: Results of the density fitting process for a model with CMB at 400 km (instead of 440 km). Light grey boxplots indicate no convergence (within the preset number of iterations). Remaining residuals: Airy-10: ±80m, Bouguer-10:±25m, James-10:±195m, James-50:±20m.

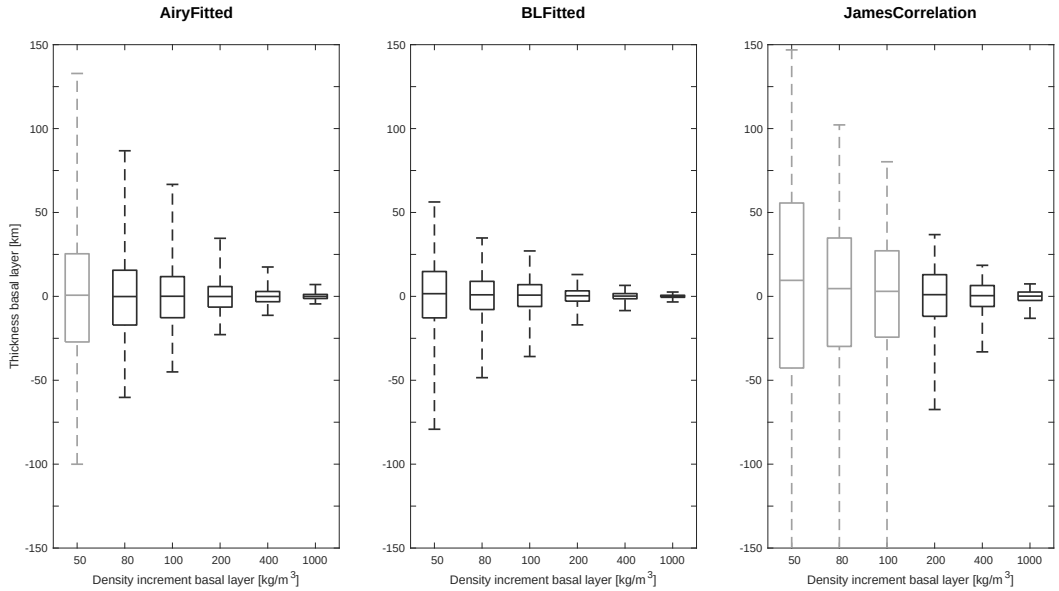

Figure A.2: Results of the thickness fitting process for a model with CMB at 400 km (instead of 440 km). Light grey boxplots indicate no convergence (within the preset number of iterations). The reason for non-convergence in all cases is a too thick layer, i.e. a layer that penetrates into the core. Initial thickness parameters: 100. Average thickness parameters: Average thickness parameters: Airy [87,92,94,97,99,99], Bouguer [103,102,102,101,100,100] and James [122,114,111,105,103,101].

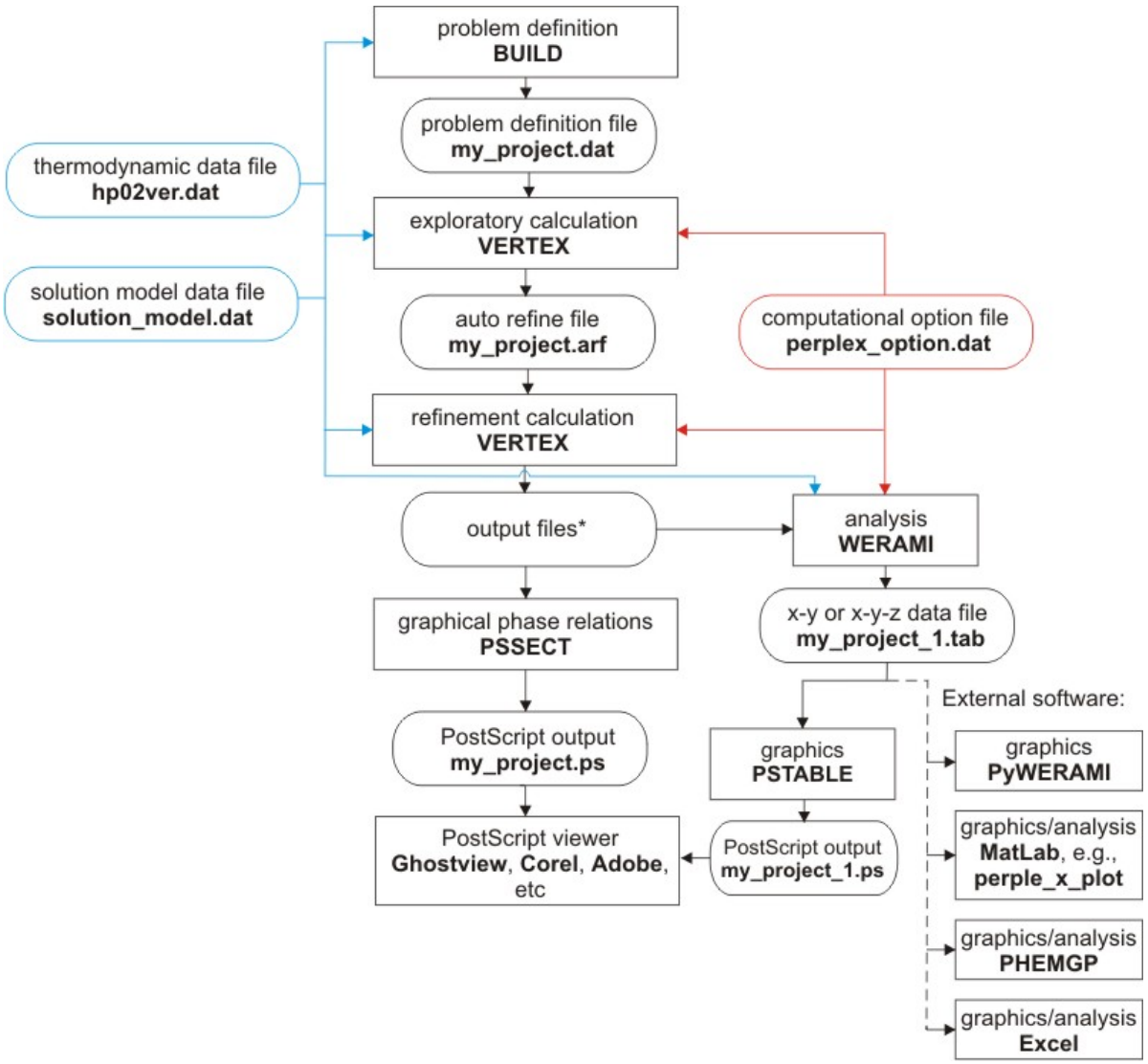

Figure A.3: Flow-chart of the Perple_X software from `http://www.perplex.ethz.ch/images/perplex_666_section_flow_chart.jpg`

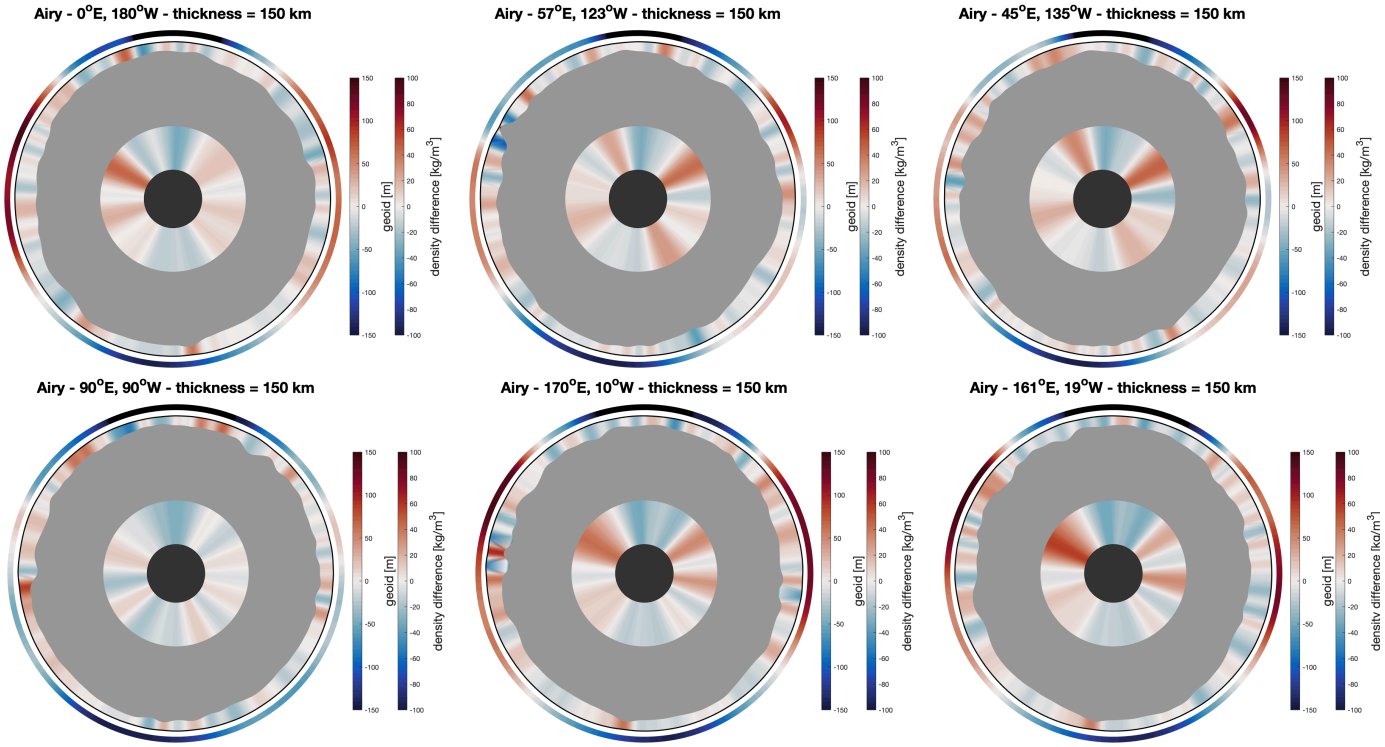

Figure A.4: Cross sections of inner Mercury after fitting of the density of the basal layer for an Airy model.

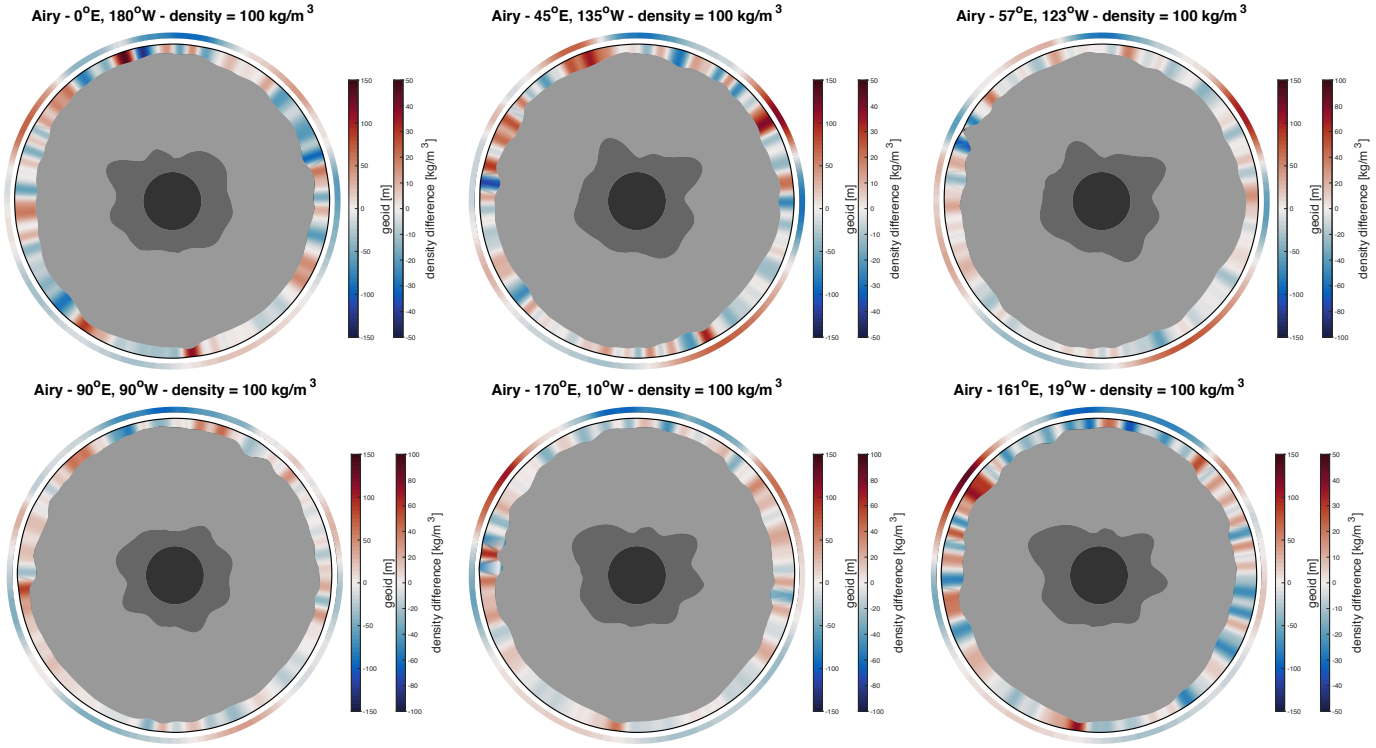

Figure A.5: Cross sections of inner Mercury after fitting of the density of the basal layer for a Bouguer model.

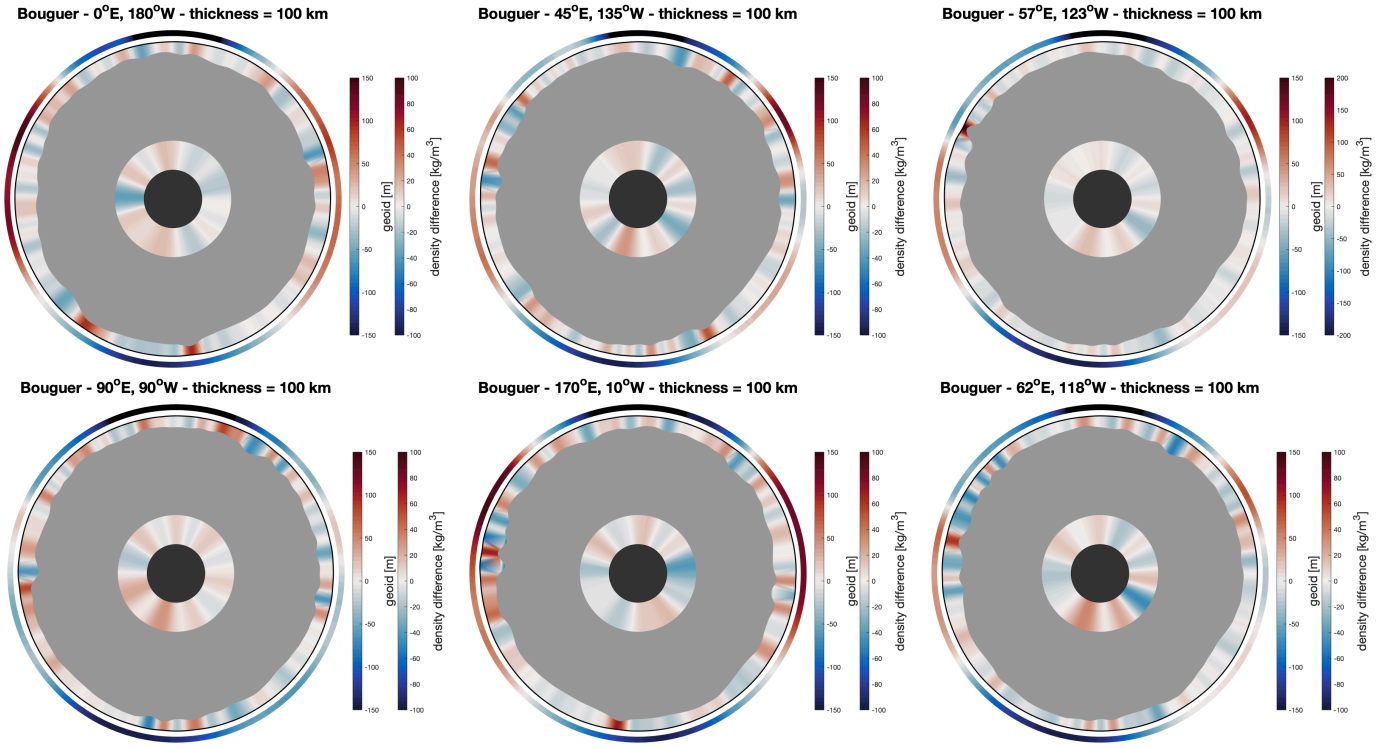

Figure A.6: Cross sections of inner Mercury after fitting of the density of the basal layer for a James model.

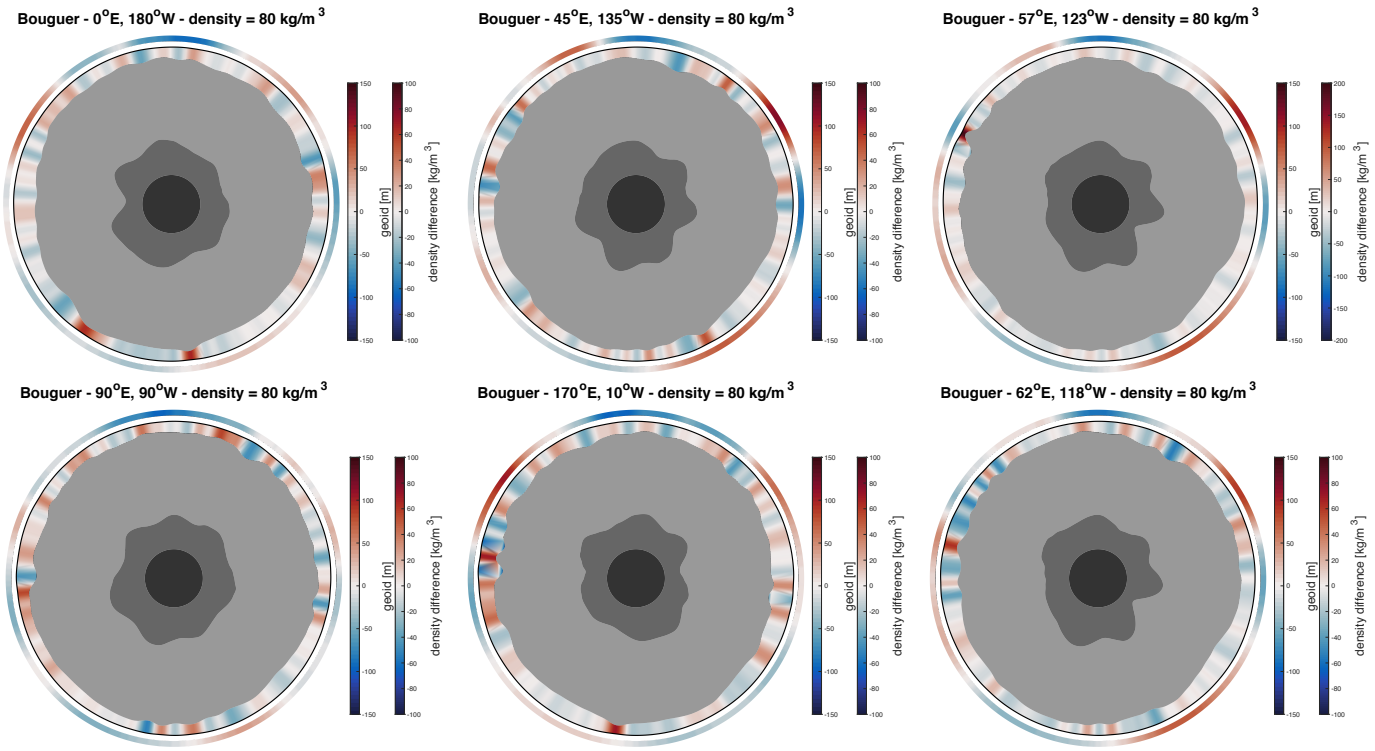

Figure A.7: Cross sections of inner Mercury after fitting of the thickness of the basal layer for an Airy model.

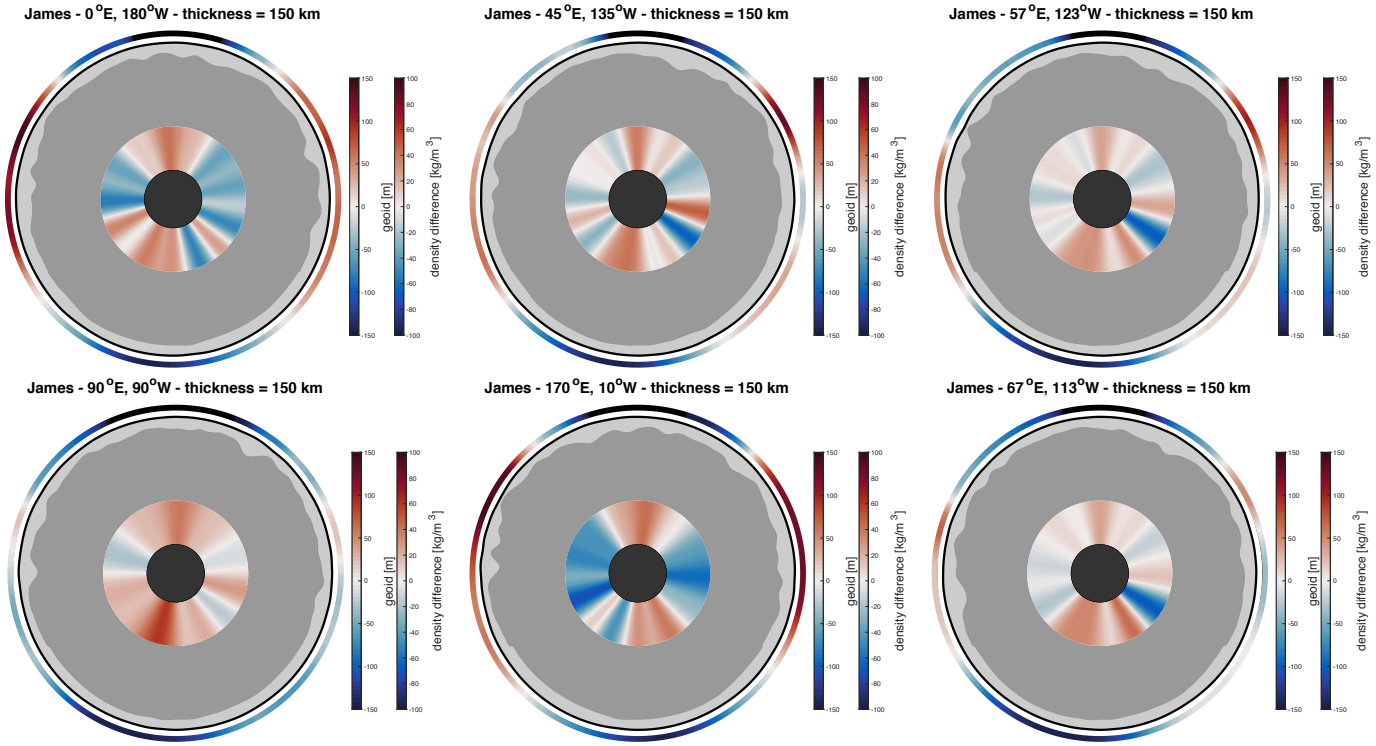

Figure A.8: Cross sections of inner Mercury after fitting of the thickness of the basal layer for a Bouguer model.

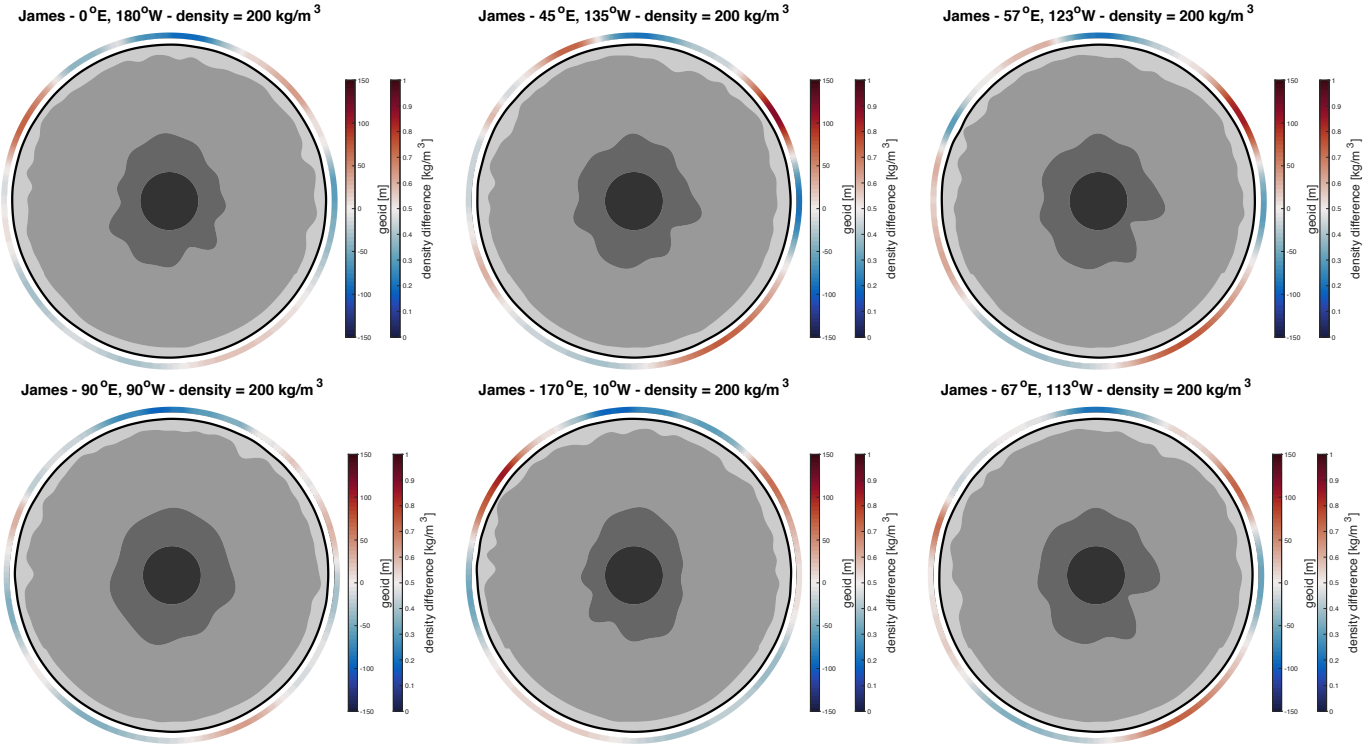

Figure A.9: Cross sections of inner Mercury after fitting of the thickness of the basal layer for a James model.

B

Additional data

B.1. Bouguer Anomaly

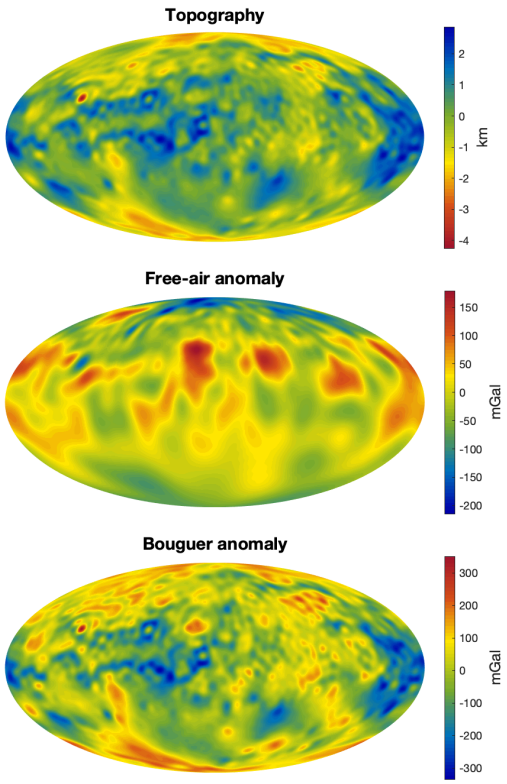

Figure B.1: (top) The topographic map of Mercury, computed from spherical harmonic degree 0 - 50, along with the (middle) observed gravity anomalies over Mercury, computed from spherical harmonic degree 0 - 50 with C_{20} = 0 and (bottom) the resulting Bouguer anomaly using a crustal density of 2800 kg/m^3. Please carefully consider the colourbar ranges that are used. (In all plots 0-level is indicated with the same colour. The colourbar for both gravity plots are set to the same range to ease comparison. The topography colourbar is of opposite colours w.r.t. the colourbars of the gravity plots.)

B.2. Crustal thickness plots

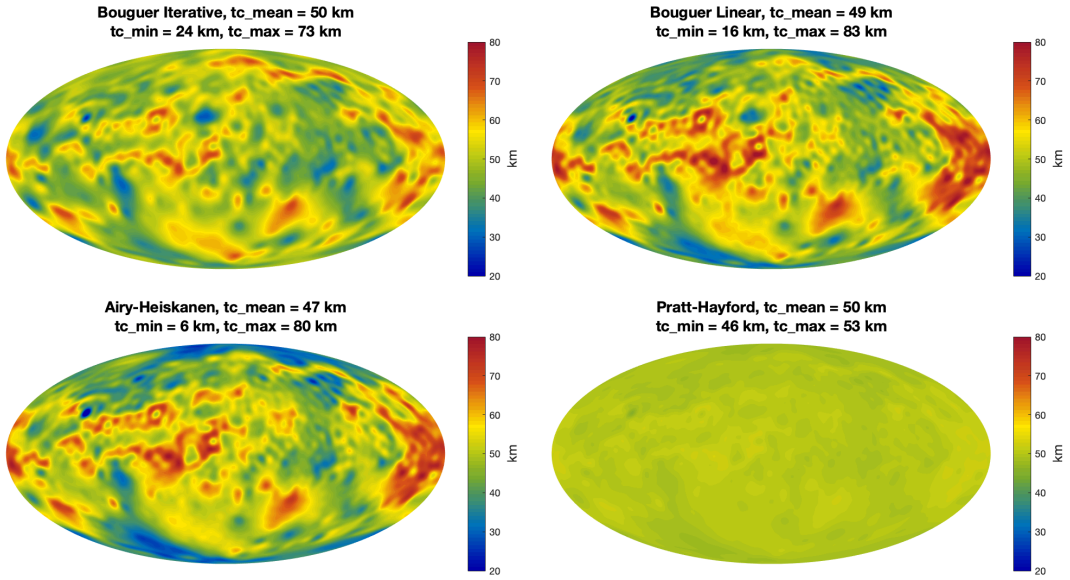

Figure B.2: Crustal thickness plots of Mercury resulting from various applied mathematical theories.

B.3. Flow-chart diagram crustal fitting process

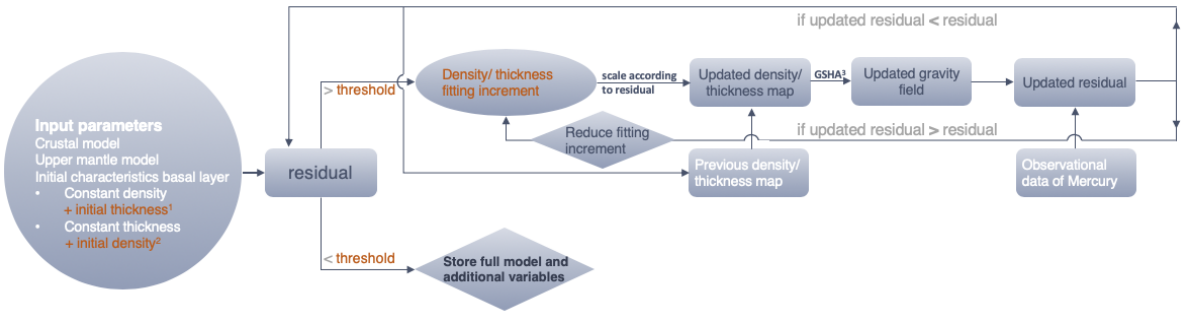

Figure B.3: Graphical representation of the crustal fitting algorithm. Orange text indicated variable input parameters (please also see Section 5.8). This diagram is a simpler version of Figure 4.1. The simplification is in the manual adjustment of the fitting increment, instead of an automated adjustment.
[1] Is only a variable input parameter when the layer *thickness* is fitted. [2] Is only a variable input parameter when the layer *density* is fitted.
[3] GSHA = Global Spherical Harmonic Analysis (software package obtained from Root et al. (2016)).

B.4. Location data pyroclastic vents

Name	Latitude [^{o}]	Longitude [^{o}]	Area [km^2]	Radius [km]	Size class	Age
Gibran	35.8	63.8	19466	71	5	Tolstojan
RS-05	24.3	-179	10414	54	5	Caloris
Hemingway	17.6	-2.7	8920	54	5	Calorian
Hesiod a	-57.2	-31.7	4950	30	5	Tolstojan
RS-03	22.3	146.2	4063	24	5	Caloris
RS-02	58.8	160.6	3951	23	5	Mansurian
Lermontov N	15.8	-48.2	3806	33	5	Mansurian
Raphael	-21	-74.4	3240	30	5	Pre-Tolstojan
Lermontov S	15.1	-49.1	3174	31	5	Mansurian
To Ngoc Van	52.6	-111.8	2924	22	5	Calorian
Praxiteles NE	26.9	-59.1	2594	26	5	Calorian
Scarlatti	41.3	-10.7	2490	22	5	Tolstojan
Hesiod c	-53.2	-30.9	2233	21	5	Calorian
Hesiod b	-55	-30	2079	19	5	Pre-Tolstojan
NE Rachmaninoff	35.8	-111.3	1852	22	5	n/a
Geddes	27.2	-29.5	1654	21	5	Calorian
Melville	26.2	59.8	1389	20	5	Mansurian
Mistral SE	4.2	-54.2	1245	19	5	Tolstojan
Praxiteles SW	26	-60.3	1210	18	5	Calorian
RS-04b	16.7	156.9	1196	20	5	Caloris
RS-04a	14.1	159.2	32	19	5	Caloris
NE Derzhavin	48.4	-33.7	1111	15	5	Tolstojan
RS-04c	14.2	162.1	1048	19	5	Caloris
Hesiod e	-51.5	-27.9	1021	14	5	Calorian
RS-01	-13.3	144.9	1008	18	5	Mansurian
Unnamed crater 1	22	-67.5	921	17	4	Calorian
RS-04d	15	164	911	17	4	Caloris
RS-03 SW	21.7	145.4	875	19	4	Caloris
Glinka	14.9	-112.4	946	16	4	Tolstojan
Rachmaninoff SE	26.2	-4.2	746	17	4	Mansurian
RS-04e	15.4	165.3	502	12	4	Caloris
Hesiod d	-52.2	-28.6	453	9	4	n/a
Mistral NW	5.4	-55.2	421	11	4	Mansurian
Beckett	-40	111.2	408	10	4	Calorian
RS-03 SE	19.4	150.2	317	7	3	Caloris
Unnamed crater 4	0.5	-161.9				Tolstojan
Picasso	3.45	50.4				Tolstojan
Unnamed crater 5a	-52.1	139.4				Calorian
Unnamed crater 5b	-55.1	142.5				n/a
Unnamed crater 5c	-56.2	143.8				Calorian
Kipling N	-18.45	72.03	936		4	Tolstojan
Kipling W	-19.21	71.43	1109		5	Tolstojan
Kipling S	-21.16	72.4	1956		5	Calorian
N Rachmaninoff	36.1	57.3	4273		5	n/a
Tolstoj E	-16.7	-161.7	4525		5	pre-Tolstojan
Tolstoje S	-21.13	-163.02	524		4	n/a
Tolstoj SE	-19.88	-161.14	512		4	Calorian
Tyagaraja	3.75	-148.88	498		4	Mansurian
Unnamed crater	6	58.8	-32.9	1352	5	Mansurian
Unnamed crater	7	32.4	88.2	1383	5	Tolstojan
Unnamed crater	8	-45.04	167.6	484	4	Mansurian

Table B.1: Overview of the locations of the identified pyroclastic vents. Gibran up to and including Kipling N are identified by Kerber et al. (2011), Kipling W up to and including the last Unnamed crater are identified Goudge et al. (2014). All data on age is from Goudge et al. (2014). Data retrieved via personal communication.

Bibliography

Anderson, D. L. (1982). Hotspots, polar wander, Mesozoic convection and the geoid. *Nature*, 297(5865):391–393.

Ash, M. E., Shapiro, I. I., and Smith, W. B. (1971). The System of Planetary Masses. *Science*, 174(4009):551–556.

Asphaug, E. and Reufer, A. (2014). Mercury and other iron-rich planetary bodies as relics of inefficient accretion. *Nature Geoscience*, 7(8):564–568.

Benkhoff, J., van Casteren, J., Hayakawa, H., Fujimoto, M., Laakso, H., Novara, M., Ferri, P., Middleton, H. R., and Ziethe, R. (2010). BepiColombo-Comprehensive exploration of Mercury: Mission overview and science goals. *Planetary and Space Science*, 58(1-2):2–20.

Blewett, D. T., Chabot, N. L., Denevi, B. W., Solomon, S. C., Xiao, Z., Ernst, C. M., Oberst, J., Nittler, L. R., Preusker, F., Braden, S. E., Murchie, S. L., Head, J. W., Fassett, C. I., McCoy, T. J., Scholten, F., Hurwitz, D. M., Baker, D. M. H., and Izenberg, N. R. (2011). Hollows on Mercury: MESSENGER Evidence for Geologically Recent Volatile-Related Activity. *Science*, 333(6051):1856–1859.

Brož, P., Čadek, O., Wright, J., and Rothery, D. A. (2018). The Apparent Absence of Kilometer-Sized Pyroclastic Volcanoes on Mercury: Are We Looking Right? *Geophysical Research Letters*, 45(22):12,171–12,179.

Burke, K. and Torsvik, T. H. (2004). Derivation of Large Igneous Provinces of the past 200 million years from long-term heterogeneities in the deep mantle. *Earth and Planetary Science Letters*, 227(3-4):531–538.

Burke, K., Werner, S. C., Steinberger, B., and Torsvik, T. H. (2012). Why is the areoid like the residual geoid? *Geophysical Research Letters*, 39(17):2004–2008.

Cameron, A. G. W. (1985). The partial volatilization of Mercury. *Icarus*, 64(2):285–294.

Castle, J. C., Creager, K. C., Winchester, J. P., and van der Hilst, R. D. (2000). Shear wave speeds at the base of the mantle. *Journal of Geophysical Research*, 105:21543.

Connolly, J. A. (1990). Multivariable phase-diagrams: an algorithm based on generalized thermodynamics. *American Journal of Science*, 290:666–718.

Cottaar, S. and Lekic, V. (2016). Morphology of seismically slow lower-mantle structures. *Geophysical Journal International*, 207(2):1122–1136.

Denevi, B. W., Ernst, C. M., Meyer, H. M., Robinson, M. S., Murchie, S. L., Whitten, J. L., Head, J. W., Watters, T. R., Solomon, S. C., Ostrach, L. R., Chapman, C. R., Byrne, P. K., Klimczak, C., and Peplowski, P. N. (2013). The distribution and origin of smooth plains on Mercury. *Journal of Geophysical Research E: Planets*, 118(5):891–907.

Dubrovinsky, L. S., N. Dubrovinskaia, Langenhorst, F., Dobson, D. P., Rubie, D. C., Geßmann, C., Abrikosov, I. A., Johansson, B., Baykov, V. I., Vitos§q, L., Bihan, T. L., Crichton, W. a., Dmitriev, V., and Weber, H. P. (2003). Iron – silica interaction at extreme conditions and the electrically conducting layer at the base of Earth's mantle. *Nature*, 422:58–61.

Dumay, C. and Cramb, A. W. (1995). Density and interfacial tension of liquid Fe-Si alloys. *Metallurgical and Materials Transactions B*, 26(1):173–176.

Fassett, C. I., Head, J. W., Blewett, D. T., Chapman, C. R., Dickson, J. L., Murchie, S. L., Solomon, S. C., and Watters, T. R. (2009). Caloris impact basin: Exterior geomorphology, stratigraphy, morphometry, radial sculpture, and smooth plains deposits. *Earth and Planetary Science Letters*, 285(3-4):297–308.

Fassett, C. I., Kadish, S. J., Head, J. W., Solomon, S. C., and Strom, R. G. (2011). The global population of large craters on Mercury and comparison with the Moon. *Geophysical Research Letters*, 38(10).

Fegley, B. and Cameron, A. G. (1987). A vaporization model for iron/silicate fractionation in the Mercury protoplanet. *Earth and Planetary Science Letters*, 82(3-4):207–222.

Fowler, C. (2005). *The Solid Earth: an introduction to global geophysics*. Cambridge University Press, United Kingdom, 2nd edition.

Garnero, E. J., McNamara, A. K., and Shim, S. H. (2016). Continent-sized anomalous zones with low seismic velocity at the base of Earth's mantle. *Nature Geoscience*, 9(7):481–489.

Goettel, K. (1988). Present bounds on the bulk composition of Mercury - Implications for planetary formation processes. In *Mercury*, pages 613–621. University of Arizona Press, Tucson.

Goudge, T., Head, J. W., Kerber, L., Blewett, D. T., Denevi, B. W., Domingue, D. L., Gillis-Davis, J. J., Gwinner, K., Helbert, J., Holsclaw, G. M., Izenberg, N. R., Klima, R. L., Mcclintock, W. E., Murchie, S. L., Neumann, G. A., Smith, D. E., Strom, R. G., Zhiyong, X., Zuber, M. T., and Solomon, S. C. (2014). Global inventory and characterization of pyroclastic deposits on Mercury: New insight into pyroclastic activity from MESSENGER orbital data. *Journal of Geophysical Research: Planets*, 119:635–658.

Hauck, S. A., Margot, J. L., Solomon, S. C., Phillips, R. J., Johnson, C. L., Lemoine, F. G., Mazarico, E., McCoy, T. J., Padovan, S., Peale, S. J., Perry, M. E., Smith, D. E., and Zuber, M. T. (2013). The curious case of Mercury's internal structure. *Journal of Geophysical Research E: Planets*, 118(6):1204–1220.

He, Y. and Wen, L. (2009). Structural features and shear-velocity structure of the "Pacific Anomaly". *Journal of Geophysical Research: Solid Earth*, 114(2):1–17.

Head, J. W., Chapman, C. R., Domingue, D. L., Hawkins, S. E., McClintock, W. E., Murchie, S. L., Prockter, L. M., Robinson, M. S., Strom, R. G., and Watters, T. R. (2007). The geology of mercury: The view prior to the MESSENGER mission. *Space Science Reviews*, 131:41–84.

Head, J. W., Phillips, R. J., Watters, T. R., Oberst, J., Preusker, F., Solomon, S. C., and Zuber, M. T. (2010). The morphology of Mercury's Caloris basin as seen in MESSENGER stereo topographic models. *Icarus*, 209(1):230–238.

Head, J. W. and Wilson, L. (2015). Chapter 40 - Volcanism on Mercury. In *The Encyclopedia of Volcanoes (Second Edition)*, pages 701 – 716. Academic Press, Amsterdam, Second edition.

Hemingway, D. J. and Matsuyama, I. (2017). Isostatic equilibrium in spherical coordinates and implications for crustal thickness on the Moon , Mars , Enceladus , and elsewhere. *Geophysical Research Letters*, 44(15):7695–7705.

Hernlund, J. W., Thomas, C., and Tackley, P. J. (2005). A doubling of the post-pervoskite phase boundary and structure of the Earth's lowermost mantle. *Science*, 434(18):1615–1618.

Hirose, K. (2006). Postperovskite Phase Transition and Its Geophysical Implications. *Review of Geophysics*, 44(3).

Hirose, K., Karato, S. I., Cormier, V. F., Brodholt, J. P., and Yuen, D. A. (2006). Unsolved problems in the lowermost mantle. *Geophysical Research Letters*, 33(12):10–13.

Holland, T. J. B. and Powell, R. (2004). An internally consistent thermodynamic data set for phases of petrological interest. *Journal of Metamorphic Geology*, 16(3):309–343.

James, P. B. (2018). The Enigma of Mercury's Northern Rise. In *Mercury: Current and Future Science 2018*, volume 2047.

James, P. B., Zuber, M. T., Phillips, R. J., and Solomon, S. C. (2014). Support of long-wavelength topography on Mercury inferred from MESSENGER measurements of gravity and topography. *Journal of Geophysical Research: Planets*, 120(2):287–310.

Kerber, L., Head, J. W., Blewett, D. T., Solomon, S. C., Wilson, L., Murchie, S. L., Robinson, M. S., Denevi, B. W., and Domingue, D. L. (2011). The global distribution of pyroclastic deposits on Mercury: The view from MESSENGER flybys 1-3. *Planetary and Space Science*, 59(15):1895–1909.

Knittle, E. and Jeanloz, R. (1989). Simulating the Core-Mantle Boundary: an Experimental Study of High-pressure Reactions Between Silicates and Liquid Iron. *Geophysical Research Letters*, 16(7):609–612.

Koelemeijer, P., Deuss, A., and Ritsema, J. (2017). Density structure of Earth's lowermost mantle from Stoneley mode splitting observations. *Nature Communications*, 8(15241).

Komabayashi, T. and Fei, Y. (2010). Internally consistent thermodynamic database for iron to the Earth's core conditions. *Journal of Geophysical Research: Solid Earth*, 115(3):1–12.

Krot, A. N., Meibom, A., Russell, S. S., Alexander, C. M. O. D., Jeffries, T. E., and Keil, K. (2001). A new astrophysical setting for chondrule formation. *Science*, 291(5509):1776–1779.

Kuo, B.-Y., Garnero, E. J., and Lay, T. (2000). Tomographic inversion of S–SKS times for shear velocity heterogeneity in D": Degree 12 and hybrid models. *Journal of Geophysical Research*, 105(B12):28139–28157.

Lay, T. and Helmberger, D. V. (1983). A shear velocity discontinuity in the lower mantle. *Geophysical Research Letters*, 10(1):63–66.

Lin, J.-F., Campbell, A. J., Heinz, D. L., and Shen, G. (2003). Static compression of iron-silicon alloys: Implications for silicon in the Earth's core. *Journal of Geophysical Research: Solid Earth*, 108(B1).

Lissauer, J. J. and de Pater, I. (2013). *Fundamental Planetary Science*. Cambridge University Press, New York, 1st edition.

Liu, X. and Zhong, S. (2015). The long-wavelength geoid from three-dimensional spherical models of thermal and thermochemical mantle convection. *Journal of Geophysical Research: Solid Earth*, 120(6):4572–4596.

Manga, M. and Jeanloz, R. (1996). Implications of a metal-bearing chemical boundary layer in D" for mantle dynamics. *Geophysical Research Letters*, 23(22):3091–3094.

Margot, J., Hauck, S., Mazarico, E., S., P., and Peale, S. (2018). Mercury's Internal Structure. In *Mercury: The View after MESSENGER*, pages 85–114. Cambridge University Press, Cambridge.

Matsuyama, I. and Nimmo, F. (2009). Gravity and tectonic patterns of Mercury: Effect of tidal deformation, spin-orbit resonance, nonzero eccentricity, despinning, and reorientation. *Journal of Geophysical Research E: Planets*, 114(1):1–23.

May, S. (2011). What Is the Planet Mercury? Retrieved from `https://www.nasa.gov/audience/forstudents/k-4/stories/nasa-knows/what-is-planet-mercury-k4.html`. Accessed: 02 July 2018.

Mazarico, E., Genova, A., Goossens, S., Lemoine, F. G., Neumann, G. A., Zuber, M. T., Smith, D. E., and Solomon, S. C. (2014). The gravity field, orientation, and ephemeris of Mercury from MESSENGER observations after three years in orbit. *Journal of Geophysical Research: Planets*, 119(12):2417–2436.

McNamara, A. K. and Zhong, S. (2005). Thermochemical structures beneath Africa and the Pacific Ocean. *Nature*, 437(7062):1136–1139.

Melosh, H. J., Freed, A. M., Johnson, B. C., Blair, D. M., Andrews-Hanna, J. C., Neumann, G. A., Philips, R. J., Smith, D. E., Solomon, S. C., Wieczorek, M. A., and Zuber, M. T. (2013). The Origin of Lunar Mascon Basins. *Science*, 340(June):1552–1555.

Mohr, P., Taylor, B., and Newell, D. (2012). CODATA recommended values of the fundamental physical constants: 2010. *Reviews of Modern Physics*, 84(4):1527–1605.

Morgan, J. W. and Anders, E. (1980). Chemical composition of Earth, Venus, and Mercury. *Proceedings of the National Academy of Sciences*, 77(12):6973–6977.

Muller, P. M. and Sjogren, W. L. (1968). Mascons: Lunar mass concentrations. *Science*, 161(3842):680–684.

Murakami, M. (2004). Post-Perovskite Phase Transition in MgSiO3. *Science*, 304(5672):855–858.

Nittler, L. R., Chabot, N. L., Grove, T. L., and Peplowski, P. N. (2018). The Chemical Composition of Mercury. In *Mercury: The View after MESSENGER*, page 30–51. Cambridge University Press, Cambridge.

Oganov, A. R. and Ono, S. (2004). Theoretical and experimental evidence for a post-perovskite phase of MgSiO3 in Earth's D" layer. *Nature*, 430(6998):445–448.

Otsuka, K. and Karato, S. I. (2012). Deep penetration of molten iron into the mantle caused by a morphological instability. *Nature*, 492:pages 243–246.

Padovan, S., Wieczorek, M. A., Margot, J. L., Tosi, N., and Solomon, S. C. (2015). Thickness of the crust of Mercury from geoid-to-topography ratios. *Geophysical Research Letters*, 42(4):1029–1038.

Pawlowski, R. S. (1994). Green's equivalent-layer concept in gravity band-pass filter design. *Geophysics*, 59(1):69–76.

Peale, S. (1988). The rotational dynamics of Mercury and the state of its core. In *Mercury*, pages 461–493. University of Arizona Press, Tucson.

Peale, S. J. (1969). Generalized Cassini's Laws. *The Astronomical Journal*, 74(3):483–489.

Prockter, L. M., Ernst, C. M., Denevi, B. W., Chapman, C. R., Head III, J. W., Fassett, C. I., Merline, W. J., Solomon, S. C., Watters, T. R., Strom, R. G., Cremonese, G., Marchi, S., and Massironi, M. (2010). Evidence for Young Volcanism on Mercury from the Third MESSENGER Flyby. *Science*, 329(5992):668–671.

Prockter, L. M., Murchie, S. L., Watters, T. R., Head, J. W., Blewett, D. T., Robinson, M. S., McClintock, W. E., Domingue, D. L., Chapman, C. R., Solomon, S. C., and Strom, R. G. (2008). Geology of the Caloris Basin, Mercury: A View from MESSENGER. *Science*, 321(5885):73–76.

Qingyun, D., Fei, L., Jianguo, Y., Zhiyong, X., and Rodriguez, J. A. P. (2018). Buried Impact Features on Mercury as Revealed by Gravity Data. *Journal of Geophysical Research: Planets*, 123(11):3005–3019.

Rivoldini, A., Van Hoolst, T., and Verhoeven, O. (2009). The interior structure of Mercury and its core sulfur content. *Icarus*, 201(1):12–30.

Root, B. C., Ebbing, J., van der Wal, W., England, R. W., and Vermeersen, L. L. (2017). Comparing gravity-based to seismic-derived lithosphere densities: A case study of the British Isles and surrounding areas. *Geophysical Journal International*, 208(3):1796–1810.

Root, B. C., Novák, P., Dirkx, D., Kaban, M., van der Wal, W., and Vermeersen, L. L. (2016). On a spectral method for forward gravity field modelling. *Journal of Geodynamics*, 97:22–30.

Schubert, G., Masters, G., Olson, P., and Tackley, P. (2004). Superplumes or plume clusters? *Physics of the Earth and Planetary Interiors*, 146(1-2):147–162.

Sidorin, I., Gurnis, M., and Helmberger, D. V. (1999). Dynamics of a phase change at the base of the mantle consistent with seismological observations. *Journal of Geophysical Research*, 104(B7):15005–15023.

Smith, D. E., Zuber, M. T., Phillips, R. J., Solomon, S. C., II, S. A. H., Lemoine, F. G., Mazarico, E., Neumann, G. A., Peale, S. J., Margot, J.-l., Johnson, C. L., Torrence, M. H., Perry, M. E., Rowlands, D. D., Goossens, S., Head, J. W., and Taylor, A. H. (2012). Gravity Field and Internal Structure of Mercury from MESSENGER. *Science*, 336(6078):214–217.

Soldati, G., Koelemeijer, P., Boschi, L., and Deuss, A. (2013). Constraints on core-mantle boundary topography from normal mode splitting. *Geochemistry, Geophysics, Geosystems*, 14(5):1333–1342.

Sori, M. M. (2018). A thin, dense crust for Mercury. *Earth and Planetary Science Letters*, 489:92–99.

Steinberger, B. and Torsvik, T. H. (2012). A geodynamic model of plumes from the margins of Large Low Shear Velocity Provinces. *Geochemistry, Geophysics, Geosystems*, 13(Q01W09).

Su, W.-J. and Dziewonski, A. M. (1997). Simultaneous inversion for 3-D variations in shear and bulk velocity in the mantle. *Physics of the Earth and Planetary Interiors*, 100(1-4):135–156.

Tan, E., Gurnis, M., and Han, L. (2002). Slabs in the lower mantle and their modulation of plume formation. *Geochemistry, Geophysics, Geosystems*, 3(11):1–24.

Taylor, G. and Scott, E. R. D. (2005). Mercury. In *Meteorites, Comets, and Planets: Treatise on geochemistry*, pages 477–485. Elsevier, Amsterdam, Second edition.

Thomas, C., Garnero, E. J., and Lay, T. (2004a). High-resolution imaging of lowermost mantle structure under the Cocos plate. *Journal of Geophysical Research: Solid Earth*, 109(8):1–11.

Thomas, C., Kendall, J. M., and Lowman, J. (2004b). Lower-mantle seismic discontinuities and the thermal morphology of subducted slabs. *Earth and Planetary Science Letters*, 225(1-2):105–113.

To, A., Romanowicz, B., Capdeville, Y., and Takeuchi, N. (2005). 3D effects of sharp boundaries at the borders of the African and Pacific Superplumes: Observation and modeling. *Earth and Planetary Science Letters*, 233(1-2):137–153.

Torsvik, T. H., Smethurst, M. A., Burke, K., and Steinberger, B. (2006). Large igneous provinces generated from the margins of the large low-velocity provinces in the deep mantle. *Geophysical Journal International*, 167(3):1447–1460.

Torsvik, T. H., Smethurst, M. A., Burke, K., and Steinberger, B. (2008). Long term stability in deep mantle structure: Evidence from the ~300 Ma Skagerrak-Centered Large Igneous Province (the SCLIP). *Earth and Planetary Science Letters*, 267(3-4):444–452.

Tosi, N., Čadek, O., Běhounková, M., Káňová, M., Plesa, A. C., Grott, M., Breuer, D., Padovan, S., and Wieczorek, M. A. (2015). Mercury's low-degree geoid and topography controlled by insolation-driven elastic deformation. *Geophysical Research Letters*, 42(18):7327–7335.

Trønnes, R. G. (2010). Structure, mineralogy and dynamics of the lowermost mantle. *Mineralogy and Petrology*, 99(3-4):243–261.

Volgyesi, L. and Moser, M. (1982). Inner Structure of the Earth. *Periodica Polytechnica Chemical Engineering*, 26(3-4):155–204.

Wang, Y. and Wen, L. (2007). Complex seismic anisotropy at the border of a very low velocity province at the base of the Earth's mantle. *Journal of Geophysical Research: Solid Earth*, 112(9):1–11.

Watts, A. (2001). *Isostacy and Flexure of the Lithosphere*. Cambridge University Press, New York.

Watts, A. B. and Moore, J. D. (2017). Flexural Isostasy: Constraints From Gravity and Topography Power Spectra. *Journal of Geophysical Research: Solid Earth*, 122(10):8417–8430.

Weidenschilling, S. J. (1978). Iron/silicate fractionation and the origin of Mercury. *Icarus*, 35(1):99–111.

Weider, S. Z., Nittler, L. R., Starr, R. D., Crapster-Pregont, E. J., Peplowski, P. N., Denevi, B. W., Head, J. W., Byrne, P. K., Hauck, S. A., Ebel, D. S., and Solomon, S. C. (2015). Evidence for geochemical terranes on Mercury: Global mapping of major elements with MESSENGER's X-Ray Spectrometer. *Earth and Planetary Science Letters*, 416:109–120.

Wen, L. (2001). Seismic evidence for a rapidly varying compositional anomaly at the base of the earth's mantle beneath the Indian Ocean. *Earth and Planetary Science Letters*, 194(1-2):83–95.

Wieczorek, M. A. (2015). Gravity and Topography of the Terrestrial Planets. In *Treatise on Geophysics: Second Edition*, pages 153–193. Elsevier, Second edition.

Wieczorek, M. A., Neumann, G. A., Nimmo, F., Kiefer, W. S., Taylor, G. J., Melosh, H. J., Phillips, R. J., Solomon, S. C., Andrews-Hanna, J. C., Asmar, S. W., Konopliv, A., Lemoine, F. G., Smith, D. E., Watkins, M. M., Williams, J., and Zuber, M. T. (2013). The crust of the Moon as seen by Grail. *Science*, 339(6120):671–676.

Wieczorek, M. A. and Phillips, R. J. (1998). Potential anomalies on a sphere: Application to the thickness of the lunar crust. *Journal of Geophysical Research*, 103(E1):1715–1724.

Wingate, M. T., Pirajno, F., and Morris, P. A. (2004). Warakurna large igneous province: A new Mesoproterozoic large igneous province in west-central Australia. *Geology*, 32(2):105–108.

Xu, W., Lithgow-Bertelloni, C., Stixrude, L., and Ritsema, J. (2008). The effect of bulk composition and temperature on mantle seismic structure. *Earth and Planetary Science Letters*, 275(1-2):70–79.

Zhao, D. (2001). Seismic structure and origin of hotspots and mantle plumes. *Earth and Planetary Science Letters*, 192(3):251–265.